NASA/CR—2019–220138

Acoustic Emission-Based Health Monitoring of Space Launch System Structures

D.O. Adams, J. Zhou, S. Kim, and B. Uprety
University of Utah, Salt Lake City, Utah

V.J. Mathews
Oregon State University, Corvallis, Oregon

Prepared for Marshall Space Flight Center
under Contract NNM13AA12G

September 2019

The NASA STI Program…in Profile

Since its founding, NASA has been dedicated to the advancement of aeronautics and space science. The NASA Scientific and Technical Information (STI) Program Office plays a key part in helping NASA maintain this important role.

The NASA STI Program Office is operated by Langley Research Center, the lead center for NASA's scientific and technical information. The NASA STI Program Office provides access to the NASA STI Database, the largest collection of aeronautical and space science STI in the world. The Program Office is also NASA's institutional mechanism for disseminating the results of its research and development activities. These results are published by NASA in the NASA STI Report Series, which includes the following report types:

- TECHNICAL PUBLICATION. Reports of completed research or a major significant phase of research that present the results of NASA programs and include extensive data or theoretical analysis. Includes compilations of significant scientific and technical data and information deemed to be of continuing reference value. NASA's counterpart of peer-reviewed formal professional papers but has less stringent limitations on manuscript length and extent of graphic presentations.

- TECHNICAL MEMORANDUM. Scientific and technical findings that are preliminary or of specialized interest, e.g., quick release reports, working papers, and bibliographies that contain minimal annotation. Does not contain extensive analysis.

- CONTRACTOR REPORT. Scientific and technical findings by NASA-sponsored contractors and grantees.

- CONFERENCE PUBLICATION. Collected papers from scientific and technical conferences, symposia, seminars, or other meetings sponsored or cosponsored by NASA.

- SPECIAL PUBLICATION. Scientific, technical, or historical information from NASA programs, projects, and mission, often concerned with subjects having substantial public interest.

- TECHNICAL TRANSLATION. English-language translations of foreign scientific and technical material pertinent to NASA's mission.

Specialized services that complement the STI Program Office's diverse offerings include creating custom thesauri, building customized databases, organizing and publishing research results…even providing videos.

For more information about the NASA STI Program Office, see the following:

- Access the NASA STI program home page at <http://www.sti.nasa.gov>

- E-mail your question via the Internet to <help@sti.nasa.gov>

- Phone the NASA STI Help Desk at 757–864–9658

- Write to:
  NASA STI Information Desk
  Mail Stop 148
  NASA Langley Research Center
  Hampton, VA 23681–2199, USA

NASA/CR—2019–220138

Acoustic Emission-Based Health Monitoring of Space Launch System Structures

D.O. Adams, J. Zhou, S. Kim, and B. Uprety
University of Utah, Salt Lake City, Utah

V.J. Mathews
Oregon State University, Corvallis, Oregon

Prepared for Marshall Space Flight Center
under Contract NNM13AA12G
and sponsored by

National Aeronautics and
Space Administration

Marshall Space Flight Center • Huntsville, Alabama 35812

September 2019

Acknowledgements

The authors express their appreciation to Chris Deemer of Orbital ATK for his technical input and valuable interactions throughout the duration of the project. Additionally, the authors acknowledge the technical assistance of Jeff Kessler and Joel Harley of the University of Utah. Finally, the authors wish to thank Mindy Nettles, Program Manager, and Alan Nettles, Technical Monitor, of NASA Marshall Space Flight Center for their technical direction and encouragement.

Available from:

NASA STI Information Desk
Mail Stop 148
NASA Langley Research Center
Hampton, VA 23681–2199, USA
757–864–9658

TABLE OF CONTENTS

TABLE OF CONTENTS (Continued)

LIST OF FIGURES

LIST OF FIGURES (Continued)

LIST OF FIGURES (Continued)

LIST OF FIGURES (Continued)

LIST OF FIGURES (Continued)

LIST OF FIGURES (Continued)

LIST OF FIGURES (Continued)

LIST OF TABLES

LIST OF TABLES (Continued)

1. INTRODUCTION

This report documents the technical accomplishments of the project, "Acoustic Emission-Based Health Monitoring of Space Launch System Structures," sponsored by the National Aeronautics and Space Administration (Award No. NNM13AA12G). As the project title suggests, the goal of the project was to develop a structural health monitoring (SHM) system for Space Launch System (SLS) vehicles based on acoustic emission (AE) or AE-like signals. Such a system will enhance SLS reliability by identifying the damage locations and type of damage when the damage is initiated. This SHM system would also lead to reduced maintenance costs by enabling ground support equipment to inspect only SLS elements or parts that are likely to be damaged. Finally, it will facilitate lean designs that meet tolerance levels specified by barely detectable damage. By avoiding excess conservatism in this manner, this SHM system will further reduce manufacturing costs of SLS vehicles.

1.1 Objectives

The specific objectives of the project were to:

- Refine and characterize a method for locating the sources of AE in anisotropic structures without knowledge of direction and location-dependent wave propagation properties of the structure. The method utilized a sparse sensor distribution on the structure such that monitoring of the complete structure is possible and the accuracy of location estimation is maintained.
- Determine from sensor waveforms if there is damage in the structure and classify potential damage types when damage is present.
- Experimentally validate the developed methods.

1.2 Summary of Project Accomplishments

In this section we provide a summary of the accomplishments of this project, demonstrating that the above objectives were accomplished.

1.2.1 Impact Location Estimation Using Acoustic Emission Signals

The research performed in this project resulted in several methods for impact location estimation on composite structures by analyzing acoustic emission signals acquired by sensors attached to the structures. Chapter 2 presents the method which was found to be the best performing in our experimental validations. Because composite structures are typically anisotropic, wave propagation velocities depend on the propagation directions and locations. Furthermore, accurate characterization of the direction-dependent wave velocities may not always be possible for complex composite structures. The location estimation method presented does not require knowledge of the location and direction-dependent velocities of wave propagation in the structure. The method employs clusters of three sensors located in close proximity to each other on the structure, and formulates the location estimation problem as the solution to a constrained optimization problem involving an array of sensor clusters located on the structure. The effect of sensor separation within each cluster, the number of sensor clusters and the signal-to-noise ratio on the algorithm performance were analyzed numerically. Experimental validation of the method was performed using two different composite panels subjected to drop-weight impacts. Analysis of the results indicated that five sensor clusters are adequate to produce accurate location estimates, provided that the acoustic emission arrives at the sensors with sufficiently high signal-to-noise ratio. Furthermore, experimental comparisons with a competing method available in the literature demonstrated the superiority of the algorithm developed in this project. Additionally, experimental results demonstrated the robustness of the algorithm to temperature changes in the composite panels.

1.2.2 Acoustic Emission-Based Damage Classification for Composite Structures

The second significant objective of this research project focused on damage classification from AE signals. Of particular interest was identifying the most important features of the AE signals for use in identifying impacts resulting in damage to a composite structure as well as classify the damage as either delamination-only or delamination plus fiber breakage. Chapter 3 of this report describes an efficient machine learning approach, based on logistic regression, developed for this purpose. The experimental set up including composite structure selection, sensor selection, type of impacting experiments, and inspection for damage were carefully and systematically designed to train and test the method. The most useful features of the AE signals were obtained from the training data. Cross-validation experiments indicated that the classification algorithm identified impacts resulting in damage with 100% accuracy. Classification of damage type showed a 74% accuracy and requires additional refinements.

1.2.3 Comparative Acoustic Emission Sensor Evaluation

In support of the SHM system development, six commercially available piezoelectric sensors were evaluated. The results of this comparative evaluation are presented in Chapter 4. Of particular interest was a comparison of the acoustic response of the candidate piezoelectric sensors for impact location estimation as well as damage classification resulting from impact in fiber-reinforced composite structures. Sensor assessment was performed based on response signal characterization and performance for active testing at 300 kHz as well as steel-ball drop testing using both aluminum and carbon/epoxy composite plates. Wave mode velocities calculated from the measured arrival times were found to be in good agreement with predictions obtained using the software code Disperse, which calculates the dispersion curves of multi-layer composite structures, as well as finite element analysis. Differences in the relative strength of the received wave modes, the overall signal strengths and signal-to-noise ratios were investigated through the use of both active testing and passive steel-ball drop testing. Four of the six sensor types investigated showed the promising results and were recommended for future studies with instrumented low-velocity impact conditions.

1.2.4 Damage Characterization Under Quasi-static Loading

In Chapter 5, testing and subsequent analyses were performed to identify AE signal features that are discriminative of different composite damage types. Quasi-static testing of composite panels was performed to characterize damage states using AE signals. A specialized four-point bend test specimen was developed to investigate each damage state under quasi-static loading. Additionally, double cantilever beam (DCB) testing was performed on specimens that exhibited four different types of fracture surfaces resulting in differences in the quantity and type of fiber breakage due to fiber bridging. The results of four-point bend testing with two customized types of specimen suggest that the peak frequency as well as the frequency centroid, traditional AE parameters in the frequency domain, do not provide useful information when a multiple-damage state is produced. However, a new damage characterization parameter, referred to as the frequency magnitude ratio, showed potential for identifying damage types produced in cases where both single and multiple damage types are produced.

The inspection of fracture surfaces of DCB test specimens following testing suggested that frequency characteristic of the AE signals may be of use for identifying the occurrence of fiber breakage during the propagation of a delamination. Further, 3D histogram plots constructed using the frequency of peak amplitude as well as the frequency magnitude ratio provides additional detailed information on the damage state, especially when multiple damage types are produced.

1.2.5 Impact Damage Classification and Feature Selection

Chapter 6 presents additional results on experimental design and feature selection for impact damage classification in composite structures. Through the use of both ultrasonic inspection and thermal de-ply analysis following impact testing, relationships between impact conditions and the resulting damage states were investigated. Preliminary signal analysis for damage classification was conducted using waterfall FFT plots superimposed on impact force versus time curves, and characteristic frequency ranges corresponding to fiber and matrix damage were suggested. Results suggest that impact damage classification is possible in composite structures through the analysis of AE signal features.

1.2.6 Numerical Modeling of the Effects of Geometrical Complexities

As the impact location-estimation algorithm developed in this project for SHM utilizes Lamb wave time-of-arrival information, the characteristics of such wave propagation in actual composite structures are of particular interest. Chapter 7 describes studies on two particular

Lamb wave propagation characteristics investigated using numerical analysis. First, the directional dependence of Lamb wave velocity in composite laminates was investigated. Finite element analyses featuring layer-by-layer modeling and applied displacement signal inputs were used to explore directional dependence of wave propagation in a quasi-isotropic carbon/epoxy composite laminate. Results from both analysis and experiment suggest that directional dependence of Lamb wave propagation may occur in a quasi-isotropic composite laminate, even though the effective, homogenized elastic properties are the same in all in-plane directions. Second, AE propagation was investigated experimentally in composite structures with geometrical complexities as well as with relatively large distances between impact location and sensor positions. Experimental approaches and signal analysis methods were developed to evaluate changes in AE signals caused by these structural variations. Furthermore, a new technique to combat the difficulties caused by changes in characteristics of the AE signals due to long propagation paths was developed.

2. ACOUSTIC EMISSION-BASED IMPACT LOCATION ESTIMATION

Impacts on composite structures can compromise structural integrity without providing visible evidence of damage. Therefore, impact detection and impact location estimation are important in structural health monitoring (SHM) systems. A generic block diagram of an SHM system, typically used for impact damage detection and assessment, is shown in Figure 2-1. Impacts generate acoustic emission (AE) or AE-like signals that propagate through the structure. A sensor network placed on the structure monitors the structure continuously for signals generated by impacts or by resulting structural damage. The AE signals are analyzed to detect impacts and estimate the impact location. Additional analysis to assess damage characteristics and provide guidance for maintenance strategies are part of SHM systems, but are not considered here.

Source location estimation with passive sensor arrays has been studied for decades. For example, locating voice sources maybe performed using passive microphone arrays by calculating the time delay between pairs of microphones. Three microphones were used in [1] to estimate the location of the source by triangulation. Another classical method for estimating source location uses intersecting hyperboloids. Schau and Robinson [2] employed intersecting spherical surfaces and derived a closed-form solution for source location from sensor locations and time delay estimates. Huang et al. [3] solved for the source location by finding the solution to a linear optimization problem with a quadratic constraint.

Unlike the models in [1]-[3] that assumed a constant travel velocity of the source signal, the signals emitted from the impact source in composite structures typically propagate with direction-dependent velocities. Several papers on estimating impact locations from AE signals for anisotropic structures are available in the literature. The classical triangulation method proposed by Coverley and Staszewski [4] requires prior knowledge of wave propagation information in the structure. The wave velocities were characterized as functions of their travel directions based on experimental analysis. Three sensors were placed sufficiently separated from each other, and the signal travel paths to the three sensors were determined from the known wave velocities and the measured times of arrival (TOA) of the signals at the sensors. The impact location estimate was restricted to a triangular area constructed from the signal travel paths. A genetic algorithm was applied to identify this triangle. The impact coordinates were estimated as the average values of the vertices of the estimated triangle.

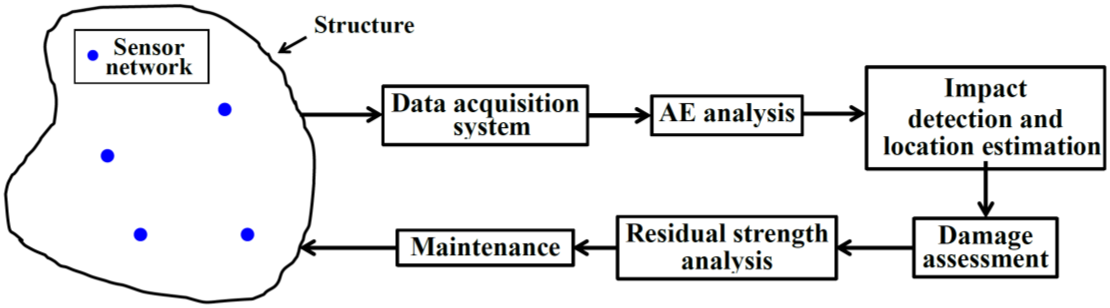

Figure 2-1. A generic block diagram of an SHM system.

There are several source location estimation methods based on the relationship that the signal travel time equals the travel distance divided by the average group velocity of the propagated waveforms. Salehian [5] developed an impact location estimation algorithm for composite panels. Two equalities were derived that related the locations of the three sensors placed in a triangular pattern on the structure, the time differences of arrivals (TDOAs) of the impact signals at each of two sensors and the group wave velocities. The group wave velocities were experimentally determined prior to deployment of the structure, and applied to the two equalities. The directions of arrival (DOAs) of the signals that traveled from the impact location to two of the three sensors were estimated from the two equalities. The impact location was then determined from the two DOAs. Meo et al. [6] implemented the algorithm in [5] using a composite sandwich panel. Kundu et al. [7] determined the impact location by minimizing an error function constructed using the sensor locations, the impact location, the TDOAs and the wave velocities. The velocity profiles were experimentally determined and a grid search method was employed to minimize the error function. A similar error function was used in [8] and the algorithm was evaluated using experiments performed on composite panels. Papulak [9] experimentally estimated the direction-dependent velocities in composite plates and the wave propagation information was characterized as a function of the DOA of the waveforms. Four sensors, equally spaced along a straight line, were used in each sensor cluster. The wave velocity corresponding to each cluster was computed from the sensor signals. The DOA of the signals reaching each cluster was obtained from the estimated relationship between wave velocities and the DOA. The estimated impact location was the intersection of the DOAs corresponding to two sensor clusters.

Due to the directionally-dependent wave velocities in anisotropic structures, the impact location estimation problem is more complex than for isotropic structures. In many applications, characterizing the direction and location dependent wave velocity information experimentally is not feasible due to the size and geometric complexity of the structure as well as the in-use variations resulting from repairs and changes in the operating environment [10, 11]. Therefore it is desirable to develop a method for estimating the impact location without the use of the wave propagation properties of the structures. Several such methods which do not require wave velocity have been proposed to date. Hiche et al. [12] developed a strain amplitude-based impact location estimation method in which the AE signals generated from the impact were measured using fiber Bragg grating sensors. An impact location estimate was computed from the strain values measured at two sensor locations. However, this estimate was constrained to be in the direction of the straight line connecting the two sensors. To overcome this limitation, additional sensors were utilized and additional impact location estimates were made from different combinations of sensor pairs. The overall impact location was estimated as the average of the estimates from multiple sensor pairs that recorded higher strain magnitudes than a predefined threshold. However, the accuracy of this method is dependent on the sensing range of the sensors used, and inaccurate location estimation may result from incomplete sensor coverage on the structures. Ciampa et al. [13] used three pairs of sensors to estimate the impact location. The group velocities corresponding to each sensor pair were assumed to be equal, and three nonlinear equations were obtained that were functions of the sensor locations, the impact location, TOAs, TDOAs and the group velocities. The impact location was obtained by solving for the unknown coordinate values from these equations using the Newton method. Zhou et al. [14] formulated the impact location estimation problem as a constrained optimization problem involving a number of sensor pairs. The two sensors within each sensor pair were located close to each other. The sensor pair locations, impact location, TDOAs and an assumed minimum velocity were used to formulate the optimization problem. The impact location was part of a vector of several unknown parameters estimated by minimizing an objective function in these parameters. The TDOAs between sensors belonging to different pairs were required to formulate and solve the optimization problem. For a composite structure, it is likely that the impact signals received at well-separated sensor locations would differ significantly due to the anisotropy of the structure. However, this is typically not the case for signals arriving at sensors close to each other. As a result, it is difficult to estimate the TDOA accurately between signals at sensors in different pairs compared with signals measured by sensors in close proximity within a sensor cluster. To further improve the TDOA estimation accuracy and hence the impact location estimation accuracy, Zhou et al. [15] developed another method that required only the TDOA at three sensors located close to each other and defined as a single sensor cluster. A set of quadratic equations were derived using multiple three-sensor clusters and an objective function was developed involving the impact location, sensor locations and TDOAs. The impact location was estimated using a grid search method. Further work by Zhou et al. [16] focused on experimental validation using different types of anisotropic structures.

Kundu et al. [17] used two clusters of sensors, each constructed with three sensors placed at the vertices of an isosceles right triangle, to estimate impact locations. The distance between sensors in each cluster was small in comparison to the distance from the impact location, and therefore the wave velocities corresponding to each sensor within a cluster were approximately equal. The DOAs of the impact signal at the sensor clusters were estimated from the TDOAs. The intersection of DOAs associated with two sensor clusters was taken as the estimated impact location. Other arrangements of sensor clusters have also been investigated. For example, Rima and Banerjee [18] designed a sensor cluster by placing eighteen sensors into a “Theodorus Spiral" pattern. The impact location was determined using a modified version of the error function in [7] by removing the wave velocities. Several other techniques have been used for source or impact location estimation, such as the time reversal method [19], which was originally derived in [20], eigen analysis-based methods [21, 22] and Multiple Signal Classification (MUSIC)-based algorithms [23].

In practical applications of impact location estimation that do not utilize any wave propagation velocity information, currently available methods require improvements in impact location estimation accuracy, simplified sensor array setup and computational simplicity for real-time implementation. In this chapter, an improved algorithm is presented for impact location estimation in anisotropic structures with no prior characterization or knowledge of the wave propagation properties. The TDOA estimation algorithm presented is an extension of the authors' previous work in [16] and utilizes the advantage of similar signals from sensors within the same cluster.

2.1 Impact Location Estimation Algorithm

The algorithm for estimating the impact location on an anisotropic structure was developed to utilize acoustic emission signals arriving at sensors distributed across the surface of the structure. The algorithm can also be applied to isotropic structures, which can be considered as a special case. Although the algorithm is derived for a two-dimensional structure for simplicity, extension of this approach to more complex structures is conceptually straightforward.

A basic problem setup is illustrated in Figure 2-2. A cluster of three sensors is located along with the location of impact at $\mathbf{X}_S = (x_S, y_S)^T$, where $()^T$ denotes the vector or matrix transpose. The three sensors are located at $\mathbf{S}_i^{(n)} = (x_i^{(n)}, y_i^{(n)})^T, i = 1,2,3$. These three sensors form the n-th sensor cluster. The placement of sensors into a cluster requires that the individual sensors are in close proximity. The triangle formed by the three sensors at the vertices may be of arbitrary shape with no specific restrictions on the angles between the sensors, other than that the three sensors are not placed in a straight line. We also assume that the impact location is sufficiently distant from the sensor cluster such that the waves arriving from the impact can be approximated as planar waves. Table 2-1 lists the notation used in this development.

Let us draw a line $\overline{\mathbf{S}_1^{(n)}\mathbf{A}}$ perpendicular to line $\overline{\mathbf{X}_S\mathbf{S}_2^{(n)}}$ and a line $\overline{\mathbf{S}_3^{(n)}\mathbf{B}}$ perpendicular to line $\overline{\mathbf{X}_S\mathbf{S}_2^{(n)}}$. Considering the two right triangles $\triangle\, \mathbf{S}_1^{(n)}\mathbf{X}_S\mathbf{A}$ and $\triangle\, \mathbf{S}_1^{(n)}\mathbf{S}_2^{(n)}\mathbf{A}$, and applying the Pythagorean theorem to these two triangles, we have

$$d_{S,1}^{(n)^2} - \overline{\mathbf{X}_S\mathbf{A}}^2 = \overline{\mathbf{S}_1^{(n)}\mathbf{A}}^2 \tag{2-1}$$

and

$$d_{1,2}^{(n)^2} - \overline{\mathbf{S}_2\mathbf{A}}^2 = \overline{\mathbf{S}_1^{(n)}\mathbf{A}}^2 . \tag{2-2}$$

Equating the left sides of (1) and (2) gives

$$d_{S,1}^{(n)^2} - \overline{\mathbf{X}_S\mathbf{A}}^2 = d_{1,2}^{(n)^2} - \overline{\mathbf{S}_2^{(n)}\mathbf{A}}^2 . \tag{2-3}$$

Because of the planar wave assumption, the distance that the wave traveled from the impact to the sensor $\mathbf{S}_1^{(n)}$ can be approximated as the length of the segment $\overline{\mathbf{X}_S\mathbf{A}}$. Therefore, the length of the segment $\overline{\mathbf{S}_2^{(n)}\mathbf{A}}$ can be approximated as the difference between the distance that the wave traveled from the impact $\mathbf{X}_S$ to reach $\mathbf{S}_2^{(1)}$ and the distance traveled to reach $\mathbf{S}_1^{(n)}$, i.e.,

$$\overline{\mathbf{S}_2^{(n)}\mathbf{A}} \approx d_{S,2}^{(n)} - d_{S,1}^{(n)} \, . \tag{2-4}$$

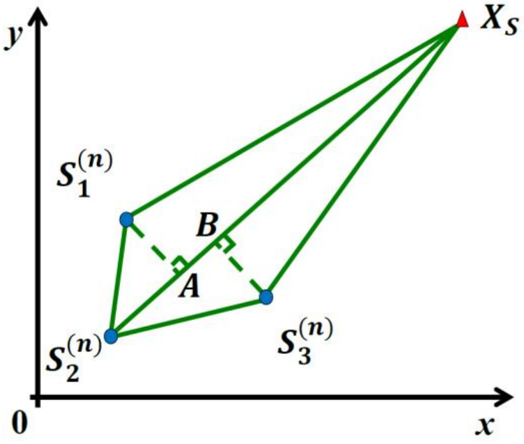

Figure 2-2. Sensor locations for one cluster and the impact location. The circles $\boldsymbol{S}_1^{(n)}$, $\boldsymbol{S}_2^{(n)}$ and $\boldsymbol{S}_3^{(n)}$ denote sensor locations and the triangle $\boldsymbol{X}_S$ denotes the impact location.

Table 2-1. Definition of Variables

Variable	**Definition**
$()^{(n)}$	Variable corresponding to the n-th sensor cluster
$d_{S,i}^{(n)}$	Distance between the impact location and the i-th sensor
$d_{i,j}^{(n)}$	Distance between the i-th and the j-th sensors
$v_i^{(n)}$	Average signal transmission velocity from the impact location to the i-th sensor
$t_i^{(n)}$	Time-of-arrival (TOA) of the wave generated by the impact at the i-th sensor
$\tau_{i,j}^{(n)}$	Time-difference-of-arrival (TDOA) of the wave between the i-th and the j-th sensors in the n-th cluster; $\tau_{i,j}^{(n)} = t_i^{(n)} - t_j^{(n)}$

According to the assumption that the distances between sensors in a cluster are small relative to the distance to the impact location, the wave velocities in the direction of the sensors in the same cluster from the impact location are approximately the same, i.e.,

$$v_1^{(n)} \approx v_2^{(n)} \approx v_3^{(n)}. \tag{2-5}$$

Therefore, the segment $\mathbf{S}_2^{(n)}\mathbf{A}$ can be expressed as

$$\overline{\mathbf{S}_2^{(n)}\mathbf{A}} \approx d_{S,2}^{(n)} - d_{S,1}^{(n)} = \left(t_2^{(n)} - t_1^{(n)}\right)v_1^{(n)} = \tau_{2,1}^{(n)}v_1^{(n)} \tag{2-6}$$

and the segment $\overline{\mathbf{X}_S\mathbf{A}}$ is expressed as

$$\overline{\mathbf{X}_S\mathbf{A}} = d_{S,2}^{(n)} - \overline{\mathbf{S}_2^{(n)}\mathbf{A}} = d_{S,2}^{(n)} - \tau_{2,1}^{(n)}v_1^{(n)}. \tag{2-7}$$

Substituting (2-6) and (2-7) into (2-3) and simplifying, we obtain

$${d_{S,1}^{(n)}}^2 - {d_{S,2}^{(n)}}^2 + 2d_{S,2}^{(n)}\tau_{2,1}^{(n)}v_1^{(n)} - {d_{1,2}^{(n)}}^2 = 0\,. \tag{2-8}$$

Next consider the two additional triangles, $\triangle\, \mathbf{X}_S\mathbf{S}_3^{(n)}\mathbf{B}$ and $\triangle\, \mathbf{S}_3^{(n)}\mathbf{S}_2^{(n)}\mathbf{B}$. Following a similar approach, a second equality is obtained:

$${d_{S,3}^{(n)}}^2 - {d_{S,2}^{(n)}}^2 + 2d_{S,2}^{(n)}\tau_{2,3}^{(n)}v_1^{(n)} - {d_{2,3}^{(n)}}^2 = 0\,. \tag{2-9}$$

The next step is to eliminate the velocity variable $v_1^{(n)}$ from (8) and (9). We will consider the cases $\tau_{2,3}^{(n)} \neq 0$ and $\tau_{2,3}^{(n)} = 0$ separately.

First, when $\tau_{2,3}^{(n)} \neq 0$, we solve for $v_1^{(n)}$ from (2-9) and then substitute into (2-8) and simplify, producing

$$\tau_{2,3}^{(n)}{d_{S,1}^{(n)}}^2 + (\tau_{2,1}^{(n)} - \tau_{2,3}^{(n)}){d_{S,2}^{(n)}}^2 - \tau_{2,1}^{(n)}{d_{S,3}^{(n)}}^2 + \tau_{2,1}^{(n)}{d_{2,3}^{(n)}}^2 - \tau_{2,3}^{(n)}{d_{1,2}^{(n)}}^2 = 0. \tag{2-10}$$

Recall that

$${d_{S,i}^{(n)}}^2 = (x_S - x_i^{(n)})^2 + (y_S - y_i^{(n)})^2 \tag{2-11}$$

and

$$d_{i,j}^{(n)^2} = (x_i^{(n)} - x_j^{(n)})^2 + (y_i^{(n)} - y_j^{(n)})^2 \ . \tag{2-12}$$

Substituting (2-11) and (2-12) into (2-10) and simplifying, we obtain

$$\alpha^{(n)} x_S + \beta^{(n)} y_S = \gamma^{(n)} \ , \tag{2-13}$$

where

$$\begin{aligned} \alpha^{(n)} &= \tau_{2,3}^{(n)} x_1^{(n)} + (\tau_{2,1}^{(n)} - \tau_{2,3}^{(n)}) x_2^{(n)} - \tau_{2,1}^{(n)} x_3^{(n)} \\ \beta^{(n)} &= \tau_{2,3}^{(n)} y_1^{(n)} + (\tau_{2,1}^{(n)} - \tau_{2,3}^{(n)}) y_2^{(n)} - \tau_{2,1}^{(n)} y_3^{(n)} \\ \gamma^{(n)} &= (\tau_{2,1}^{(n)} - \tau_{2,3}^{(n)})(x_2^{(n)^2} + y_2^{(n)^2}) \\ &\quad - \tau_{2,1}^{(n)} (x_2^{(n)} x_3^{(n)} + y_2^{(n)} y_3^{(n)}) \\ &\quad + \tau_{2,3}^{(n)} (x_1^{(n)} x_2^{(n)} + y_1^{(n)} y_2^{(n)}) \ . \end{aligned} \tag{2-14}$$

When $\tau_{2,3}^{(n)} = 0$, equation (2-9) becomes

$$d_{S,3}^{(n)^2} - d_{S,2}^{(n)^2} - d_{2,3}^{(n)^2} = 0 \ . \tag{2-15}$$

Rewriting (2-15) using the coordinate values,

$$\alpha^{(n)} x_S + \beta^{(n)} y_S = \gamma^{(n)}, \tag{2-16}$$

where

$$\begin{aligned} \alpha^{(n)} &= x_2^{(n)} - x_3^{(n)} \\ \beta^{(n)} &= y_2^{(n)} - y_3^{(n)} \\ \gamma^{(n)} &= x_2^{(n)^2} + y_2^{(n)^2} - x_2^{(n)} x_3^{(n)} - y_2^{(n)} y_3^{(n)} \ . \end{aligned} \tag{2-17}$$

For now, let us assume that $\tau_{2,1}^{(n)}$ and $\tau_{2,3}^{(n)}$ are available. As a result, the impact location coordinates x_S and y_S are the only two unknown parameters in (2-13), (2-14), (2-16) and (2-17). Therefore from each sensor cluster and the impact location, a single linear equality is produced by (2-13) or (2-16) in the two unknown coordinate values of the impact location. Similar expressions can be derived for every sensor cluster on the structure, providing N equations in two unknown variables when there are N sensor clusters. A least-squares approach can be used to solve for x_S and y_S from these equations when $N \geq 2$.

Using matrix notation, let the N equalities be written compactly as

$$\mathbf{\Omega X}_S = \mathbf{\Gamma}\,, \tag{2-18}$$

where $\mathbf{X}_S = (x_S, y_S)^T$ and

$$\mathbf{\Omega} = \begin{pmatrix} \alpha^{(1)} & \beta^{(1)} \\ \alpha^{(2)} & \beta^{(2)} \\ \vdots & \vdots \\ \alpha^{(N)} & \beta^{(N)} \end{pmatrix} \quad ; \qquad \mathbf{\Gamma} = \begin{pmatrix} \gamma^{(1)} \\ \gamma^{(2)} \\ \vdots \\ \gamma^{(N)} \end{pmatrix}. \tag{2-19}$$

The impact location estimate is the value of the vector $\mathbf{X}_S$ that solves the optimization problem given by

$$\begin{gathered} \min_{\mathbf{X}_S} \|\mathbf{\Omega X}_S - \mathbf{\Gamma}\|^2 \\ \text{s.t. } \mathbf{X}_S \in \mathbf{\Upsilon}\,, \end{gathered} \tag{2-20}$$

where $\mathbf{\Upsilon}$ is the set of all possible locations on the structure. For solving the optimization problem efficiently, a closed form solution is first obtained as the lease-squares solution to the objective function in (20) given by

$$\hat{\mathbf{X}}_S = (\mathbf{\Omega}^T \mathbf{\Omega})^{-1} \mathbf{\Omega}^T \mathbf{\Gamma}\,. \tag{2-21}$$

If $\hat{\mathbf{X}}_S \in \mathbf{\Upsilon}$, then $\hat{\boldsymbol{X}}_S$ is the optimal solution for the impact location. Otherwise, for structures for which $\mathbf{\Upsilon}$ is a convex set, it is straightforward to use interactive methods such as the Nelder-Mead simplex direct-search technique to find the solution. For irregular structures resulting in non-convex $\mathbf{\Upsilon}$, brute force methods such as grid-search techniques may be required to produce the best estimate [24].

2.1.1 Modification to the Algorithm

When the impacts are close to the boundaries of the structure, the signals generated from the impact get reflected from boundaries and complicates the sensor signals and their analysis. In particular, the calculation of signal TOAs for sensors which are distant from the impact are more likely to be confounded by the signal reflections than for sensors that are closer to the impact. Therefore, the algorithm was further modified to mitigate the problems created by signal reflections. Instead of using all sensor clusters, only three closest sensor clusters to the impact location were identified and used to estimate the impact location. The three closest sensor clusters were determined by selecting the three sensor clusters whose TOAs were the earliest.

2.1.2 Relationship to the Method in [17]

The method in [17] may be considered as a special case of the described method when the three sensors in each cluster form an isosceles right triangle. However, the formulation of the described method can be shown to be more robust to errors in TDOA estimates. Here, we compare the objective functions of the described method and the method in [17] when the sensor locations in each cluster form an isosceles right triangle.

Let us consider the n-th sensor cluster and one impact location $\mathbf{X}_S$. An example of the sensor locations and impact location is given in Figure 2-3. Assume that $\mathbf{S}_1^{(n)}$ and $\mathbf{S}_3^{(n)}$ are equidistant from $\mathbf{S}_2^{(n)}$, and the sides $\overline{\mathbf{S}_1\mathbf{S}_2}$ and $\overline{\mathbf{S}_2\mathbf{S}_3}$ form a right angle, and the sensor separation is d. For this configuration, which is easily generalizable for other orientations of this triangle,

$$\begin{aligned} x_1^{(n)} &= x_2^{(n)}, \\ y_1^{(n)} &= y_2^{(n)} + d \\ x_3^{(n)} &= x_2^{(n)} + d \\ y_3^{(n)} &= y_2^{(n)} . \end{aligned} \tag{2-22}$$

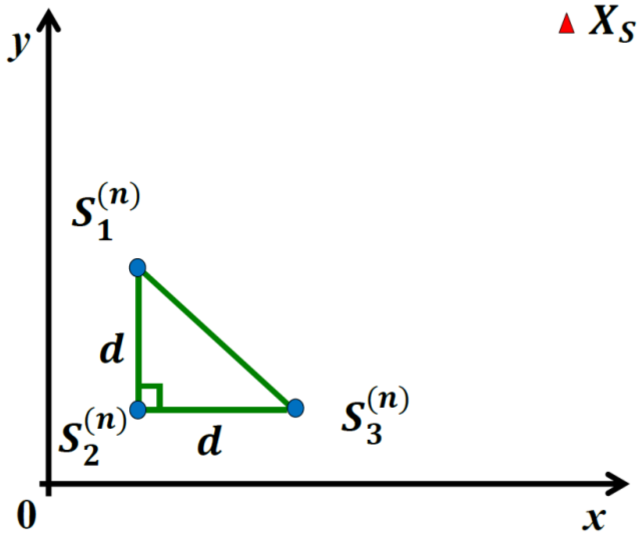

Figure 2-3. Sensor locations in a three-sensor cluster that forms an isosceles right triangle. The circles $\mathbf{S}_1^{(\mathrm{n})}$, $\mathbf{S}_2^{(\mathrm{n})}$ and $\mathbf{S}_3^{(\mathrm{n})}$ denote sensor locations and the triangle $\mathbf{X}_\mathrm{S}$ denotes the impact location.

For simplicity, we focus on comparing the described method and the method of [17] when $\tau_{2,3}^{(n)} \neq 0$. Substituting for the sensor coordinates above in (2-14) we get

$$\begin{aligned} \alpha^{(n)} &= -\tau_{2,1}^{(n)} d \\ \beta^{(n)} &= \tau_{2,3}^{(n)} d \\ \gamma^{(n)} &= \left(-\tau_{2,1}^{(n)} x_2^{(n)} + \tau_{2,3}^{(n)} y_2^{(n)}\right) d\,. \end{aligned} \tag{2-23}$$

With N sensor clusters, the objective function of the described method can be written as

$$f = \sum_{n=1}^{N} (\,\alpha^{(n)} x_S + \beta^{(n)} y_S - \gamma^{(n)})^2\,. \tag{2-24}$$

Substituting (23) into (24) and cancelling the common factor d^2, this expression becomes

$$f = \sum_{n=1}^{N} [\,\tau_{2,1}^{(n)} x_S - \tau_{2,3}^{(n)} y_S + (-\tau_{2,1}^{(n)} x_2^{(n)} + \tau_{2,3}^{(n)} y_2^{(n)})]^2\,, \tag{2-25}$$

The method in [17] used only two sensor clusters. Two straight lines passing through the impact and the sensor clusters were identified. The impact location was estimated as the intersection of these two straight lines. In the described method, more than two sensor clusters are used and the impact location is estimated by minimizing an objective function given by

$$f = \sum_{n=1}^{N} (\,k^{(n)} x_S + b^{(n)} - y_S)^2\,, \tag{2-26}$$

where N is the total number of sensor clusters and k_n and b_n are the slope and intercept, respectively, of a straight line corresponding to the DOA to the n^{th} sensor cluster and computed as

$$\begin{aligned} k^{(n)} &= \frac{\tau_{2,1}^{(n)}}{\tau_{2,3}^{(n)}} \\ b^{(n)} &= -\frac{\tau_{2,1}^{(n)}}{\tau_{2,3}^{(n)}} x_2^{(n)} + y_2^{(n)}. \end{aligned} \tag{2-27}$$

Substituting (2-27) into (2-26), the objective function can be expressed as

$$f = \sum_{n=1}^{N} [\frac{\tau_{2,1}^{(n)}}{\tau_{2,3}^{(n)}} x_S - y_S + (-\frac{\tau_{2,1}^{(n)}}{\tau_{2,3}^{(n)}} x_2^{(n)} + y_2^{(n)})]^2\,. \tag{2-28}$$

Multiplying each summation component in the objective function in equation (2-25) by the scaler $\frac{1}{\tau_{2,3}^{(n)}}$, this objective function becomes identical to that presented in [17] and given in equation (2-28). However, the described method provides a more balanced weighting of x_S and y_S in the objective function. Specifically, let us focus on the n-th terms in the objective functions in equations (2-25) and (2-28). For the described method, this term is

$$f^{(n)} = [\tau_{2,1}^{(n)} x_S - \tau_{2,3}^{(n)} y_S + (-\tau_{2,1}^{(n)} x_2^{(n)} + \tau_{2,3}^{(n)} y_2^{(n)})](-d). \tag{2-29}$$

For the method in [17], the corresponding term is

$$f^{(n)} = \frac{\tau_{2,1}^{(n)}}{\tau_{2,3}^{(n)}} x_S - y_S + (-\frac{\tau_{2,1}^{(n)}}{\tau_{2,3}^{(n)}} x_2^{(n)} + y_2^{(n)})\ . \tag{2-30}$$

We can see that equation (2-30), from the method in [17], can be obtained by adding a scaler $\frac{1}{\tau_{2,3}^{(n)}(-d)}$ to equation (2-29) from the described method. Since d is constant, we focus on $\frac{1}{\tau_{2,3}^{(n)}}$ as the scaler. As a result, the behavior of the weight of $f^{(n)}$ among the objective function is affected by $\frac{1}{\tau_{2,3}^{(n)}}$ for the method in [17].

2.2 Time of Arrival Estimation

The time-difference-of-arrivals, $\tau_{i,j}^{(n)}$, need to be calculated from sensor measurements before impact location estimation can be performed. The experiments performed in this research used piezoelectric sensors that produced output voltages as a function of time. Because different frequency components of the waves travel at different speeds in an anisotropic structure, the TDOAs cannot be obtained by directly calculating the cross correlation between two sensor signals and selecting the time difference of arrival as the lag at which the maximum correlation is reached.

Since

$$\tau_{i,j}^{(n)} = t_i^{(n)} - t_j^{(n)}, \tag{2-31}$$

we first estimate the TOAs and then calculate the TDOA using (31). In this work, we consider only the times at which the initial components of the AE signal arrive at the sensor. For sufficiently long travel paths, estimating the time of the fastest mode of propagation has the benefit of mitigating the difficulties caused by overlapping modes of wave propagation travelling at different speeds.

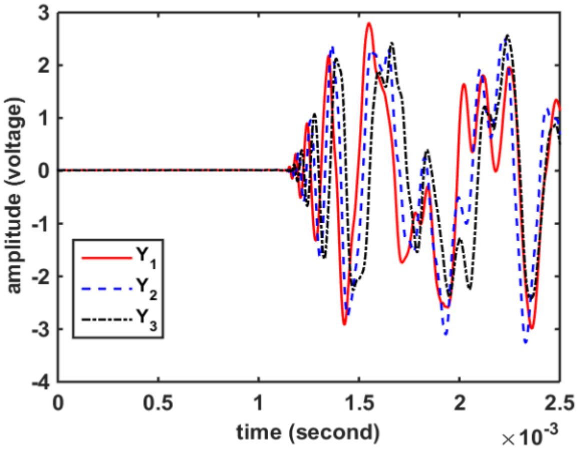

Figure 2-4. Sensor signals in one cluster. The three sensor signals, $\boldsymbol{Y}_1$, $\boldsymbol{Y}_2$ and $\boldsymbol{Y}_3$, are represented by red, blue and black dashed curves.

The TOA estimation method considers all three sensor measurements in the same cluster simultaneously. The method first identifies the fastest arriving signal segment in the sensor signals. The approach assumes that the signal components of all three sensor signals in a cluster are highly correlated. Let the three sensor signals in one cluster be represented by the vectors $\mathbf{Y}_1$, $\mathbf{Y}_2$ and $\mathbf{Y}_3$, where the order is immaterial to this discussion. Let the signal length be L samples. Figure 2-4 provides an example of the three signal segments in one cluster. The estimation method for the n-th sensor cluster involves the following steps.

Step 1: Coarse TOA estimation

In this step, a coarse TOA estimate of the signals $\hat{t}_i^{(n)}$ is made at each sensor in every cluster located on the structure. The method used for the coarse TOA estimation is somewhat structure-dependent, and these estimates will be refined to obtain the final TOA values in subsequent steps.

Two approaches were considered for coarsely estimating the TOAs. In the first approach, a running variance estimate was computed from a sliding five-sample window at each time increment. The initial TOA estimate was chosen as the time at which this variance exceeded a specified threshold. The threshold may be selected based on noise-only measurements made on the structure prior to deployment or testing. In the second approach, the initial TOA estimate was chosen simply as the time at which the sensor signal amplitude exceeded a pre-selected threshold.

Step 2: Detection of the reference segment

A segment of the sensor signal $\mathbf{Y}_1$ surrounding the preliminary TOA location $\hat{t}_1^{(n)}$ and extending through several amplitude peaks on both sides of $\hat{t}_1^{(n)}$ was identified as a reference segment. The number of amplitude peaks on each side of $\hat{t}_1^{(n)}$ was determined by cross validation. The reference segment is shown as a red solid curve in Figure 2-5.

Step 3: Detection of similar segments

Sensor signals in the same cluster are typically highly correlated with each other as evidenced by the experimental measurements shown in Figure 4. The segments in $\mathbf{Y}_2$ and $\mathbf{Y}_3$ that are the most similar to the reference segment in $\mathbf{Y}_1$. were detected by comparing the reference segment in $\mathbf{Y}_1$ with the signal around $\hat{t}_i^{(n)}$ in $\mathbf{Y}_i$, for $i = 2,3$. For each signal, candidate segments were identified that exhibited a correlation coefficient with the reference segment that was larger than a pre-selected threshold. The similar segment was selected as that which minimized the root-mean-square error with the reference segment. In Figure 5, the solid blue and black curves were selected as the similar segments in $\mathbf{Y}_2$ and $\mathbf{Y}_3$, respectively.

Step 4: TOA estimation

TOAs were estimated from the three signal segments identified in Step 2 and Step 3. The time corresponding to the peak amplitude for each of the three AE signal segments were selected as the TOAs $t_i^{(n)}$ for $i = 1,2,3$. Figure 2-5 shows an example of the TOA estimation results. The solid vertical straight lines denote the TOAs for sensor signals of the same color.

2.3 Performance Evaluation

The performance of the algorithm was assessed in two steps. In the first step, extensive simulations of a composite panel were performed to understand the capabilities of the algorithm and to design the experimental set up. In the second step, experiments were performed using two different types of composite panels.

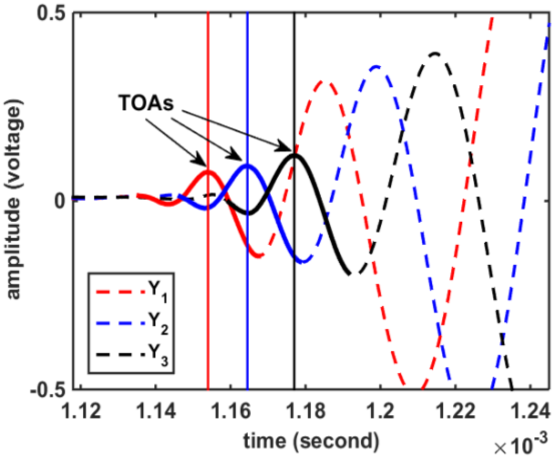

Figure 2-5. TOA estimation results for one sensor cluster. Sensor measurements are zoomed in from Figure 2-4. Curves are sensor signals and vertical straight lines are the TOAs for sensor signals of the same color.

2.3.1 Simulation Analysis

A flat 117 cm square anisotropic panel was used in the simulations. The size of this panel was comparable to that of the carbon/epoxy composite panel used for experimental validation. The impact locations were selected randomly on the panel but not at the sensor locations. The impact signal was modeled as

$$\begin{aligned} s_0(t) = [&\cos(2\pi f_1 t + \eta_1) + \cos(2\pi f_2 t + \eta_2) + \\ &\cos(2\pi f_3 t + \eta_3) + 0.5\cos(2\pi f_4 t + \eta_4)]w(t)\ , \end{aligned} \tag{2-32}$$

where $f_1 = 20$ kHz, $f_2 = 30$ kHz, $f_3 = 40$ kHz, $f_4 = 50$ kHz, η_i for $i = 1,\cdots,4$, were random phase values uniformly distributed in $[-\pi,\pi)$, and $w(t)$ was a Hann window function given by

$$w(t) = \begin{cases} \frac{1}{2}(1 - \cos\frac{2\pi t f_s}{L}) & ; 0 \leq \mathrm{t} < \mathrm{L} \\ 0 & ; \text{otherwise.} \end{cases} \tag{2-33}$$

where f_s is the sampling frequency and L is the length of the signal. The impact signals were assumed to propagate with varied velocities along different directions according to

$$v_i = \frac{v_{\max} - v_{\min}}{2}\cos(\varphi_i) + \frac{v_{\max} + v_{\min}}{2}\ , \tag{2-34}$$

where φ_i is the angle between the signal travel path (from the impact to the ith sensor) and the x-axis, and $v_{\max} = 1$ km/s and $v_{\min} = 0.9$ km/s are the maximum and minimum velocities, respectively, of wave propagation in the panel. Attenuation during wave propagation was modeled using an exponential function. Thus, the i-th sensor signal was modeled as

$$s_i(t) = e^{-d_{S,i}\lambda} s_0(t - \frac{d_{S,i}}{v_i}) + \sigma\xi(t)\ , \tag{2-35}$$

where $\xi(t)$ is a zero-mean Gaussian, white noise with unit variance and $\lambda = 0.002\ \mathrm{cm}^{-1}$. The parameter σ controlled the signal-to-noise ratio of the sensor signal. Note that this signal model does not include the effects of multiple modes and reflections present in practice.

The three sensors in each cluster were placed at the vertices of an isosceles right triangle. The location of the mid-point of the hypotenuse of this triangle was defined as the cluster location. For each independent simulation, the orientation of the triangles formed by the sensors were randomly selected and the sensor clusters were randomly placed in the shaded area of Figure 2-6. The radii of the circles defining the shaded area were $r_{min} = 34.5$ cm and $r_{max} = 39.6$ cm, respectively. Let θ_i, for $i = 1,2,\cdots,N$, denote the angles formed by the i-th sensor cluster, the mid-point of the panel and the adjacent sensor cluster. The angles $\theta_1, \theta_2, \cdots, \theta_N$ were uniformly generated in the interval $(\frac{2\pi}{N} - (\frac{2\pi}{N} - \frac{2\pi}{N+1}), \frac{2\pi}{N} + (\frac{2\pi}{N} - \frac{2\pi}{N+1}))$, where N is the number of sensor clusters.

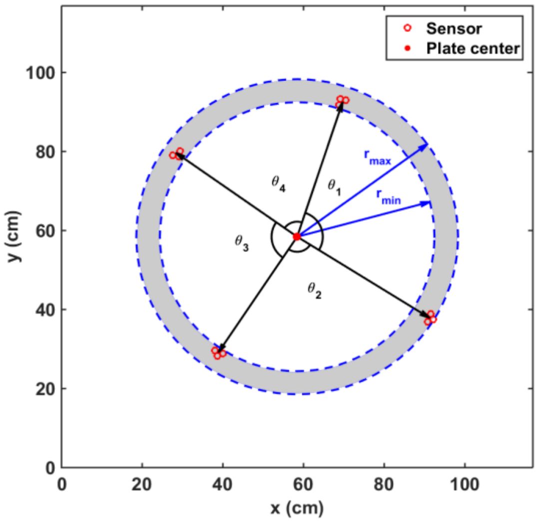

Figure 2-6. Sensor distribution for four sensor clusters ($N = 4$). The cluster locations were randomly generated in the grey area bounded by two circles, whose centers were at the mid-point of the panel and radii denoted by r_{min} and r_{max}, respectively. θ_i, for $i = 1,2,3,4$, denotes the angle between two adjacent sensor clusters.

The sensor separation distance was defined as the length of the equal sides of the isosceles triangle formed by the sensors in one cluster. TOAs were estimated from impact signals using a sampling rate of 2 MHz. The results presented in this section are averages obtained from 5,000 independent simulations.

2.3.2 Effect of Sensor Separation

The sensor separation distance was changed from 0.5 cm to 5 cm in 0.5 cm increments. The simulations for this analysis employed five sensor clusters and used a signal-to-noise ratio (SNR) of 40 dB. As shown in Figure 2-7, the root-mean-square (RMS) location-estimation error is smallest for a sensor separation of 1.5 cm. Further analysis revealed that the TDOA estimation became less accurate as the sensor separation is reduced. However, the approximation of the common velocities of the waveforms traveling to the three sensors in a cluster becomes less accurate as the sensor separation is increased. Consequently, the selection of the best-suited sensor separation distance is a tradeoff between the accuracy of the TDOA estimation and the velocity approximation. Based on the simulation results shown in Figure 2-7, the sensor separation distance was set to 1.5 cm in the remaining simulations as well as the experiments.

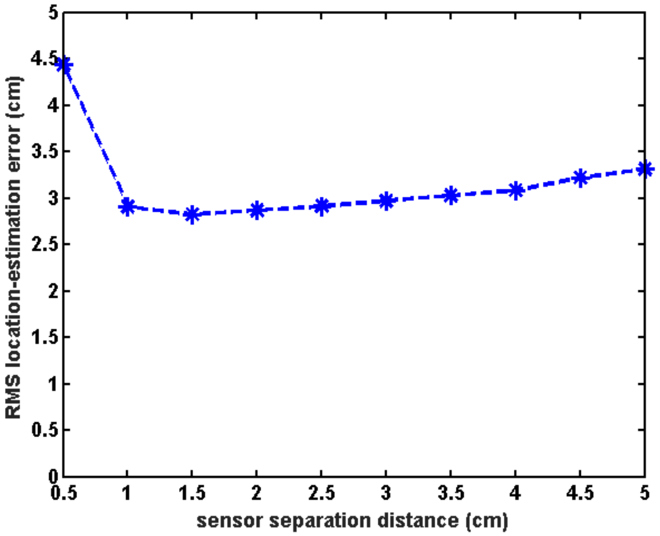

Figure 2-7. RMS location-estimation errors for different sensor separation distances.

2.3.3 Effect of the Number of Sensor Clusters

In this set of simulations, the number of sensor clusters used to estimate the impact locations was varied from two to eight. The simulations used SNR = 40 dB and 1.5 cm sensor-separation distance. As shown in Figure 2-8, the RMS location-estimation error decreases with increasing number of sensor clusters. However, the performance improvements obtained by using more than five sensor clusters may not be worth the associated increase in the complexity of the estimator. Therefore, five sensor clusters were utilized in the remaining simulations as well as in the experiments.

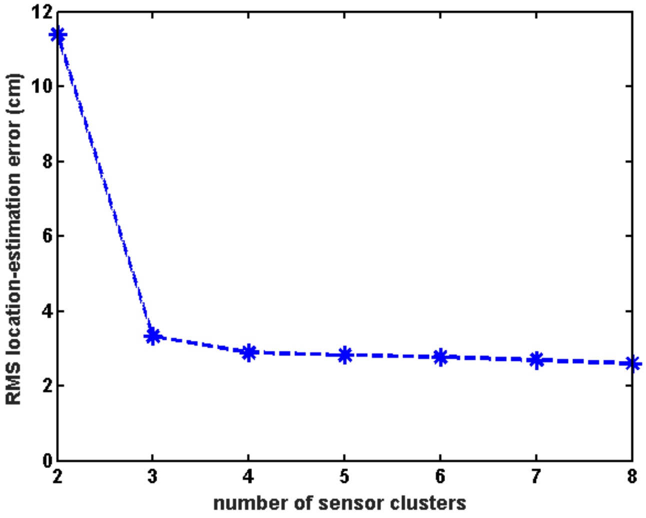

Figure 2-8. RMS location-estimation errors for different number of sensor clusters.

2.3.4 Effect of Signal to Noise Ratio

To further analyze the performance of the algorithm when the sensor signals become noisy, simulations were performed in which the signal to noise ratio (SNR) was varied from 15 dB to 50 dB in 5dB increments. Five sensor clusters were used and the sensor separation distance was 1.5 cm. The simulation results are shown in Figure 2-9. As expected, the RMS location-estimation errors decrease with increasing SNR. At higher SNRs, the errors due to the velocity approximation dominate the effect of noise. Consequently, the rate at which the RMS error decreases is relatively small for large SNRs.

2.4 Experimental Validation

The impact location estimation algorithm was experimentally validated using both a monolithic composite panel and a composite sandwich panel. The experiments used Acellent Single Smart Layer piezoelectric sensors. Five sensor clusters were used with a sensor separation distance of 1.5 cm, the optimal separation determined from the simulations. The variation in sensor separation due to sensor attachment errors was less than 0.1 cm. Sensor signals were acquired using a 32-channel National Instruments PXIe-1073 data acquisition system. The data sampling rate was 2×10^6 samples/s/channel, and the data was acquired with a resolution of 14 bits/sample. The panels were impacted by dropping a steel ball (1.3 cm diameter) from a height of 25.4 cm and the corresponding sensor signals were recorded and stored for further analysis.

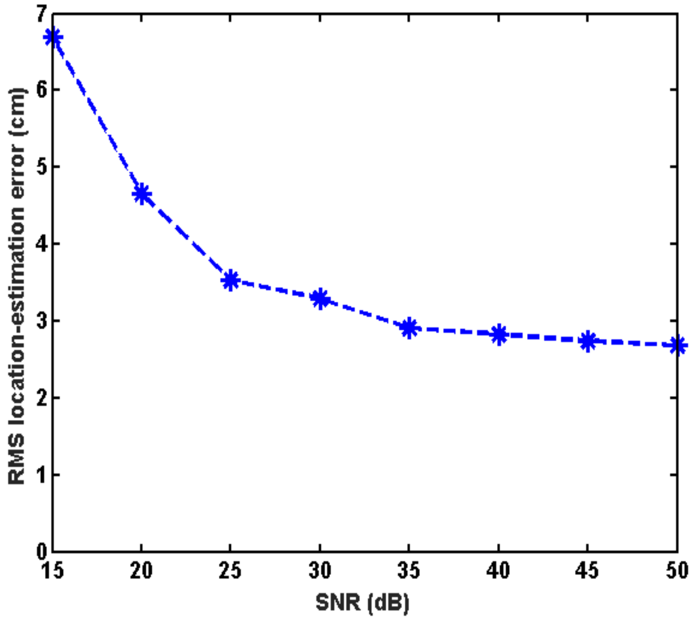

Figure 2-9. RMS location-estimation errors for different SNR values.

2.4.1 Experiments on a Quasi-Isotropic Composite Panel

The first panel was a 117 cm square quasi-isotropic carbon/epoxy composite laminate of 0.3 cm thickness. The panel was fabricated using a total of 24 plies of unidirectional carbon/epoxy prepreg tape with a $[0/45/90/-45]_{3s}$ ply stacking sequence. The sensor and impact locations were as illustrated in Figure 2-10. A total of 49 impacts were performed: 25 *inner* impacts that were at least 20 cm away from the boundaries to avoid the effects of signal reflections and 24 *outer* impacts located closer to the boundaries. The inner impacts and outer impacts are denoted by blue dots and black asterisks, respectively, in Figure 2-10. The composite panel was impacted one time at each location.

The performance of the location estimation method was investigated when two, three, four and five sensor clusters were used. The RMS location-estimation errors calculated for each condition are shown in Table 2-2. When using two sensor clusters, each of the 10 possible sensor cluster combinations from the five clusters on the panel was evaluated. Since there were 25 impact locations, a total of 250 impact location estimates were evaluated using two sensor clusters. Similarly when using three, four and five sensor clusters, there were 250, 125 and 25 estimates, respectively.

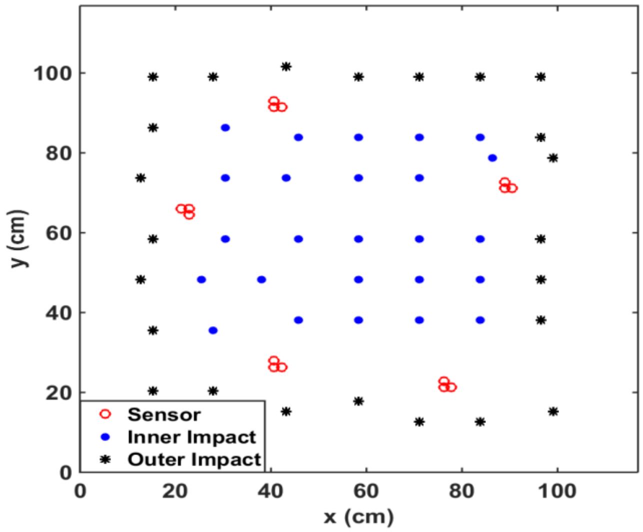

Figure 2-10. Sensor locations and impact locations on the quasi-isotropic composite panel.

Table 2-2. RMS Location Estimation Error (cm) for Impacts on the Quasi-Isotropic Composite Panel

Impacts	**Method I**					**Method II [17]**				
	Number of Sensor Clusters									
	2	3	4	5	3*	2	3	4	5	3*
All Impacts	14.0	6.8	5.4	4.7	3.7	28.5	7.7	6.2	5.3	3.6
Inner Impacts	13.3	5.3	4.1	3.6	3.6	20.0	5.9	4.8	4.5	3.5
Outer Impacts	14.8	8.0	6.5	5.6	3.8	35.3	9.2	7.3	6.1	3.7

*Three closest sensor clusters were used.

In Table 2-2, Method I corresponds to the approach presented in this report. The method of [17] was applied as a comparison and the results are tabulated under Method II in Table 2-2. For all 49 impacts and for both methods, increasing the number of clusters from two to five decreased the RMS location-estimation error. Method I exhibited smaller RMS location-estimation errors than Method II when the same number of sensor clusters were used. When five sensor clusters were used for Method I, 80% of the location estimates had errors less than 5 cm and the largest error was 12.5 cm. In comparison, 67% of impacts were located within 5 cm using Method II, and the largest error was 13.1 cm. Similarly for the 25 inner impacts and the 24 outer impacts, the RMS location-estimation error became smaller when more sensor clusters were used and Method I had smaller location estimation errors than Method II.

To mitigate the reflections from the boundaries, a modified impact location estimation method was presented in this chapter that used the three sensor clusters closest to the impact to estimate the location. The estimation results using the three closest sensor clusters are also shown in Table 2-2. For both methods, the location estimation error reduced substantially for the outer impacts. This result was expected, as reflections from the boundaries cause difficulties to the TOA estimation process and therefore to the impact location estimation process. Improvements in location estimation performance were greatest for Method II for this structure. For impacts sufficiently removed from the boundaries, significant improvements were not expected by utilizing only the nearest three sensor clusters. However, the experimental results for this structure showed an improvement for Method II in the location estimation performance even for the inner impacts when the three nearest sensors to the impact were used.

2.4.2 Experiments on a Composite Sandwich Panel

To further evaluate the performance of the proposed impact location estimation method, additional experiments were performed using a 60 cm square composite sandwich panel of 1.6 cm thickness. The facesheets of the sandwich panel were 1.3 mm thick woven-carbon/epoxy laminates. The facesheets were bonded to an aluminum honeycomb core. The primary objective of this experiment was to validate the robustness of the location estimation method to temperature variations. Additionally, this experiment was used to investigate the performance of the location estimation method when the impact occurs on the opposite surface of the sandwich panel from which the sensor clusters are mounted, Consequently, analyses were limited to impact locations away from the boundaries of the panel as well as impact location estimation using the three closest sensor clusters as identified by TOA measurements.

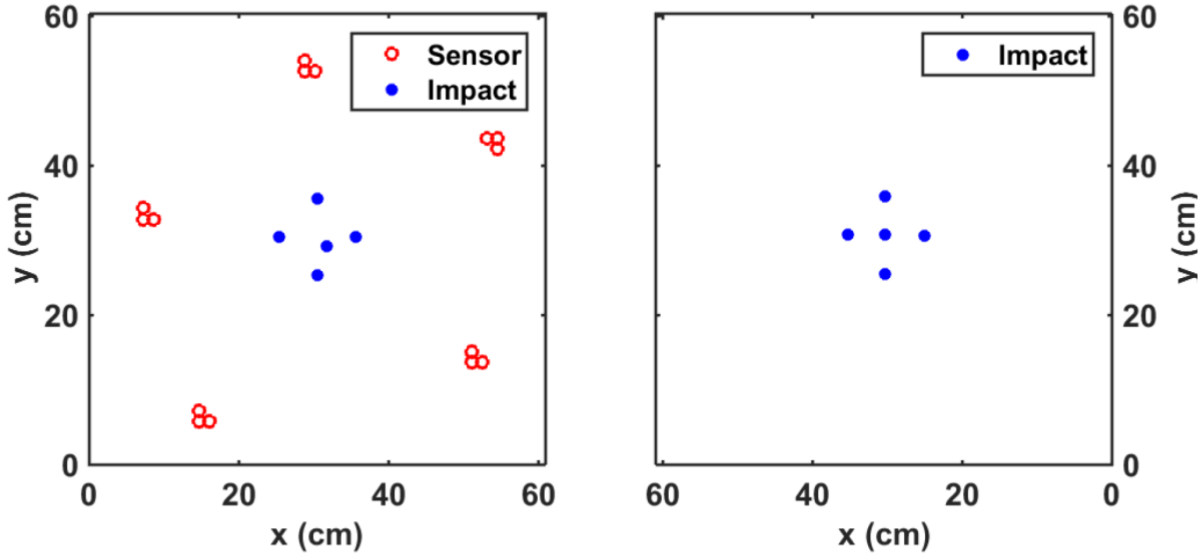

Figure 2-11. Sensor and impact locations on the composite sandwich panel. The lower-left corner from the top surface of the panel is the origin. (a) Top surface of the panel; (b) Bottom surface of the panel.

The sandwich panel was impacted ten times at five different locations on both the top and bottom surfaces as shown in Figure 2-11. Thus, a total of 50 impacts were performed on the top and bottom surfaces. A total of five sensor clusters were attached to the top surface of the panel. Impact experiments on the top surface of the panel were performed in an environmental chamber at three different temperatures: 21°C, 51°C and 66°C. The temperature of the panel was monitored using temperature sensors placed on both the top and bottom surfaces. The received AE signals were analyzed by the two methods using two, three, four and five sensor clusters. Note that for the case of two and three clusters, there is no “closest" sensor cluster selection to be implemented.

The RMS location-estimation errors shown in Table 2-3 indicate that both methods are robust to temperature variations. As expected, the location-estimation error decreased substantially with an increasing number of sensor clusters. Furthermore, the described location estimation method resulted in smaller errors for all cases considered when compared with the method in [17]. With the AE sensors mounted on the top surface of the sandwich panel, both location estimation methods exhibited similar location estimation performance for impacts on the top and bottom surfaces of the composite sandwich panel.

The location estimation errors produced using the three closest sensor clusters were larger than those produced using five sensor clusters. This result was not unexpected, as the impact locations were all located a sufficient distance from the boundaries of the structure. However, location estimates using the three closest sensor clusters were more accurate than those obtained using four sensor clusters for both methods. Unlike for the quasi-isotropic composite panel, Method I performed substantially better than Method II when using the three closest sensor clusters.

Table 2-3. RMS Location Estimation Error (cm) for Impacts
on the Composite Sandwich Panel

Impact Condition	**Method I**					**Method II [17]**				
	Number of Sensor Clusters									
	2	3	4	5	3*	2	3	4	5	3*
Top surface impact, 21°C	14.4	5.6	3.9	2.8	3.7	18.9	6.6	4.8	2.9	4.5
Top surface impact, 51°C	13.2	5.6	4.0	3.0	3.3	24.3	6.7	4.9	3.1	4.7
Top surface impact, 66°C	12.9	5.5	3.9	2.8	3.3	19.9[+]	6.4	4.8	3.2	4.6
Bottom surface impact, 21°C	14.2	5.7	3.9	2.8	3.4	19.4	6.8	4.9	3.0	4.0

*Three sensor clusters closest to the impact location were used.

[+] In 7 out of 500 estimates, the estimation errors were extremely large (larger than 200 cm). These cases were excluded from the results.

2.5 Summary and Conclusions

This chapter presented an AE-based impact location estimation algorithm for use with composite structures. The algorithm was formulated as a constrained optimization problem by utilizing sensor locations and times of arrival of impact signals at the sensors. As a result, impact locations are estimated without any wave propagation velocity information. A modification of the algorithm to overcome difficulties caused by waveform reflections enabled accurate estimation of impact locations close to the structure's boundaries. The capability of this algorithm to accurately estimate impact locations was demonstrated numerically and experimentally. Experiments performed at different temperatures showed that the algorithm was robust to temperature changes. An automatic time-of-arrival estimation method was also developed. The performance capabilities of the method and its computational simplicity make this approach an attractive alternative to other methods available in the literature for practical structural health monitoring applications.

3. ACOUSTIC EMISSION-BASED DAMAGE CLASSIFICATION FOR COMPOSITE STRUCTURES

Damage classification is an important aspect of damage assessment. When the SHM system determines that an impact event has occurred, we also wish to decide whether the impact caused damage to the structure. If the impact caused damage, we also wish to determine what type of damage was created. The goal of this task was to determine from the AE signals if the impact caused damage, and if so to classify the damage type as delamination or a mixture of delamination and fiber breakage with an efficient classifier.

There are many published works on damage classification for different materials and different types of damage. In [25], Gutkin et al. investigated the damage types in carbon fiber reinforced plastics using AE signals. Peak amplitude, peak frequency, energy, rise time and signal duration were the features used for damage classification. The k-means algorithm, self-organizing map algorithm combined with k-means (SOM/k-means) and a neural network algorithm were compared and Gutkin et al. concluded that the SOM/k-means algorithm was better than the other two in terms of quality and computational effort. Frequency range distributions corresponding to different damage types, which were matrix cracking, delamination, fiber/matrix debonding, fiber failure and fiber pull-out, for compact compression specimen were obtained from SOM/k-means algorithm. In [26], Shahidan et al. classified damage in a reinforced concrete beam resulting from different loading levels with a simplified cyclic load test system. Four AE sensors monitored the beam at different ranges. The peak amplitude, rise time, average frequency and signal strength were the features and they presented separable clusters for 20%, 50%, 80% and 100% of the ultimate load.

Kim et al. classified two types of damage: delamination with minimal fiber damage and fiber-breakage with minimal delamination in [27]. Drop-weight with low-velocity impact experiments under different boundary conditions of the specimen were designed. The root-mean-square values of the AE signals in time and frequency domain were the criteria used for the classification. Frequency ranges corresponding to the two types of damages were analyzed. The amplitude of the AE wave is attenuated as the wave propagates through the structures and also the waves get dispersed as they travel through composite materials. Therefore, in [28], Ramirez-Jimenez et al. considered the dominant frequency of the wave over amplitude-based analysis as the most relevant characteristic. The authors classified three types of damage: fiber/matrix debonding, fiber slippage and fiber pull-out, and fiber breakage, in glass/polypropylene composites. The experiment was tensile loading test on an Instron 4550 universal test machine and a broadband piezoelectric sensor was used. The power spectrum of the fast Fourier transformation of the sensor signals was analyzed. The primary frequency was extracted for each event and was plotted against the progress of the test. The experiment showed clusters around well-defined frequencies. Scanning electron microscope micrographs of the damaged specimen were studied to verify the type of damage. Finally, the frequency ranges for each of the three types of damage were determined. Reference [29] also utilized frequency-based analysis. This paper studied and classified four different types of damage on unidirectional composite specimens. The tensile test machine was applied. The AE signals were analyzed by implementing a burst spectrum analyzer (BSA). It was shown in the paper that matrix cracking, fiber failure, debonding and fiber pull-out resulted in signals with significant strength in different frequency ranges. Wavelet transformation is a very popular method for feature extraction. For instance, in [30], Yan et al. classified different size of crack damage in a honeycomb sandwich panel using a dynamic finite element model. The structural response signal was first decomposed into several sub-signals in different frequency bands using wavelet analysis. The features were designed according to the ratio between the energy of the sub-signals from the undamaged panel and the crack damaged panel. The features obtained from different wavelets components were compared and shown to be sensitive to small crack damage in the sandwich panel.

References [31] and [32] studied features of signals from piezoelectric transducers rather than AE signals which were of interest in the current investigation. However, some features could be applied to AE signals as well. In [31], Ying, et al. detected whether a steel pipe is damaged. A mass scatterer was used to simulate damage in the pipe and two piezoelectric transducers were used as the transmitter and receiver. Baseline signals before applying the mass scatterer were obtained. Different sets of signals using the mass or after removing the mass were collected. A total of 303 features were extracted from time and frequency domains. Examples of features included peak-to-peak value, amplitude of the 1st/2nd/3rd greatest peaks, curve length and cross-correlation coefficient. Three classifiers were employed: adaptive boosting, modified adaptive boosting and support vector machine. Ying et al. increased the number of features to 365 in [32] and the features were organized as baseline-free and baseline-dependent. Feature selection was implemented by adaptive boosting and the performance enhancement using the selected features was analyzed. There are many other popular classification algorithms applied to damage classification as well, such as artificial neural networks (ANN) [33, 34], principal component analysis (PCA) [35], and matching pursuit decomposition (MPD) based algorithm [36,37].

In this chapter, we present a data-driven machine learning approach to detect and classify damage in carbon/epoxy composite materials and identify useful AE data components and features. A machine learning classifier, the logistic regression algorithm, feature extraction and a LASSO-based feature selection procedure are described, along with extensive experimental results.

3.1 Experimental Design

The classifier for detecting damage as well as for determining the type of damage is designed based on experimental data. Controlled laboratory experiments were designed to generate the damage of interest. The structures used in experiments were IM7/8552 carbon/epoxy composite panels with a $[0/90]_{2s}$ orthotropic layer stacking sequence. The panels were 2.2 mm to 2.5 mm thick, 152.4 mm wide and 304.8 mm long, which was the largest size that fit into the pneumatically-assisted Instron Dynatup 8250 HV drop tower used in the experiments. A hemispherical impactor and a sharp impactor were used, as shown in Figure

3-1. The dimensions of impactors and the total drop weights are listed in Table 3-1. The drop-weight height varied from 25 mm to 254 mm with 25 mm increments.

3.1.1 Support Conditions for the Composite Panel

The support condition for the composite panel has direct effect on the deformation during impacting. A 2.5 mm thick silicone rubber pad and a metal panel of size 152 mm x 432 mm x 19 mm were used to support the panel. The layer order from top to bottom was the panel, the rubber pad and the metal panel. By using two different metal panels in the experiments, two different support conditions were achieved. The first was the back-supported condition, which used a metal panel without a hole. The second option was the edge-supported condition, which used a metal panel with a hole of size 76 mm x 127 mm. The two support conditions are shown in Figure 3-2. Using the edge-supported condition, the hole was located under the impacted area of the composite panel to produce greater bending deformation.

Figure 3-1. Hemispherical impactor (top) and sharp impactor (bottom).

Table 3-1. Dimensions of the Impactor and Total Drop Weight

Impactor	**Impactor Diameter (mm)**	**Total drop weight (kg)**
Hemispherical	25.4	4.8
Sharp	2.0	4.2

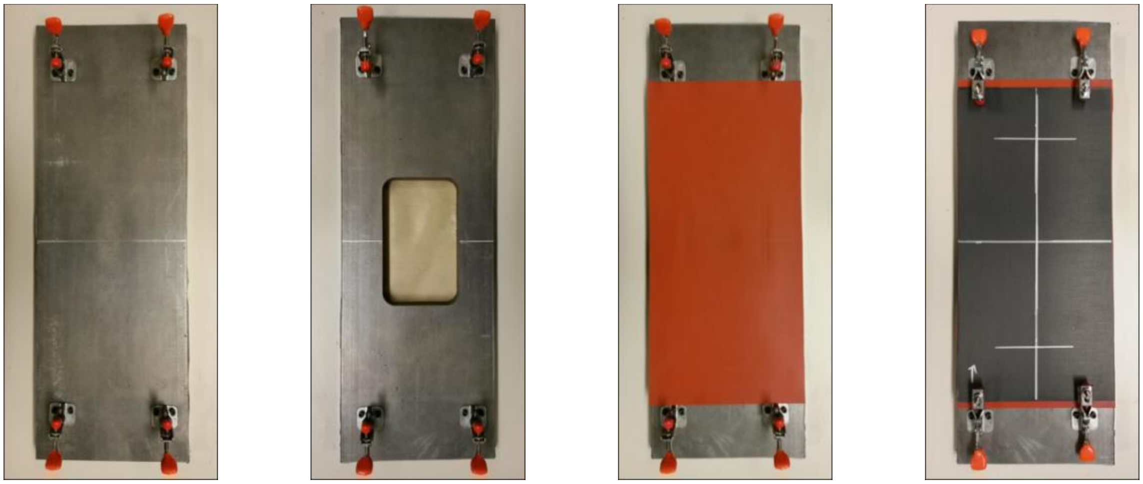

(a) (b) (c) (d)

Figure 3-2. Support conditions for the composite panel. (a) Metal panel without a hole; (b) Metal panel with a hole; (c) Silicone rubber pad laid on the metal panel; (d) Assembly of metal panel, silicone rubber and the composite panel.

After assembling the metal panel, rubber pad and the composite panel together, the four corners of the panel were fixed with clamps. This was done to avoid movement of the composite panel and to mitigate debonding between sensors and the composite panel during impacting. The different experimental conditions were designed to produce different types of damage in the composite panels. Specifically, the sharp impactor would result in fiber cracks more often than the hemispherical impactor. Lower drop-weight height would cause less damage in the panels, but more severe damage could be generated by impacting the panels from higher height. The back-supported condition is used to reduce the global deformation of the panels during impacting and results in greater fiber breakage. In contrast, the edge-support condition results in more bending deformation and tends to produce delamination damage.

3.1.2 Sensor Selection and Experimental Setup

Vallen Systeme's 900M RIC sensors with working frequency range from 100 kHz to 900 kHz, were used in all the experiments described in this chapter. Two sensors were used for each drop-weight impacting experiment. The sensor locations and the impact location on the composite panel are shown in Figure 3-3. The composite panels were impacted at the center and the two sensors were placed equally-distant from the impact location.

A National Instruments data acquisition system (PXIe-1073) with the data sampling rate 2×10^6 samples/channel and a resolution of 14 bits/sample was used to record data from the experiments. Each drop-weight experiment impacted one new undamaged composite panel and AE signals were collected using the two sensors on the panel. A total of 86 experiments with different experimental conditions were performed. The number of experiments selected for different experimental conditions selected are presented in Tables 3-2 to 3-5.

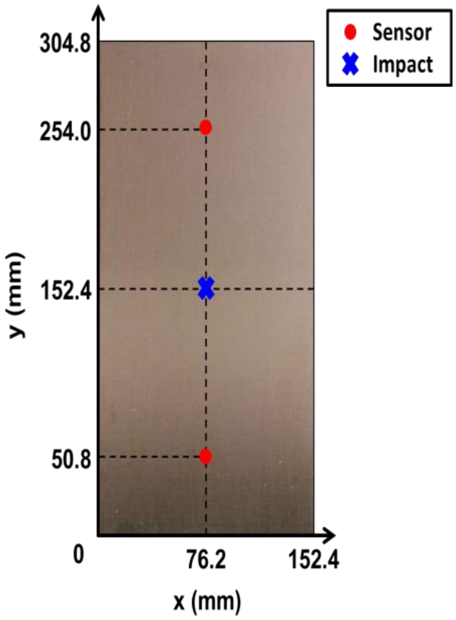

Figure 3-3. Sensor locations and impact location on the composite panel.

.

Table 3-2. Number of Experiments Using the Hemispherical Impactor and the Back-Supported Condition

Drop-weight height (mm)	25	51	76	102	127	152	178	203	229	254
Number of experiments	5	4	6	5	4	4	4	3	2	2

Table 3-3. Number of Experiments Using the Sharp Impactor and the Back-Supported Condition

Drop-weight height (mm)	25	51	76	102	127	152	178
Number of experiments	2	2	5	2	2	2	2

Table 3-4. Number of Experiments Using the Hemispherical Impactor and the Edge-Supported Condition

Drop-weight height (mm)	25	51	76	102	127	178	203	229	254
Number of experiments	5	5	4	1	1	2	3	2	1

Table 3-5. Number of Experiments Using the Sharp Impactor and the Edge-Supported Condition

Drop-weight height (mm)	51	127	178
Number of experiments	2	2	2

3.2 Inspection of Impacted Panels

Non-destructive inspections were performed on the impacted composite panels using ultrasonic C-scan, and destructive inspections using thermal de-ply to characterize damage and use the results for designing and validating the classifiers The C-scan method characterizes the presence of damage on the panel by examining reflected waveforms through the thickness of the inspected composite panel during a certain time gate [38]. For this work, a Sonix ultrasonic inspection system using a 5 MHz Panametrics V309 ultrasonic transducer was used. Three time gates to examine the wave reflections from top laminates, middle laminates and bottom laminates of the panel were applied and the grayscale digital image corresponding to each time gate was obtained.

After the ultrasonic C-scan, a 35 mm x 35 mm area around the impacted area on the composite panel was cut out for further inspection. A destructive inspection based on thermal deply analysis was performed. This procedure examined the damage in more detail, specifically to measure the fiber breakage length. To perform the de-ply analysis, the composite panels were heated in a furnace at 460°C and the epoxy resin pyrolyzed to allow separation the plies. The length of fiber breakage on both sides of each ply was examined using a Dino-Lite digital microscope. Figure 3-4 shows a magnified photo under the microscope of one ply showing multiple fiber cracks. The fiber breakage lengths were measured along the direction orthogonal to the fiber orientation. Finally, the total fiber breakage length was recorded by adding the fiber breakage length of all plies for each composite panel.

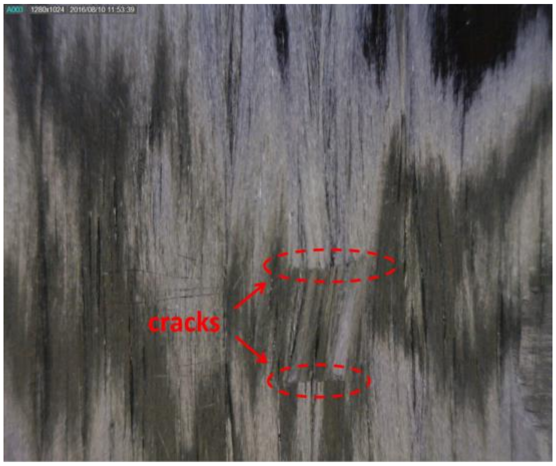

Figure 3-4. Magnified photo of one ply under the microscope.

A summary of the damaged area as determined from the C-scan inspection and the total fiber breakage length measured after thermal de-ply is provided in Figures 3-5 through 3-8 for different impact configurations. As expected, the damaged area and the total fiber breakage length generally increased with the drop-weight height. When the hemispherical impactor and the back-supported condition was used (Figure 3-5), there was no fiber breakage for drop-weight heights lower than or equal to 76 mm. The fiber breakage occurred in some experiments when the drop-weight height increased from 76 mm to 152 mm. Beyond 152 mm, the fiber breakage length became much larger. Fiber breakage occurred more frequently in experiments with the sharp impactor and the back-supported conditions (Figure 3-6). Even with the lowest drop-weigh height, fiber cracks were present and much larger total fiber breakage lengths were obtained than using the hemispherical impactor for high drop-weight height.

When the hemispherical impactor and the edge-support condition were used, no damage was detected for the lowest three drop-weight heights as shown in Figure 3-7. When the height was 102 mm, 127 mm and 178 mm the impacts induced delamination, but no fiber breakage. When the drop-weight height was larger than 178 mm, fiber breakage occurred. Finally a comparison of the results for experiments using the sharp impactor and edge-supported condition (Figure 3-8) with the results for back-supported condition (Figure 3-6) demonstrates that the fiber breakage length is larger for the back supported case for similar drop-weight heights. The edge-supported condition allows more global bending deformation to reduce the occurrence of fiber breakage.

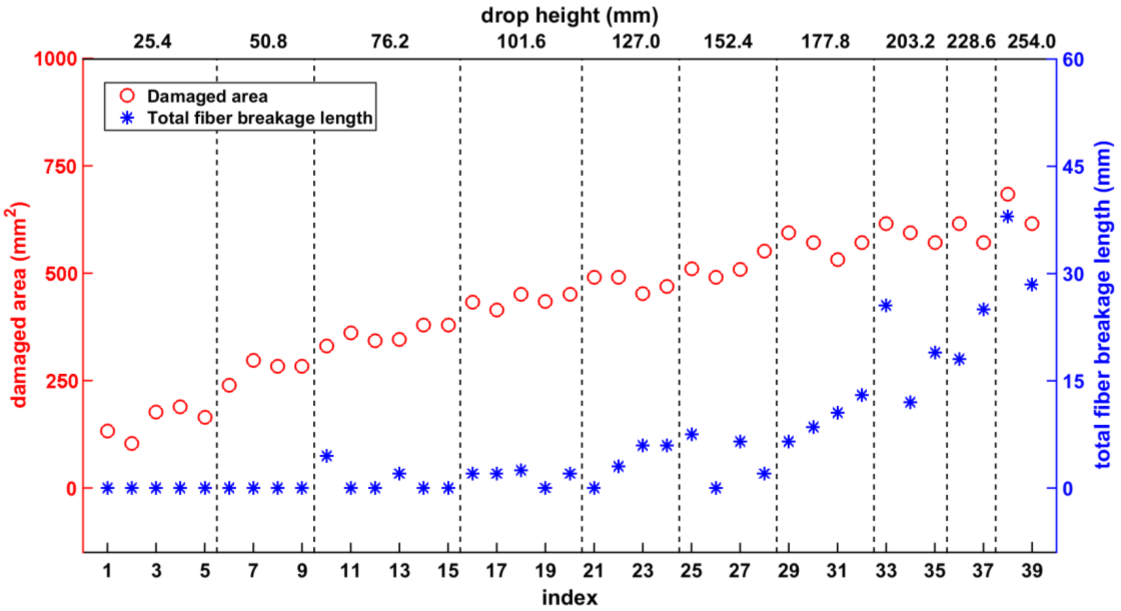

Figure 3-5. Summary of the damaged area and the total fiber breakage length of experiments using the hemispherical impactor and the back-supported condition.

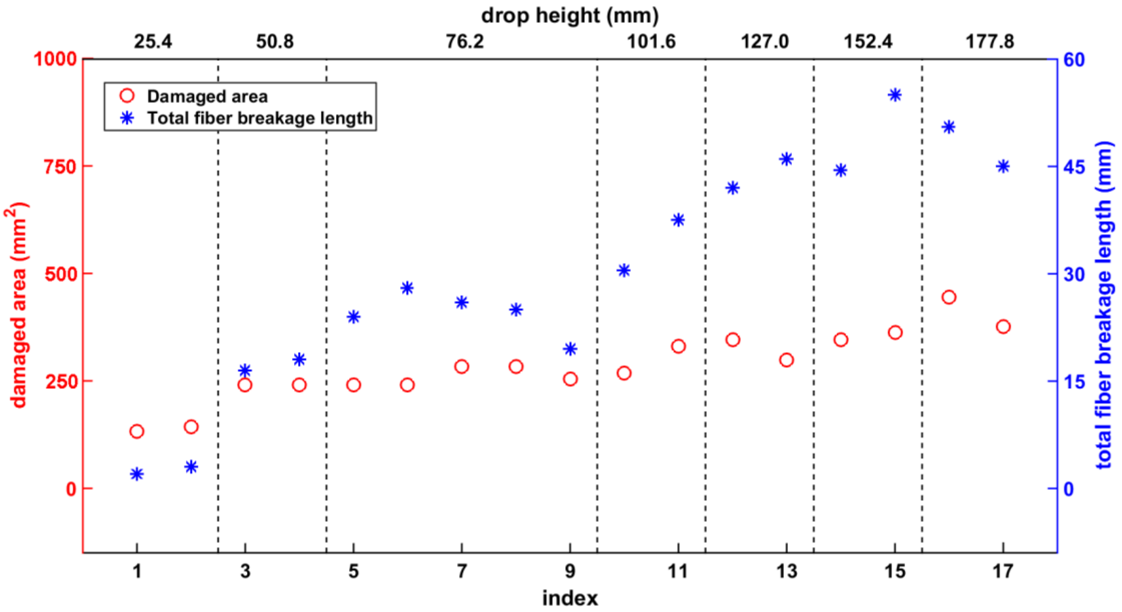

Figure 3-6. Summary of the damaged area and the total fiber breakage length of experiments using the sharp impactor and the back-supported condition.

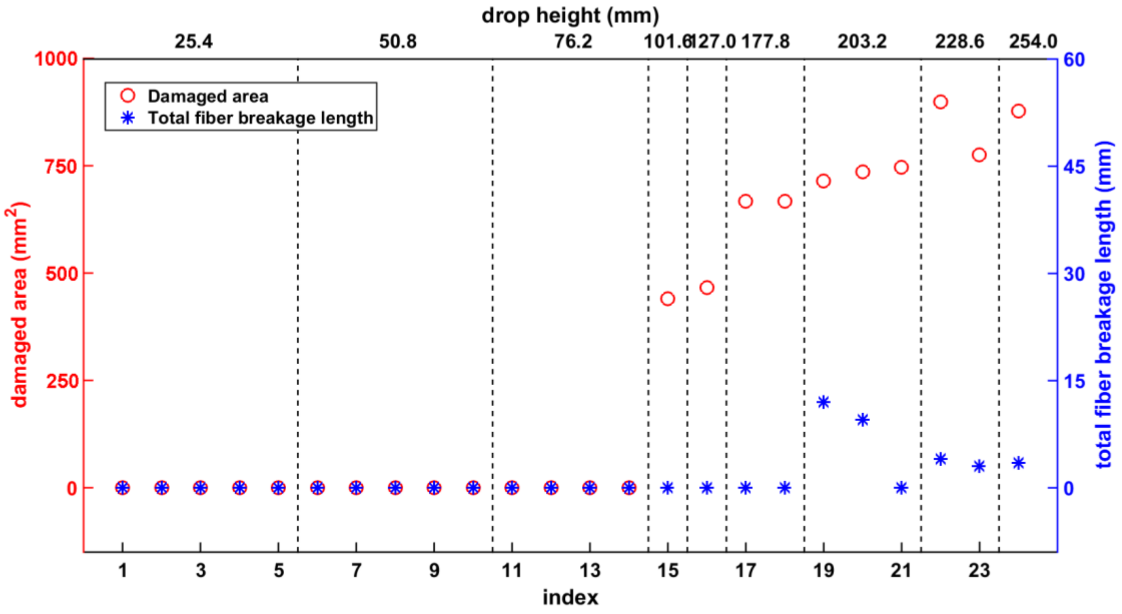

Figure 3-7. Summary of the damaged area and the total fiber breakage length of experiments using the hemispherical impactor and the edge-supported condition.

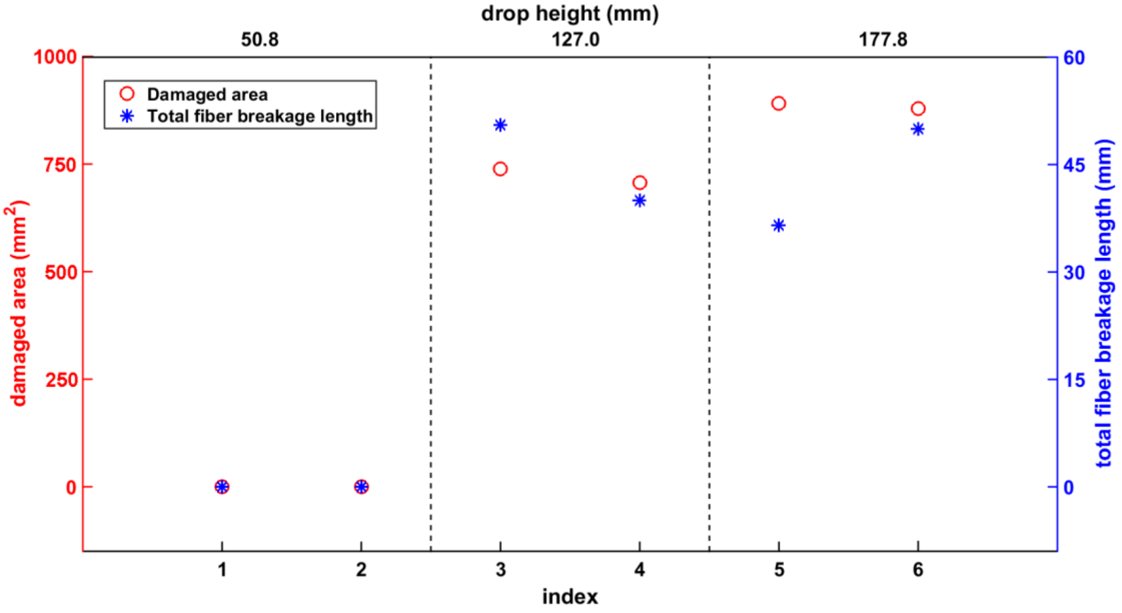

Figure 3-8. Summary of the damaged area and the total fiber breakage length of experiments using the sharp impactor and the edge-supported condition.

Based on the inspection of the impacted specimen, damage states were classified as either undamaged, delaminated with no fiber breakage, or a mixture of delamination and fiber breakage. Of the total of 86 experiments performed, 16 resulted in no damage, 21 resulted in delamination with no fiber breakage, and the remaining 49 involved both fiber breakage and delamination.

3.3 Machine Learning-Based Classification

In this section, we describe a machine learning approach to classifying the results of impacts on the structure. As discussed earlier, we consider two basic problems. The first problem deals with determining if an impact caused damage. The second problem deals with impacts that induced damage in the structure, and we attempt to determine the type of damage as matrix damage (delamination) or a mixture of matrix damage and fiber breakage. Both classifiers are built based on logistic regression, and we describe the general approach to designing a classifier using the logistic regression model next.

3.3.1 Logistic Regression Algorithm

Logistic regression is one of the commonly used and well-known classification algorithms [39, 40]. This method computes the probability that a new observation belongs to a specific class using a parametric model.

Let $y_i \in \{0,1\}$, where i denotes the index of the observations, represent the class label for the feature vector $\mathbf{x}_i$ corresponding to the ith observation (impact). For example, in the problem of determining if an impact caused damage, y_i=1 may correspond to damage and y_i=0 may correspond to the no-damage case. The derivation of this classifier assumes that the conditional probability $\mathbb{P}(y_i = 1|\mathbf{x}_i)$ follows a Bernoulli distribution. In addition, logistic regression assumes the logit transformation of the conditional probability, which maps the probability $\mathbb{P}$ from $[0,1]$ to $[-\infty, +\infty]$, is linear in the entries of the feature vector, *i.e.*,

$$\operatorname{logit}(\mathbb{P}(y_i = 1|\mathbf{x}_i)) = \log\left\{\frac{\mathbb{P}(y_i=1|\mathbf{x}_i)}{1-\mathbb{P}(y_i=1|\mathbf{x}_i)}\right\} = \mathrm{x}_i^T \beta\ , \tag{3-1}$$

where β is the unknown coefficient vector. The conditional probability can be solved from the above equation as

$$\mathbb{P}(y_i = 1|\mathbf{x}_i) = \frac{\exp(\mathbf{x}_i^T \boldsymbol{\beta})}{\mathbf{1}+\exp(\mathbf{x}_i^T \boldsymbol{\beta})}\,. \tag{3-2}$$

Assume that $y_i|\mathbf{x}_i$, for $i = 1, \cdots, M$, are independent of each other, where M is the number of the observations used for training. The unknown coefficient vector $\boldsymbol{\beta}$ may be estimated using a maximum likelihood approach from a training set that is similar in its characteristics to the data that the system will encounter in practice:

$$\max_{\boldsymbol{\beta}} \prod_{i=1}^{M} \mathbb{P}(y_i|\mathbf{x}_i) = \max_{\boldsymbol{\beta}} \left\{ \prod_{i:y_i=1} \mathbb{P}(y_i = 1|\mathbf{x}_i) \prod_{i:y_i=0} \mathbb{P}(y_i = 0|\mathbf{x}_i) \right\}$$
$$= \max_{\boldsymbol{\beta}} \left\{ \prod\nolimits_{i:y_i=1} \frac{\exp(\mathbf{x}_i^T\boldsymbol{\beta})}{1+\exp(\mathbf{x}_i^T\boldsymbol{\beta})} \prod\nolimits_{i:y_i=0} \frac{1}{1+\exp(\mathbf{x}_i^T\boldsymbol{\beta})} \right\} . \quad (3\text{-}3)$$

The above optimization problem has no closed-form solutions. However, the objective function is convex and one can efficiently solve for the unknown parameters using numerical approaches such as Newton's method [41]. Once β has been determined, the probability that any future observation x^* belongs to the class labeled 1 can be computed as

$$\mathbb{P}(y^* = 1|\mathbf{x}^*) = \frac{\exp\left((\mathbf{x}^*)^T\boldsymbol{\beta}\right)}{1+\exp((\mathbf{x}^*)^T\boldsymbol{\beta})} . \quad (3\text{-}4)$$

Based on the above, the decision rule for the classifier is given by

$$y^* = \begin{cases} 0, & \text{if} \quad \mathbb{P}(y^* = 1|\mathbf{x}^*) < \delta \\ 1, & \text{if} \quad \mathbb{P}(y^* = 1|\mathbf{x}^*) \geq \delta, \end{cases} \quad (3\text{-}5)$$

where δ is the discrimination threshold that determines the predicted class.

3.3.2 Feature Extraction

The developed approach uses both time-domain and frequency-domain features extracted from several features described below.

3.3.2.1 Time-Domain Features

Time domain features such as peak amplitude, rise time, etc. [25, 26] are commonly used to classify damage types for different materials. Features such as Kurtosis have also been found useful in structures such as metal pipes [32]. Features used for different materials may have the potential to be useful for the composite materials as well. The time domain features considered here include commonly used features in different structural analysis problems and others used by machine learning classifiers for different materials. Ten different features of the experimental AE signals in time domain were studied. Estimation of a number of these features is illustrated in Figure 3-9, and discussed below.

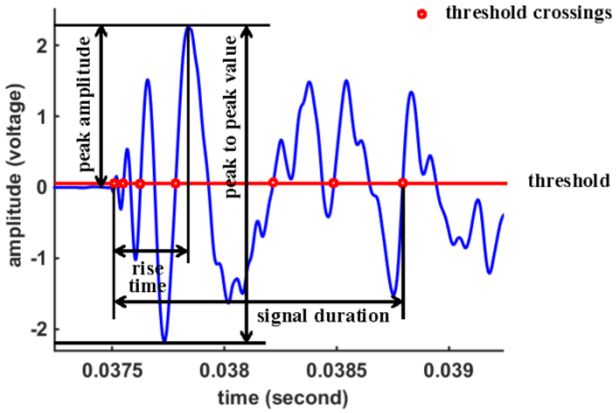

Figure 3-9. Time domain features of an experimental signal.
The amplitude threshold equals 0.4 voltages.

<u>Peak Amplitude</u>: Peak amplitude is the maximum amplitude of the signal [25, 26]. It represents the largest instantaneous strength of the sensor signal during the response time.

<u>Rise Time</u>: Rise time is the time elapsed from the first time the signal crossed a preselected threshold to the time of the peak amplitude [26]. That is, rise time measures how much time the signal takes to reach its maximum strength.

<u>RA Value</u>: The RA value is defined as the ratio between the rise time and the peak amplitude [26], i.e.,

$$\mathrm{RA} = \frac{\text{rise time}}{\text{peak amplitude}} . \tag{3-6}$$

<u>Signal Duration</u>: The signal duration is the time elapsed from the first time the signal crossed a preselected threshold in the positive direction to the last time the signal crossed the threshold in the positive direction [25, 26].

<u>Average Frequency</u>: Define the crossings of the signal and the preselected threshold in the positive direction as the number of threshold crossings. The average frequency is defined as [26]

$$\text{Average Frequency} = \frac{\text{number of threshold crossings}}{\text{signal duration}} . \tag{3-7}$$

This feature provides information about how frequently the signal strength reaches a threshold level and it is related to the frequency contents of the signal.

<u>Signal Energy</u>: Signal energy is a commonly used feature [25, 32]. The signal energy and l_2 norm signal energy are defined as

$$E_{\mathbf{s}} = \sum_{i=0}^{L-1} s_i^2 \tag{3-8}$$

and

$$\| \mathbf{s} \|_2 = \sqrt{\sum_{i=0}^{L-1} s_i^2} \ . \tag{3-9}$$

Peak to Peak Value: Peak to peak value is defined as the difference between the maximum amplitude and the minimum amplitude of the signal [31]. It is the range that the signal amplitude varies.

Curve Length: Curve length was a very useful feature in [31, 32] for damage classification on a metal pipe. Curve length describes the shape changes in the signal. It is calculated as

$$\text{curve length} = \sum_{i=1}^{L-1} | s_i - s_{i-1}. \tag{3-10}$$

Kurtosis: Kurtosis is an important concept in statistics to describe the distributional shapes [42]. Kurtosis interprets the value of the standardized fourth central moment and it is defined as

$$\text{Kurtosis} = \frac{\frac{1}{L}\sum_{i=0}^{L-1}(s_i - \bar{s}_i)^4}{[\frac{1}{L}\sum_{i=0}^{L-1}(s_i - \bar{s}_i)^2]^2} \ . \tag{3-11}$$

3.3.2.2 Frequency-Domain Features

Figure 3-10 provides a summary of some published work on frequency ranges corresponding to different types of damage [25, 28, 29]. The frequency components of the AE signals associated with different types of damage has a wide range because of the differences in the materials involved. However, we can see that delamination and fiber breakage always occupy different frequency ranges for each material and the ranges are larger than 50 kHz generally. Therefore, our algorithm selected features based on thirty-nine sub-bands with frequency range as shown in Figure 3-11. These sub-bands had bandwidths of 50 kHz or 100 kHz, and covered the whole frequency band (0-1MHz). Features that represent the distribution or signal energy corresponding to each frequency band are extracted used in the classifier.

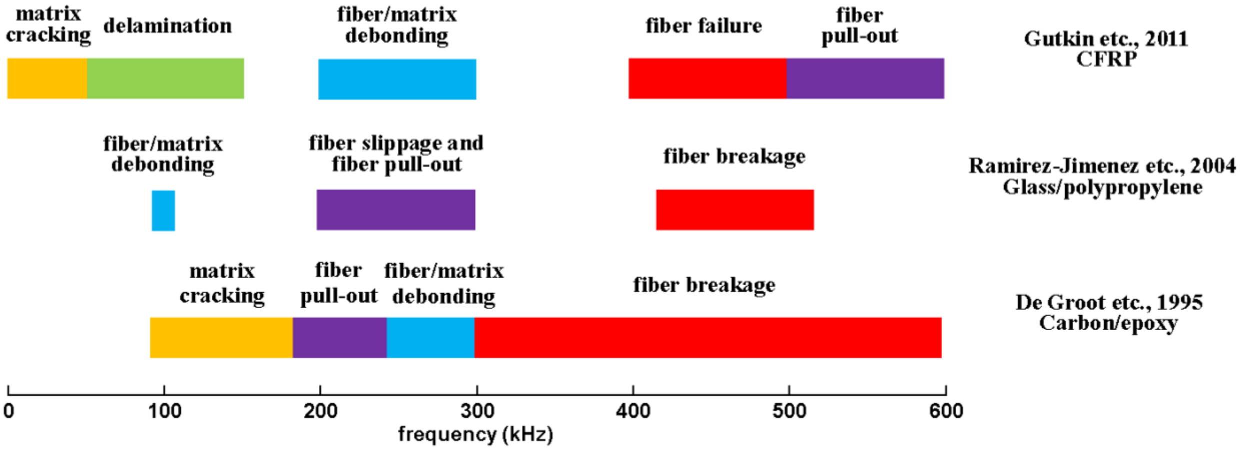

Figure 3-10. Frequency ranges corresponding to different types of damage.

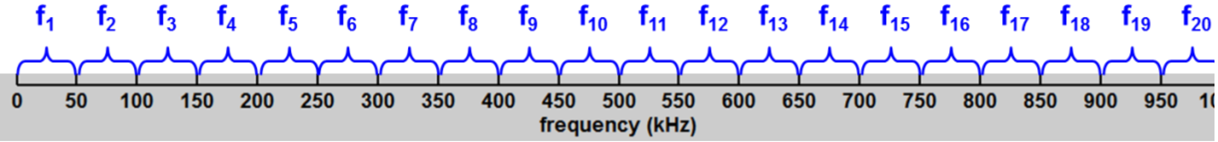

(a) Set I: 0 kHz to 1000 kHz, 50 kHz increment

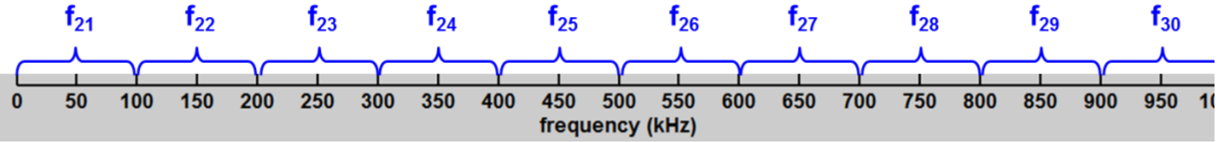

(b) Set II: 0 kHz to 1000 kHz, 100 kHz increment

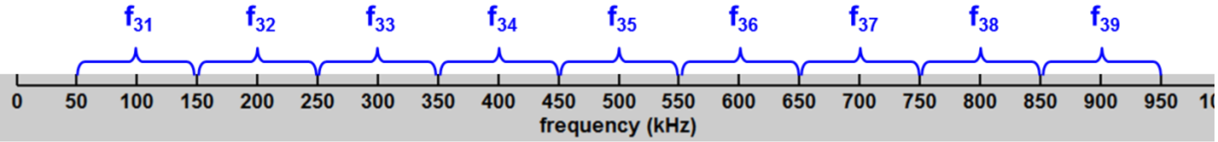

(c) Set III: 50 kHz to 950 kHz, 100 kHz increment

Figure 3-11. Frequency bands used to extract features for the classifier.
There are 39 sub-bands in total.

The discrete Fourier transform (DFT) of the signals $\mathbf{y} = (y_0, \cdots, y_{N-1})$ is calculated as

$$S(k) = \frac{1}{N} \sum_{n=0}^{N-1} s_n \cdot e^{-\frac{i2\pi kn}{N}},\ k = 0, \cdots, N-1\ . \tag{3-12}$$

To assess the signal energy distribution in the frequency domain, we estimate the power spectral density (PSD) $\widehat{\phi_{ss}}(k)$ of the signal using the Welch method [43].

The following variables comprised the frequency-domain features used in the classifier:

Primary frequency: The primary frequency is the frequency at which the magnitude of DFT of the signals is the largest. This is a very popular parameter for damage classification [44]. In some situations, a certain number of the maximal peaks are considered, especially when the signals are wideband. Since our signals have wide-band characteristics, and different types of damage could occupy different frequency ranges, frequencies corresponding to the top five maximal magnitude peaks of DFT signals are used as features.

Sum of the magnitude of the DFT: This feature is computed for all 39 sub-bands.

Mean of the PSD: The mean value of the PSD is computed over all frequencies in each sub-band, resulting in 39 different features.

Variance of the PSD: This feature is computed for each of the 39 sub-bands.

Standard Deviation of the PSD: This feature is also computed for each sub-band.

There are 39 features for each of the last four categories. Altogether, a total of 171 different features were employed in the classifier, including the 10 time-domain features.

3.3.3 Feature Selection

Using the 171 features described above may result in overfitting the classifier model to the training data. This will result in a reduction of the classification accuracy outside the training set. In this work, we employ the LASSO algorithm to select a smaller number of features that can best perform the classification task [44].

In the LASSO method, β is determined by solving an optimization problem given as

$$\min_{\boldsymbol{\beta}}\ -\sum_{i=1}^{N} \log\left(\mathbb{P}(y_i|\mathbf{x}_i)\right) + \lambda \sum_{i=1}^{N} |\beta_i|\ , \tag{3-13}$$

where $\mathbb{P}(y_i|\mathbf{x}_i)$ is the conditional probability obtained in the logistic regression method. The variable λ is a tuning parameter solved by cross validation. Given the value of λ, the objective function in the above formulation is convex, and a unique global solution may be obtained by the cyclical coordinate descent method [45]. The nonzero values of the sparse solution β indicate the features which are selected.

3.4 Results of Damage Classification

3.4.1 Metrics for Performance Assessment

The accuracy and the area under the Receiver Operating Characteristics (ROC) curve (AUC) are used for classification evaluation. They are computed from a confusion matrix [46]. Taking the characterization of the undamaged type from the damaged type as an example, a confusion matrix is defined in Table 3-6. True positive (TP) and true negative (TN) values are the number of occurrences that correctly identify the damaged or undamaged type, respectively. False negative (FN) and false positive (FP) are the number of occurrences that wrongly classify damage types as undamaged or damaged, respectively.

Accuracy measures the percentage of the correct classifications and it is reported as

$$\text{accuracy} = \frac{\text{TP}+\text{TN}}{\text{TP}+\text{TN}+\text{FP}+\text{FN}}. \tag{3-14}$$

An ROC curve is a two-dimensional graph that depicts classifier performance [47]. It is generated by two variables: true positive rate (TPR) and false positive rate (FPR), which are defined by

$$\text{TPR} = \frac{\text{TP}}{\text{TP}+\text{FN}} \tag{3-15}$$

$$\text{FPR} = \frac{\text{FP}}{\text{FP}+\text{TN}}. \tag{3-16}$$

From the above definitions, we can see that TPR is the rate of correctly classifying damaged case and FPR is the rate of wrongly characterizing undamaged as damaged case. The ROC curve plots the FPR and TPR as x-axis and y-axis, respectively, when the discrimination threshold of a binary classifier varies [47]. The ROC curve depicts the relative trade-offs between FPR and TPR. For a perfect classifier, FPR and TPR would be 0 and 1, which denote the left upper corner of the ROC curve. Therefore, the closer the ROC curve is to the left upper corner, the better the performance of the classification. Moreover, the area under the ROC curve (AUC), which takes values in the interval $[0,1]$, is another metric for performance evaluation. Therefore the larger the AUC, the better the classifier.

Table 3.6. Confusion Matrix

		PREDICTION	
		Damaged	**Undamaged**
TRUTH	**Damaged**	True positive (TP)	False negative (FN)
	Undamaged	False positive (FP)	True negative (TN)

3.4.2 Identifying Damage Producing Impacts

There were 86 drop weight experiments in total generating different types of damage on the composite panels. There were 16 impacts that did not result in damage on the composite panels and 70 impacts that caused damage. Eighty percent of the impact data corresponding to undamaged cases and damaged cases were used for training. Testing was performed on the remainder of impact data. The reduced set of features selected by the LASSO algorithm is listed in Table 3-7. We evaluated the classifier using all 171 features and the reduced set of 8 features. The classifier was designed and tested 1000 times using five-fold cross validation on a different (randomly selected from our data set) training and testing set each time.

The classification accuracies using all features or selected features are shown in Figure 3-12. We can see that when all features were used, most of the realizations had 100% classification accuracy. Twenty-four out of the 1000 runs characterized damage with about 99% accuracy. Using feature selection, the results achieved 100% accuracy in every run. The average ROC curve was obtained by merging all the predictions in each run to one large set and then applying the mechanism of ROC curve generation on this large prediction set [47]. Figure 3-13 displays the average ROC curves for the two cases. The AUC value of using all features was approximately 1, and for selected features the AUC equaled 1.0 as shown in Figure 3-13.

Table 3-7. Selected Features for Identifying Impacts that Induce Damage

Index	Feature
1	Signal duration
2	Summation of magnitude of DFT in 200 kHz ~ 250 kHz
3	Summation of magnitude of DFT in 200 kHz ~ 300 kHz
4	The 1st primary frequency
5	Mean of PSD in 0 kHz ~ 50 kHz
6	Mean of PSD in 350 kHz ~ 400 kHz
7	Standard deviation of PSD in 50 kHz ~ 100 kHz
8	Standard deviation of PSD in 250 kHz ~ 350 kHz

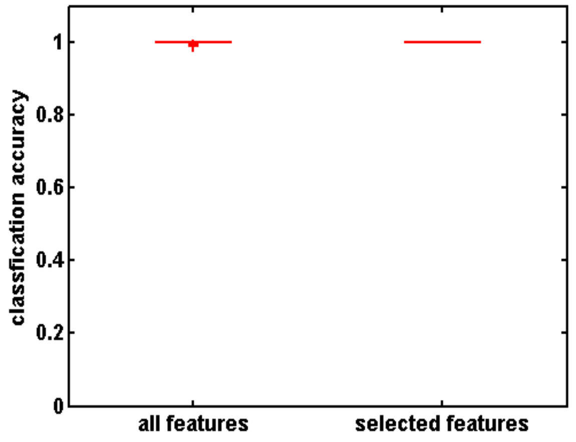

Figure 3-12. Box plots of classification accuracy of undamaged type and damaged type over 1000 runs.

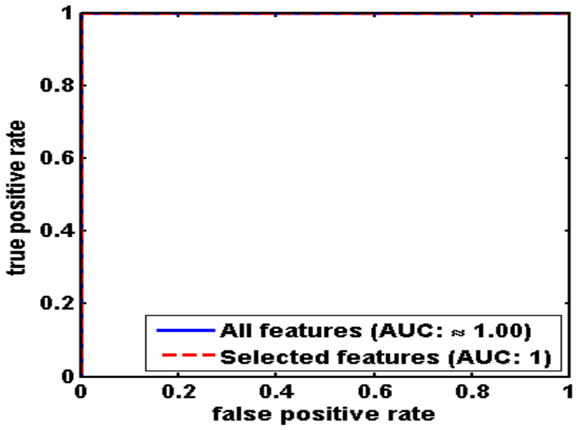

Figure 3-13. Average ROC curves of undamaged type and damaged type over 1000 runs.

3.4.3 Identification of Damage Type

In this analysis, the data sets for impacts that resulted in damage were considered. There were 70 impacts in total that caused damage in the composite panels: 21impacts of delamination with no fiber breakage and 49 impacts of mixture of delamination and fiber breakage. The classifier was used to characterize the delamination only and the mixture of delamination and fiber breakage. Similar to the analysis for classification between undamaged and damaged cases, eighty percent of the impacts corresponding to each type of damage were used for training. A total of 1000 runs each implementing a five-fold cross validation and using different training and testing sets each time, with and without feature selections were implemented.

The reduced feature set, as determined by the LASSO algorithm contained 19 features, and are shown in Table 3-8. The results of classification accuracy are shown in Figure 3-14. The accuracy was approximately 67% when all features were utilized. Applying the reduced feature set resulted in an improved classification accuracy of 74%. Although this is better than chance and demonstrate the feasibility of the method to determine damage types from acoustic emission signals, additional work is needed to obtain more reliable determination of the damage type. The average ROC curves and AUC values for the classification of damage types are given in Figure 3-15. The AUC increased from 0.69 to 0.80 after using feature selection.

Table 3-8. Selected Features for Classification Between Delamination with No Fiber Breakage and Mixture of Delamination and Fiber Breakage

Index	Feature	Index	Feature
1	Maximum amplitude	11	Mean of PSD in 650 kHz ~ 700 kHz
2	Rise time	12	Variance of PSD in 850 kHz ~ 900 kHz
3	Average frequency	13	Standard deviation of PSD in 50 kHz ~ 100 kHz
4	Curve length	14	Standard deviation of PSD in 350 kHz ~ 400 kHz
5	Kurtosis	15	Standard deviation of PSD in 750 kHz ~ 800 kHz
6	Summation of the magnitude of DFT in 350 kHz ~ 400 kHz	16	Mean of PSD in 600 kHz ~ 700 kHz
7	The 4th primary frequency	17	Variance of PSD in 0 kHz ~ 100 kHz
8	The 5th primary frequency	18	Standard deviation of PSD in 250 kHz ~ 350 kHz
9	Mean of PSD in 0 kHz ~ 50 kHz	19	Standard deviation of PSD in 350 kHz ~ 450 kHz
10	Mean of PSD in 100 kHz ~ 150 kHz		

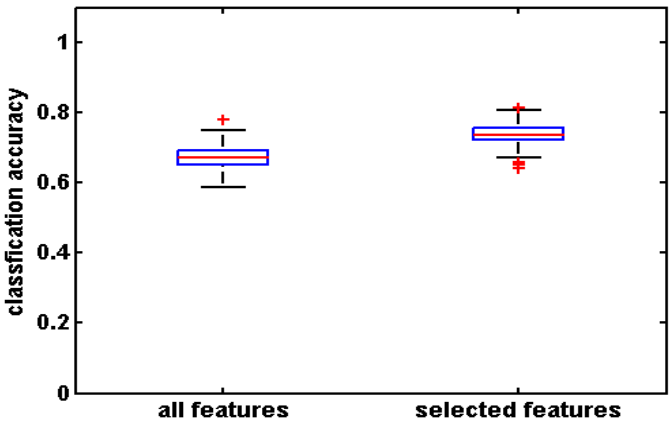

Figure 3-14. Accuracy of classification of delamination with no fiber breakage and mixture of delamination and fiber breakage over 1000 runs.

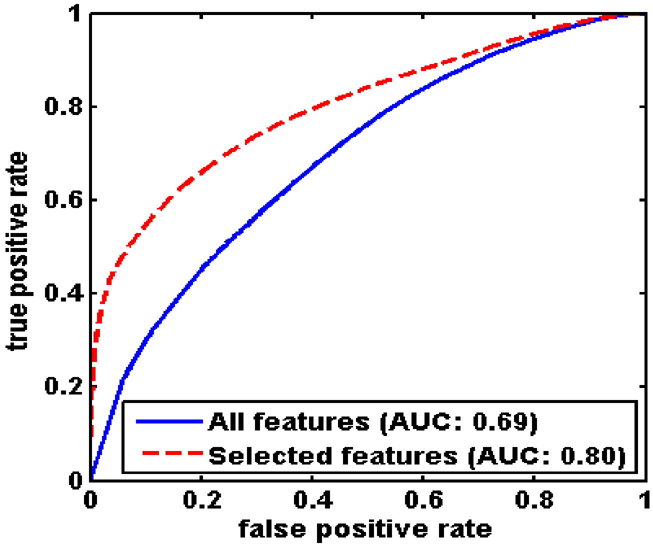

Figure 3-15. ROC curves for classification between delamination with no fiber breakage and mixture of delamination and fiber breakage.

3.4.4 Effect of Fiber Breakage Severity on Damage Type Classification

Figures 3-16 and 3-17 display the classification accuracy and AUC for analyzing classifiers of matrix damage Vs a mixture of matrix damage and fiber damage with fiber breakage length larger than a threshold μ. Here, we attempt to determine if the classification accuracy will become better as the severity of fiber damage increases. The results of a similar analysis where the severity of fiber breakage is characterized in terms of the ply depth κ of the fiber breakage are shown in Figures 3-18 and 3-19. As expected, both sets of analysis clearly indicate that our method performs better as the severity of damage increases. Even then, it is important to seek enhancements to the algorithm that would increase the robustness of the classifier accuracy to smaller levels of damage.

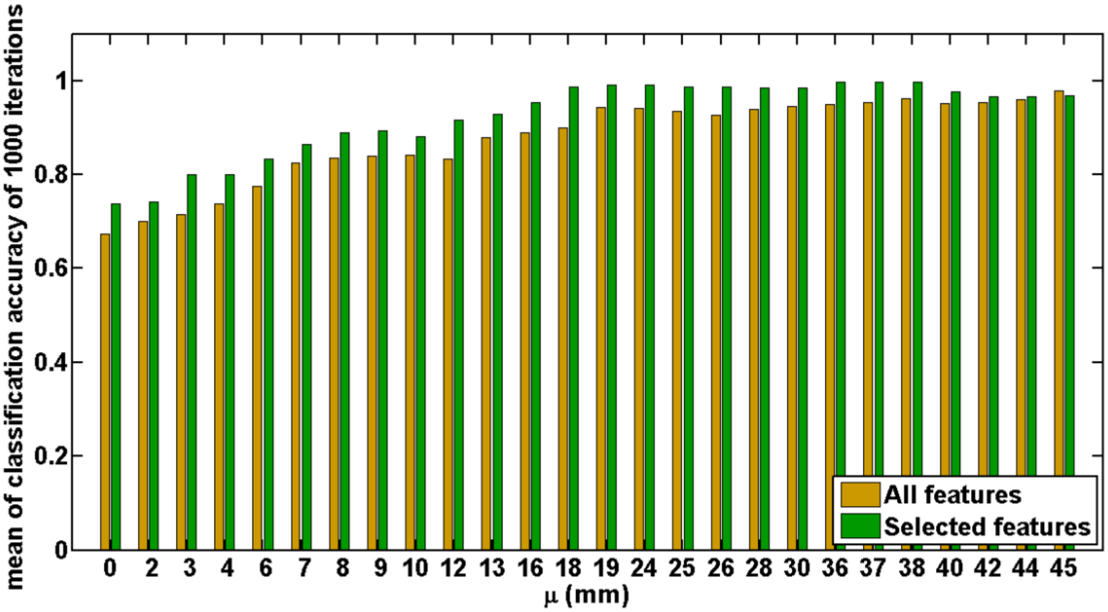

Figure 3-16. Mean of the classification accuracy for matrix damage and mixture of matrix and fiber damage with fiber breakage length larger than μ.

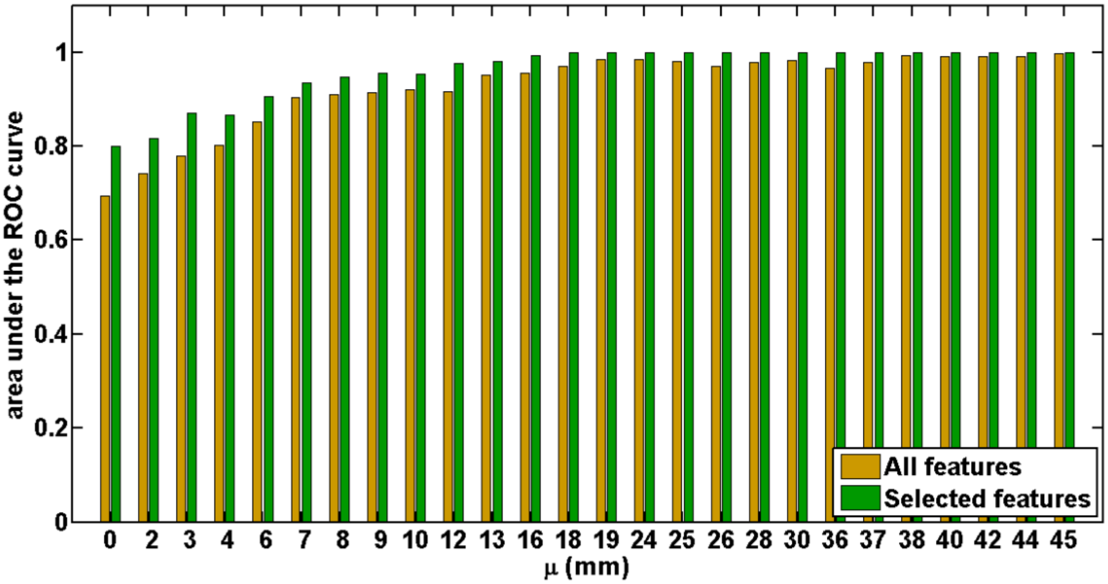

Figure 3-17. AUC of the classifiers for matrix damage vs. mixture of matrix and fiber damage with fiber breakage length larger than μ.

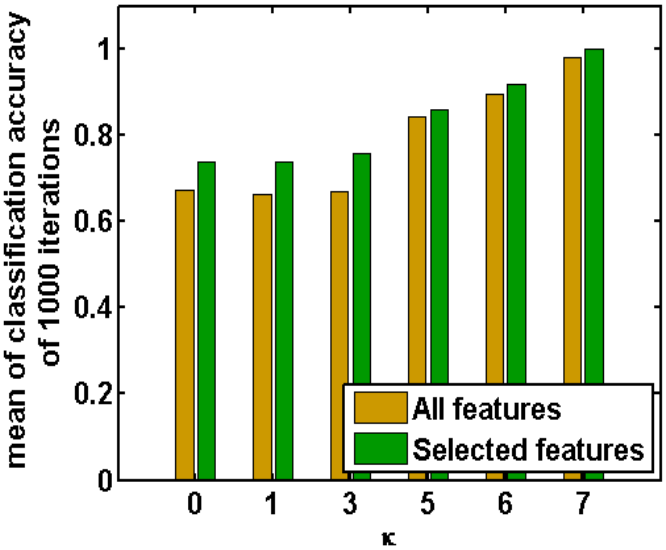

Figure 3-18. Mean of the classification accuracy for matrix damage and mixture of matrix and fiber damage with depth of fiber breakage at ply depth κ or more.

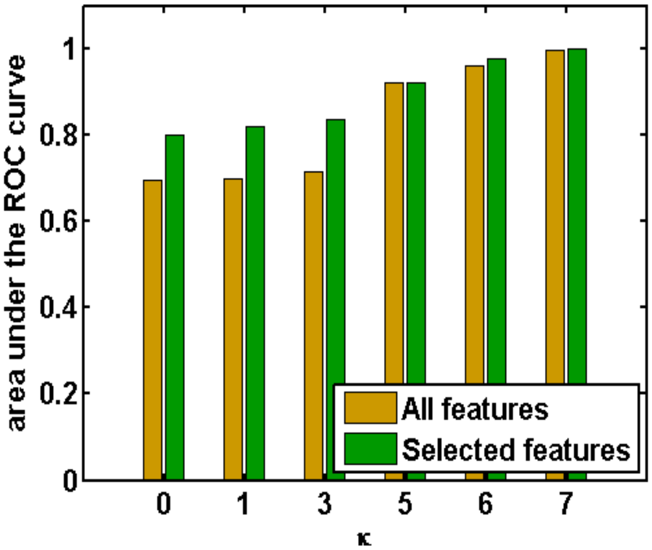

Figure 3-19. AUC of the classifiers for matrix damage vs. mixture of matrix and fiber damage with depth of fiber breakage at ply depth κ or more.

3.5 Summary and Conclusions

Damage assessment is required after damage detection for evaluation of the structure's residual strength. This is especially important when the damage in a composite structure is barely visible and not easy to detect using visual inspection methods. Therefore it is of interest to have the ability to classify the type of damage that is produced when a composite structure is impacted. In this work, drop-weight impact data acquired systematically on orthotropic carbon/epoxy composite panels was analyzed for damage classification. Two related objectives were investigated. The first involved the identification of impacts that produced damage. The second involved the determination of whether damage was limited to delaminations or was a mixture of delamination and fiber breakage. A total of 171 different acoustic emission features in the time and frequency domains were analyzed. The system employed logistic regression for classification and the LASSO algorithm for feature selection. For the undamaged versus damage case, the classification accuracy achieved 100% for every run and the area under the ROC curve equaled 1. For the delamination only versus a mixture of delamination and fiber breakage, the accuracy was 74% and the AUC was 0.80. These results indicate that the developed approach provides reliable performance in identifying impacts that result in damage. The computational complexity of this method is relatively low, and the method can be easily implemented for real-time operation. Identifying the type of damage is more challenging, and additional research is necessary to achieve the same level of performance possible for detecting damage from AE signals.

4. COMPARATIVE AE SENSOR EVALUATION

Acoustic Emission (AE) based Structural Health Monitoring (SHM) systems typically require the use of sensor networks that are affixed to the surface of the structure and allow real-time acquisition of AE signals from impact events. The characteristics of these received signals can be used to detect an impact event, estimate the impact location, and possibly determine the formation and type of damage produced from the impact. With a variety of available AE sensors exhibiting different characteristics and responses to varying impact events, comparative performance evaluations are useful for identifying their suitability for use in AE-based SHM systems. When a structure is excited upon external impact, the transmission of the AE signal from the structure to the bonded sensors and the characteristics of the received waveform are dependent on the sensor properties. Based on these response attributes, the sensor response information on wave mode Time Of Arrival (TOA) and velocity estimation can be used for impact location identification. Therefore, sensor selection is an important consideration in the development of a SHM system. Since a wide range of wave frequencies below 1 MHz are expected to be generated from a spectrum of possible impacts, a broadband sensor response is a primary interest. In addition to location estimation and damage classification, it is also imperative that the accuracy of the location estimation process be improved while decreasing the sensor footprint on the composite structure.

4.1 AE Sensors Investigated

Based on initial research, a variety of piezoelectric sensors offering a range of characteristics were identified. Upon further discussions with industry professionals and a preliminary evaluation, six different AE sensors were selected for initial evaluation based on their performance characteristics, operating frequency range, size and ease of use, signal quality and sensitivity to realistic damage events. As shown in Figure 4-1, both permanently mounted as well as moveable sensors were considered for the sensor characterization and feasibility assessment. Each sensor is shown in Figure 4-1 and described briefly below.

a. b. c. d. e. f.

Figure 4-1. AE sensors evaluated. a. Acellent Single Smart Layer. b. Vallen Systeme 900-RIC. c. Vallen Systeme 900-RIC. d. Digital Wave B-1025T. e. STEMiNC wire lead sensor. f. SteveCo KRNBB-PC.

Acellent Single Smart Layer Sensor

Acellent's Single Smart Layer sensors are a permanently mounted and compact sensor type that uses a piezoelectric ceramic element. The overall sensor dimensions are 40 mm x 10 mm, and feature a 6 mm diameter sensor element. A polyamide high dielectric film is used to protect the element from the environment as well as noise interferences. The sensor has a weight of 1 gram and reported frequency range of 1 Hz- 5 kHz [48].

Vallen Systeme 900- RIC Sensor

Vallen Systeme's 900-RIC sensors are moveable sensors that consists of an integral 34 dB gain pre-amplifier and calibration bypass. The dimensions of the sensor stainless steel casing are 29 mm in diameter x 32 mm tall, and the enclosed piezoelectric ceramic sensor element is 12.5 mm in diameter. The sensor has a reported frequency response of 100 – 900 kHz and weighs 67 grams [49].

Vallen Systeme 900- M Sensor

Vallen Systeme's 900-M sensors are also moveable sensors with a reported frequency response of 100 – 900 kHz. The dimensions of the sensor casing are 20 mm in diameter x 14 mm in height, have an enclosed 12.5 mm diameter sensor element and weigh 21 grams. In contrast to the 900-RIC sensor, these sensors require the use of an external preamplifier with a 34 dB gain and a 28 VDC power supply [49].

Digital Wave B-1025T Sensor

Digital Wave's B1025-T sensors are another type of moveable sensor with a reported frequency response of 1 kHz – 1.5 MHz. The 9 mm diameter x 14 mm tall casing encloses a 6.3 mm diameter piezoelectric ceramic sensor element with a total weight of 8 grams. These sensors also require the use of an external preamplifier with a 20 dB gain [50].

STEMiNC Wire Lead Sensor

Steiner & Martin, Inc's Wire Lead Sensor has a piezoelectric ceramic plate that uses a SM412 piezo material. These sensors are permanently mounted and have a resonant frequency of 240 ±5 kHz. The dimensions of the sensor are 7 mm x 8 mm x 0.2 mm and weigh less than a gram [51].

SteveCo KRNBB-PC Point Contact Sensor

SteveCo's KRNBB-PC Point Contact sensors are moveable sensors with a reported frequency response of 20 kHz – 1 MHz. The dimensions of the sensor casing are 14 mm in diameter and 28 mm in height and weighs 17 grams. The sensor encloses a nickel faceplate within a stainless steel body. These sensors require the use of a KRNWB-PC single or KRN AMP-xBB-J multi-channel preamplifier [52].

4.2 Sensor Assessment and Characterization

The six piezoelectric sensors investigated were characterized based on the received signal quality and their TOA response to both active and passive testing. These test types were performed using both aluminum and carbon/epoxy composite plates. The arrival time of the initial symmetric extension (S_o) and asymmetric flexural (A_o) plate wave modes were estimated and used to calculate the mode velocities, based on the signals received by the different AE sensors under investigation.

Additionally, the signal quality and strength, as characterized by the waveform dispersion and Signal-to-Noise Ratio (SNR) was investigated and compared for the six sensor types. The frequency response of each sensor was evaluated for the two types of tests to assess sensor sensitivity. Finally, the experimental results were compared with predictions obtained using both the Disperse code and finite element analysis software, ANSYS. Disperse is commercially available software used to generate dispersion curves for multi-layered structures [53] whereas ANSYS is a commercially available multi-physics finite element code [54].

4.2.1 Active and Passive Testing

Two types of tests were performed to investigate the characteristics of the six piezoelectric AE sensors: active testing and passive testing. For active testing, an AE transducer is used to produce an input signal to excite the structure. The piezoelectric sensors under investigation are used as receiving sensors to record a signal response. In the case of SHM applications, active testing would focus on changes in received sensor signals from neighboring "sending" sensors to indicate the presence of damage produced in the structure [55]. For passive testing, an external impact event, ranging from a pencil lead break or steel-ball drop to an actual low-velocity impact experiment is used to provide the input signal and the AE sensors under investigation record a signal response [56].

4.2.2 Wave Modes and Time of Arrival Estimation

For thin plates, two primary modes of Lamb wave propagation are produced from both passive and active excitation: extensional, or Symmetric (S) modes and flexural or Asymmetric (A) modes. While each wave mode consists of in-plane and out-of-plane displacement components, the extensional (S) mode consists primarily of in-plane displacements versus out-of-plane displacements for the flexural (A) mode. Whereas the extensional mode is characterized by high-frequency components, high velocity and low to minimal dispersive nature, the flexural mode exhibits lower frequency components, lower velocity and is highly dispersive. Furthermore, A modes can travel longer distances than the S modes, making them better suited for impact location estimation in large composite structures. However the wave propagation dispersion makes the process difficult [56]. For impact location estimation algorithms that utilize the initial time of arrival of a received signal, only the initial S_o and A_o modes are of interest. As a result the S_o and A_o modes are the primary focus in this study.

Based on the waveform signal recorded by the candidate sensors, the time of arrival measurements for the S_o and A_o modes are recorded for each sensor type. At different locations from the impact position, d_1 and d_2, the time difference of arrival of the wave modes, $t_2 - t_1$, is used to estimate the S_o and A_o wave mode velocities in both aluminum and carbon/epoxy composite plates using the expression

$$velocity = \frac{d_2 - d_1}{t_2 - t_1}. \tag{4-1}$$

For a particular sensor type, Figure 4-2 shows the waveform response recorded at two receiving locations namely Signal A and Signal B. Red dotted lines *d1* and *d2* denote the initial time of arrival of S_o modes at these two receiving locations. The time of arrival estimates at these locations is then used to estimate the S_o mode wave velocity. The process is then repeated for the A_o wave modes.

4.2.3 Waveform Dispersion

While the extensional and flexural wave modes are the most prominent in thin plates, the number of these waves depends on the *d/l* ratio, where *d* is the thickness of the plate and *l* is the acoustic wave length. For a particular acoustic frequency, there exists a number of wave propagation modes produced in the plate with a specific wave number or a phase velocity. The presence of these multiple wave modes as well the dispersive nature of the wave mode propagation are dictated by the dispersion curves [56].

Figure 4-3 shows the dispersion curve for an aluminum plate with a thickness of 1.6 mm as estimated from the Disperse software. Note that only the initial S_o and A_o modes are observed for frequency ranges lower than 1 MHz. While S_o wave mode depicts a general flat response of phase velocity over a range, A_o mode shows an ascending curve therefore causing phase velocity dispersion. Above 1 MHz, higher order Lamb waves, S_1 and A_1, are also observed and make mode separation difficult. For this sensor assessment, lower frequencies below 1 MHz are used for both active and passive testing. Hence, only S_o and A_o wave modes are expected for both active and passive testing to eliminate any possible convolution of higher frequency modes.

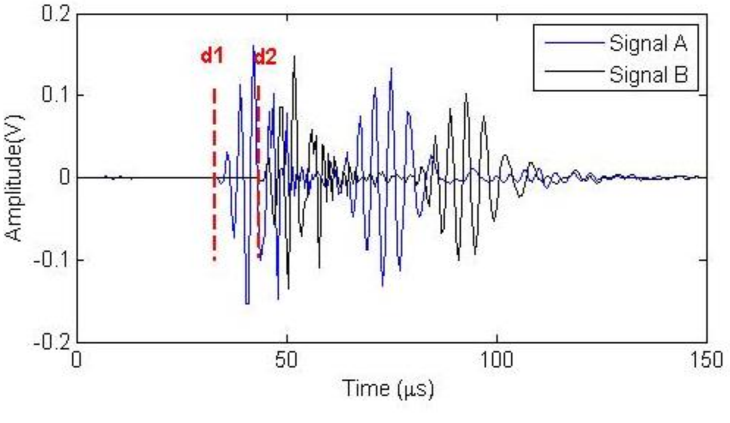

Figure 4-2. Time of arrival estimation.

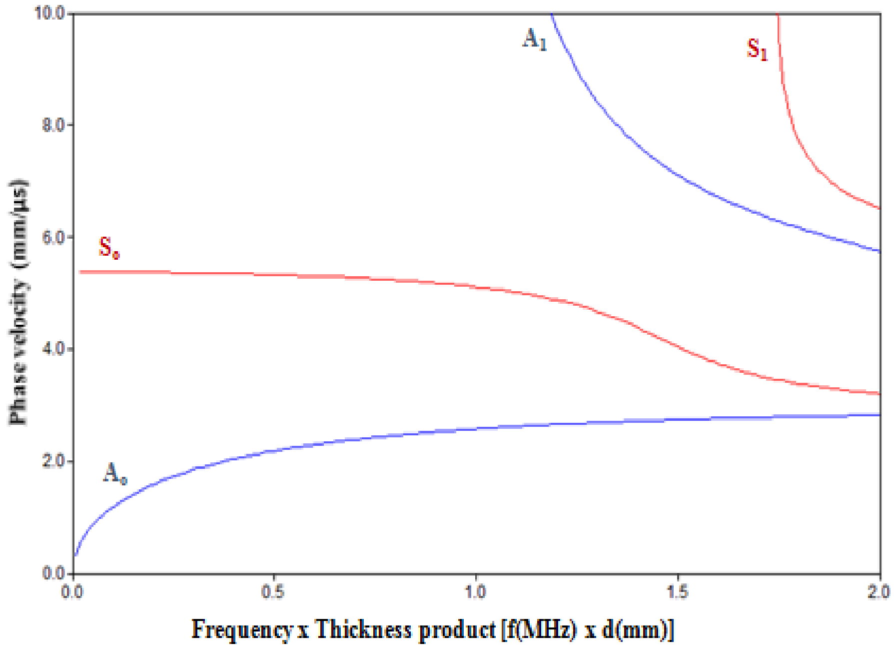

Figure 4-3. Dispersion curve of aluminum plate.

4.2.4 Signal-to-Noise Ratio

In signal processing, a Signal-to-Noise Ratio (SNR) quantifies the noise power corrupting the received signal power. A ratio higher than 1:1 means higher signal power than noise power and is desired for all sensor types. For an ideal signal with no noise and a zero-mean, the SNR is the ratio of squares of the signal variance to the noise variance [57], or

$$SNR = \frac{\sigma_{signal}^2}{\sigma_{noise}^2}. \tag{4-2}$$

For actual sensor signals, the signal power includes some level of noise. For a sufficiently large sample size, the noise can be considered non-zero and statistically independent of the signal [58]. In addition, the mean noise should be removed from the received signal to avoid the DC bias. The Signal-to-Noise Ratio in such case, can be written as

$$SNR = \frac{\sigma_{signal}^2}{\sigma_{noise}^2} - 1. \tag{4-3}$$

The SNR in the decibel scale can then be written as

$$SNR_{dB} = 20log_{10}(SNR). \tag{4-4}$$

4.3 Experimental Setup

Sensor evaluations were performed using two 1.2 m square test panels. The first panel, a 1.6 mm thick 6061-T6 aluminum plate was used for active and steel ball drop testing. Aluminum is isotropic in nature and has stiffness properties that are approximately constant in all directions, therefore making preliminary comparison easier for sensor evaluation. The second panel was a 16-ply (2.3 mm) thick quasi-isotropic $[0_2/45_2/90_2/-45_2]_s$ composite plate that was fabricated from Hexcel IM7/8551 carbon/epoxy unidirectional prepreg.

A National Instruments (NI) PXIe-1073 data acquisition system coupled with NI LABVIEW and MATLAB scripts were used for data collection and signal processing. For the Acellent single smart layer, Vallen Systeme 900-M, Digital Wave B1025T, KRNBB-PC and STEMiNC Wire Lead sensors were used with an AMP-4BB-J external preamplifier with 27 dB gain and internal 28 VDC power supply to boost the output signal strength. The Vallen Systeme's 900-RIC sensor required a decoupling circuit to remove the AC component from the signal prior to data acquisition.

To reduce impedance mismatch between the test panel and the sensor for better signal transmission, Vishay M-Bond 200 adhesive and Sonotech's High Z-HV couplant were used for the permanently mounted and moveable sensors, respectively. For proper mounting and consistency purposes, polyethylene templates were used for sensor placement at the desired locations. These templates were drilled and threaded at specific locations to custom fit each moveable sensor type to ensure proper bonding onto the test panel and prevent sensor movement.

4.3.1 Frequency Response Evaluation

A frequency response evaluation was performed for all six sensor types to determine their working frequency range on both aluminum and composite test panels. Since a wide range of AE monitoring is performed at frequency levels below 1 MHz, an input frequency range of 50 to 500 kHz with 50 kHz increments was used. The Acellent Single Smart Layer was used as a transducer for all active testing experiments owing to its broadband frequency range, low profile and permanent bondage to the test panel. Therefore the input signal and phase change was assumed constant for all sensors. A 5-cycle sinusoidal input signal was applied to the center of the test panel and the receiving sensor was placed 178 mm from the transducer. At each frequency, active testing was performed 10 times for each sensor type and the received signals were averaged to compute the sensor response for S_o and A_o plate wave modes.

For preliminary analysis of velocity estimation, the Disperse code was used to approximate particular wave modes' phase velocities at different frequencies. Figure 4-4 shows the dispersion curve of S_o and A_o wave mode velocities at different input frequencies for an aluminum plate. These estimates were used to separate the plate wave modes for further verification with sensor response analysis.

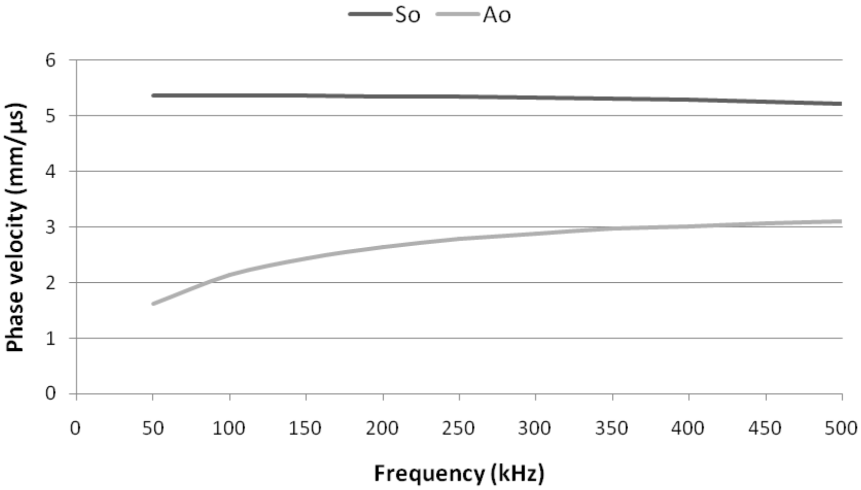

Figure 4-4. Dispersion curve of aluminum plate using 50 – 500 kHz input frequencies.

4.3.2 Sensor Response Estimation

The output response of a Linear Time-Invariant (LTI) system, *Y(f)*, can be characterized in the frequency domain using the convolution theorem such that

$$Y(f) = X(f) \cdot H(f), \tag{4-5}$$

where *X(f)* is the input signal (impulse) and *H(f)* is the system response to an impulse [58]. The system response consists of multiple components including instrumentation, coupling, structural and sensor properties. Assuming the system response is only affected by the plate response $H_p(f)$, *H(f)* may be written as

$$H(f) = H_p(f) \cdot H_a(f) \cdot H_r(f), \tag{4-6}$$

where $H_a(f)$ is the actuator response and $H_r(f,)$ is the receiving sensor response.

For a particular wave number *k(f)* and an actuating distance *r*, the ratio of the input frequency *f* and the phase velocity V_{ph} is different for both S_o and A_o mode waveforms. Therefore, the magnitude of the plate response $H_p(f)$ can be estimated using the Fast Fourier Transform (FFT) of the input and received signal response as [59]

$$\left|H_p(f)\right| = \frac{|Y(f)|}{|X(f)|\sum_m \sqrt{\frac{1}{k(f)r}}} = \frac{|Y(f)|}{|X(f)|\sum_m \sqrt{\frac{V_{ph}}{rf}}} = \left|\frac{Y(f)}{X(f)}\right| \sqrt{\frac{rf}{V_{ph}}}. \tag{4-7}$$

Furthermore, for a single actuator type, the input signal response was estimated and separated along with the plate response from the output signal response of the plate wave modes S_o and A_o therefore estimating the receiving sensor frequency response. An approximated time interval was chosen for both S_o and A_o mode propagation based on Disperse velocity simulation.

Figures 4-5 (a) and (b) show the frequency response analysis of S_o and A_o modes, respectively, for each sensor type. Vallen Systeme's 900-RIC showed the strongest overall signal response for S_o while KRNBB-PC showed a stronger response for the A_o wave mode, particularly at the midrange of frequencies investigated. It is to be noted that these results are used to understand the strength of the received waveforms at particular input frequencies and are valid for the said setup only. Some discrepancies between the S_o and A_o mode frequency responses were observed as a result of wave mode propagations and approximated time intervals using the predicted values of Disperse simulations. Nevertheless, based on the signal strengths at the approximated sensor bandwidth, 300 kHz was chosen as the best-suited input frequency for all six AE sensor types. Thus this frequency was selected for active testing in further sensor evaluations.

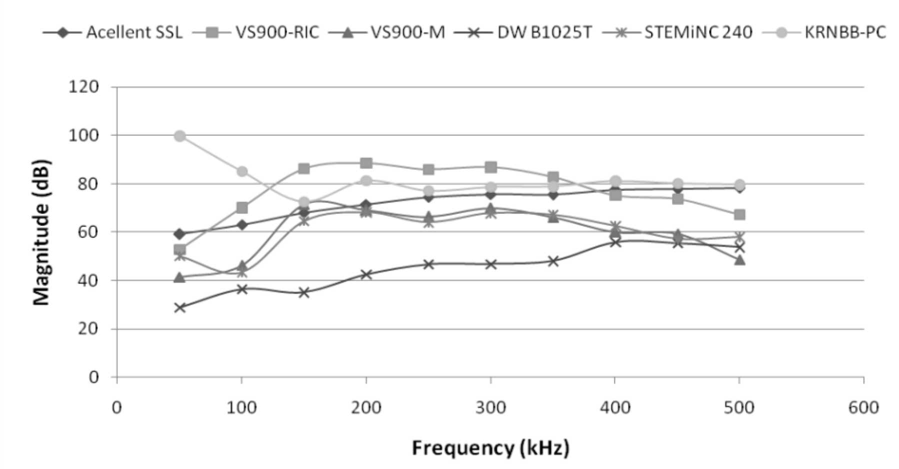

a. S_o wave mode.

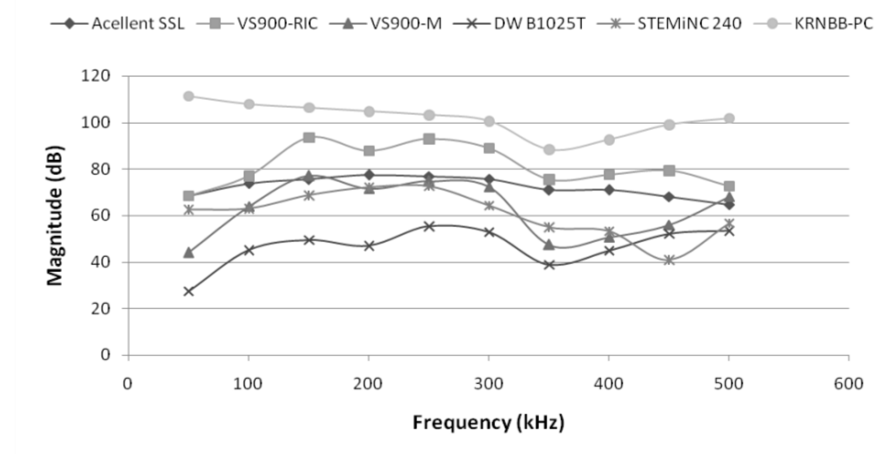

b. A_o wave mode.

Figure 4-5. Frequency response analysis of all sensor types.

4.3.3 Active and Passive Testing

For active testing, the input signal shown in Figure 4-6a was introduced at the center of the test panel. The response signal was recorded by two receiving sensors from each sensor type that were placed at two different distances from the input signal (Figure 4-6b): 178 mm and 228 mm. These distances were selected to effectively separate the S_o and A_o wave modes at the sensor locations and to avoid reflections from the edges of the 1.2 m square plate. As chosen from the frequency response analysis, a 5-cycle input signal was applied at a 300 kHz excitation frequency and a 2 MHz sampling frequency range to excite the structure. Testing was performed 20 times for each sensor type and the averaged data from each location were used for further signal analysis and TOA estimation.

For passive testing, a 12.7 mm diameter steel ball was dropped from a 152 mm height through a steering tube to a point at the center of the test panel. AE sensors were placed at the same two distances (178 mm and 228 mm) as used for active testing to record the impact response. The drop experiments were repeated 10 times for consistency of signal quality investigation.

4.4 Disperse Simulation

For this comparative evaluation study, dispersion curves for both aluminum and composite plates were calculated as per the material properties. Aluminum has a material density of 2.7 gm/cm^3 and the elastic properties are frequency and direction independent. For the composite plate, the plies are modeled using material properties in their local material coordinate system. The density of the IM7/8551 carbon/epoxy composite material used is 1.57 gm/cm^3 and each ply is 0.14 mm thick. Table 4-1 lists the elastic properties of the IM7/8551 composite material.

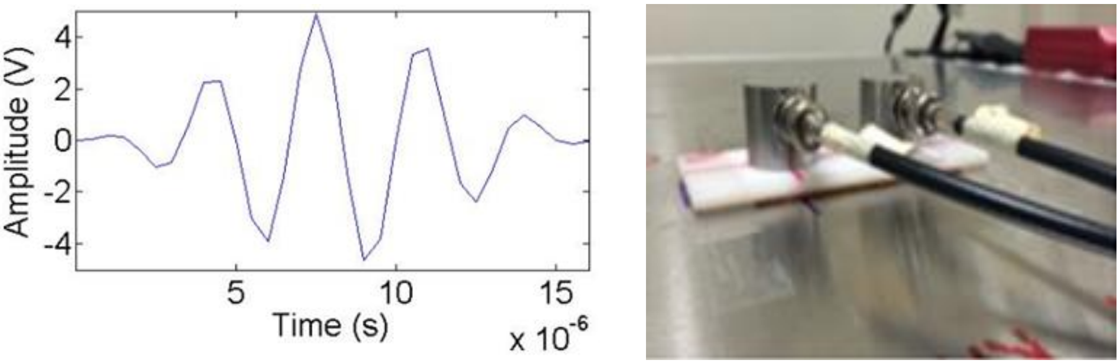

a. b.

Figure 4-6. a. Excitation signal for active testing. b. Two receiving sensors (VS 900-RIC).

Table 4-1. Elastic Properties of IM7/8551 Carbon/Epoxy

Material Property	**Value**
E_{11} (Pa)	1.66E+11
E_{22} (Pa)	8.56E+09
E_{33} (Pa)	8.56E+09
G_{12}(Pa)	5.60E+09
G_{13}(Pa)	5.60E+09
G_{23}(Pa)	2.94E+09
ν_{12}	2.69 E-01
ν_{13}	2.69 E-01
ν_{23}	4.56 E-01

4.5 Finite Element Analysis

To assist the evaluation of the recorded sensor responses during active testing, wave propagation of the 5-cycle tone burst input signal at 300 kHz frequency was simulated using finite element analysis. The commercial finite element code ANSYS was used to perform the three-dimensional dynamic analyses. Eight-node brick-type elements were used and displacement boundary conditions were applied to produce the input signal and the far-field support constraint as shown in Figure 4-7a. A representative three-dimensional "strip" of the test panels (400 mm in length x 5 mm in width x 2.3 mm in thickness) was used to reduce computational time. Response waveforms were recorded at the same two distances from the excitation input location used in testing: 178 mm and 228 mm. Two separate analyses with either in-plane or out-of-plane displacement signal inputs were used to investigate the S_o and A_o wave modes, respectively, as shown in Figure 4-7b. A 0.0625 μsec time step corresponding to a 16 MHz frequency response was used in the model and damping was not considered [27].

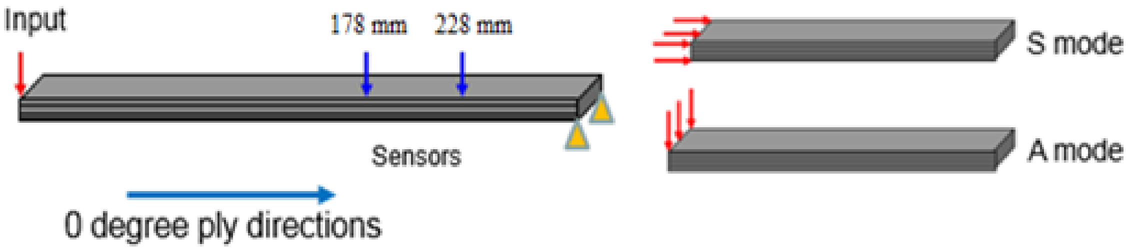

(a) (b)

Figure 4-7. Finite element modeling of test panel strip. a. Modeled region. b. Two input types (in-plane and out-of-plane) used for wave mode estimation.

4.6 Results

For active testing, averaged raw signals were used for sensor evaluation and TOA determination to avoid loss of any response data. The received output signals were compared with finite element simulation results for both TOA and velocity estimates. The finite element analyses did not incorporate a damping factor, and therefore did not produce the attenuation that exists in the actual test conditions. In this investigation, however, results from finite element simulations are used only for velocity comparison as well as S_o and A_o wave packet correlations.

4.6.1 Velocity Estimation Using Simulation

An input frequency of 300 kHz was used in the Disperse code and wave velocities for both symmetric (S_o) and asymmetric (A_o) modes were extracted from the dispersion curves. Similarly, finite element analyses were used to calculate the wave mode velocities using the time difference of arrival between two locations (178 mm and 228 mm). Figure 4-8 shows the S_o and A_o wave mode separation for active testing on an aluminum panel at a receiving location of 178 mm. Separation of these plate wave modes is significant for accurate time of arrival estimation.

Table 4-2 lists the predicted wave mode velocities for both the aluminum and composite plate using the Disperse code and ANSYS finite element analysis at an input frequency of 300 kHz. The simulated and theoretically predicted wave mode velocities using both analysis methods were found to be in agreement.

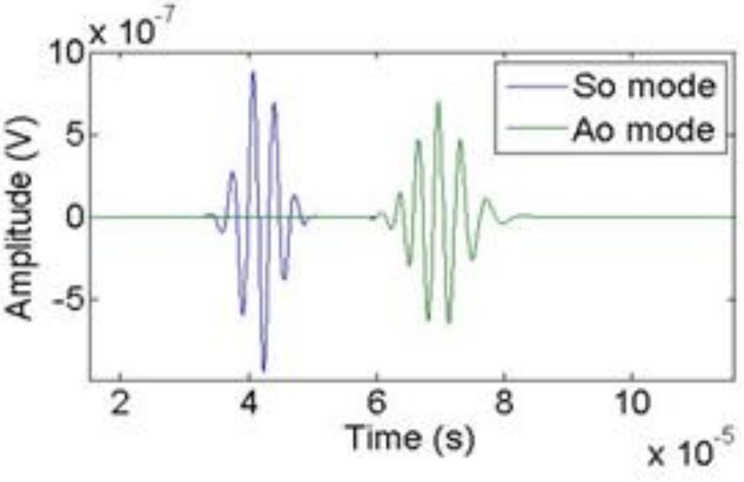

Figure 4-8. Results from finite element analysis of wave propagation in an aluminum plate for a 300 kHz input signal frequency.

Table 4-2. Predicted Wave Mode Velocities

Material Type	**Wave Mode**	**Predicted Wave Mode Velocity (mm/µs)**	
		Disperse	**ANSYS**
Aluminum	So	5.33	5.35
	Ao	2.89	2.92
Composite	So	5.63	5.83
	Ao	1.78	1.64

4.6.2 Waveform Evaluation and Velocity Estimation for Active Testing

For an input frequency of 300 kHz, both symmetric (S_o) and asymmetric (A_o) wave components were visible in the received signals from all six sensors types. For a 5-cycle input frequency, both S_o mode and A_o mode showed minimal to low dispersive nature of received wave packets for the aluminum test panel. As shown in Figure 4-9, a good signal amplitude response was observed for all sensor types. VS 900-RIC showed the largest S_o amplitude response (0.38 V) and DW B1025T showed the lowest at 0.006 V. The KRNBB-PC sensor showed the strongest response of the A_o wave packet at 2.8 V and the DW B1025T showed the lowest response of 0.006 V. Comparing the amplitude of the received S_o and A_o modes, the KRNBB-PC sensors showed the larger amplitude difference (0.28 V for S_o to 2.8 V for A_o) whereas the DW B1025T showed similar amplitudes for both wave modes. Additionally, random noise components between the wave packets were observed to be lower for the Acellent SSL, STEMiNC Wire Lead and KRNBB-PC sensors.

An excitation signal causes multiple wave modes, which propagate at different velocities. With increasing distance from the input signal, the total wave energy spreads, therefore causing dispersion [51]. A higher attenuation of the A_o wave packet and higher noise signal component was seen for all the sensor types for the composite plate. This result was believed to be due to the multiaxial laminated nature of the composite plate. As a result of multiple layers with different fiber orientations through the panel thickness, additional reflections from each layer interface are believed to occur in the composite panel. Additionally, random noise resulting from instrument setup, cable interference, and BNC cable connections add to these responses.

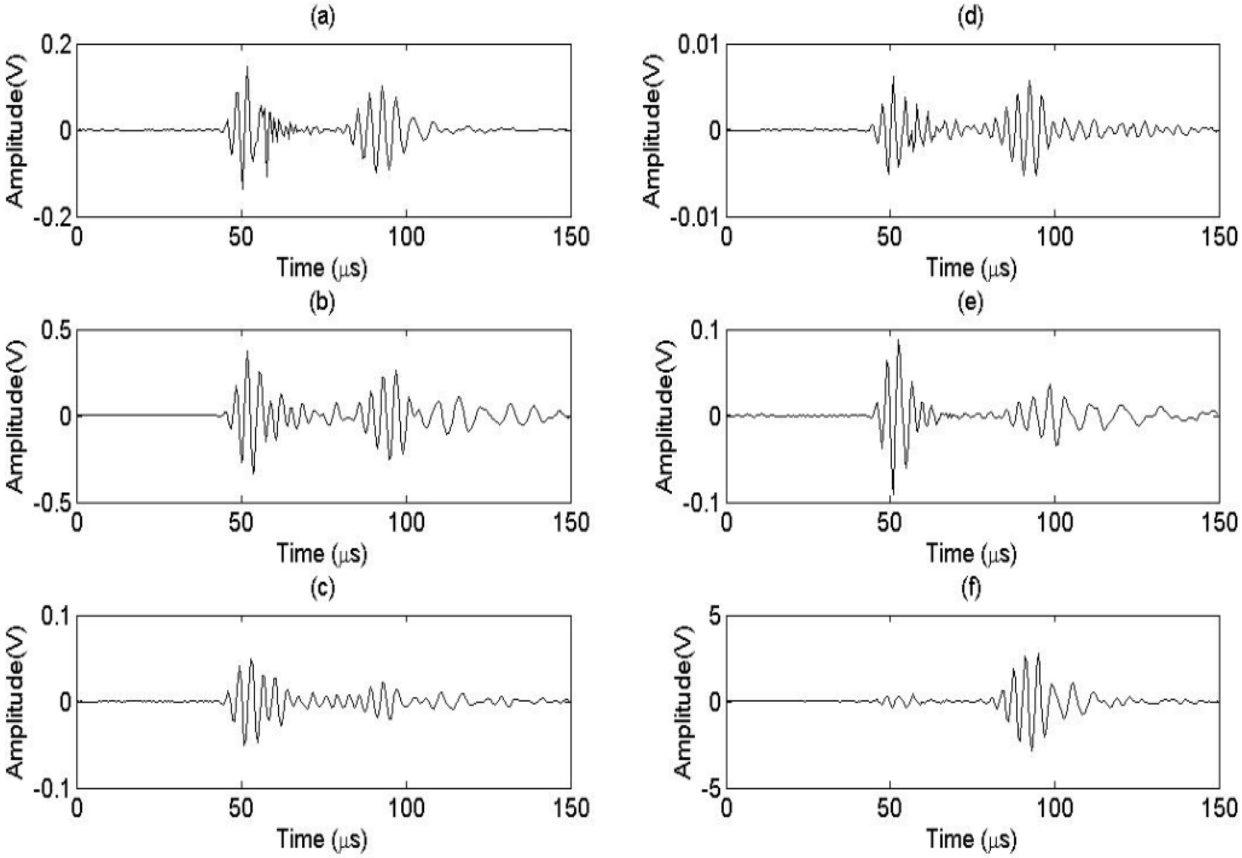

Figure 4-9. Active testing results from aluminum test panel. a. Acellent Single Smart Layer. b. Vallen Sensor 900-RIC. c. Vallen Sensor 900-M. d. Digital Wave B1025T. e. STEMiNC wire lead. f. SteveCo KRNBB-PC.

At a 300 kHz input frequency, both high-frequencies S_o and low-frequency A_o mode components were observed in all cases, but with some dispersive modes of lower amplitudes in between. This dispersive nature is believed to be a combined effect of the structural response in addition to instrument response, sensor type and the coupling mechanism. For a 5-cycle input signal, Acellent SSL sensor showed a good amplitude response owing to its permanent bondage to the structure, however, some additional wave components were observed in the S_o wave mode. The STEMiNC sensor showed comparable response to the Acellent SSL sensor, but with a slower A_o mode arrival time. The Vallen Systeme 900-M sensor also displayed significant noise components in comparison with the received wave modes. It is noted that the sensor element in the Vallen Systeme and Digital Wave moveable sensors is enclosed in a stainless-steel casing, which may reduce electromagnetic noise interference. However, additional “ringing” was observed with these sensors, which adds to the noise dispersion and makes initial arrival time estimation more difficult, especially for the A_o mode. The KRNBB-PC sensors showed a higher amplitude response for the A_o wave mode. In addition, lower received signal amplitudes were recorded in comparison to the ±5

Volt input excitation signal in active testing. This was believed to be due to the response signal from an impact point attenuating over a longer distance in the test specimen.

Based on the experimental signal responses, the time difference of arrival was estimated at five different locations on the response signal to account for the discrepancy caused due to dispersion. This assessment method was performed on all sensor types for consistency purposes. As a result, the initial time difference of arrival estimation for the S_o mode was slower than the average estimated time difference. Figure 4-10 shows the standard deviation error bar (1σ) for the time difference of arrival on the aluminum plate. The relative difference was found to be comparable for all sensor types. A similar observation was observed for the composite plate as well.

Based on the average time difference of arrival of all the sensor types, the So and Ao mode velocities were calculated. Table 4-3 shows the comparison between predicted wave mode velocities and those determined experimentally for both the carbon/epoxy composite and aluminum panels using the six AE sensors investigated. The measured wave velocities are in good agreement with the predictions from both the Disperse and ANSYS analyses. In conjunction with the dispersion curve of aluminum, the S_o arrival time was relatively independent of input frequency and minimal dispersion was observed. In contrast, the A_o mode exhibited wave property dependence particularly on input frequency. Preliminary study also suggested wave mode velocity dependence on material thickness. A better correlation with the Disperse and ANSYS results is found for the flexural A_o mode due to the approximated time intervals. While the permanently mounted Acellent single smart layer sensor showed good agreement with predictions for both wave mode components in aluminum, the moveable Digital Wave's B1025-T sensor showed better agreement for the composite plate.

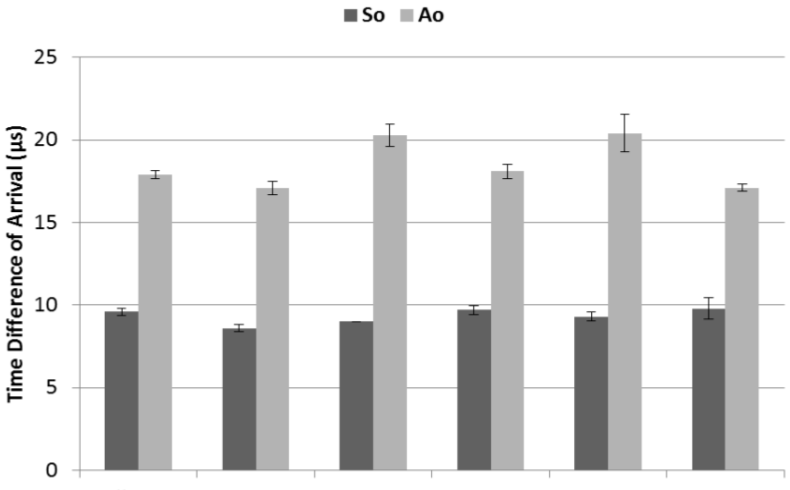

Figure 4-10. Time difference of arrival estimation from aluminum plate.

Table 4-3. Active Testing Wave Mode Velocity Predictions and Measurements

Material Type	Wave Mode	Predicted Wave Mode Velocity (mm/µs)		Measured Wave Mode Velocity (mm/µs)					
		Disperse	ANSYS	Acellent SSL	VS 900-RIC	VS 900-M	DW B1025T	STEM iNC	KRN BB-PC
Aluminum	**So**	**5.33**	**5.35**	**5.29**	**5.91**	**5.64**	**5.24**	**5.47**	**5.20**
	Ao	**2.89**	**2.92**	**2.84**	**2.97**	**2.50**	**2.81**	**2.50**	**2.97**
Composite	**So**	**5.63**	**5.83**	**5.41**	**5.41**	**5.04**	**5.78**	**6.20**	**5.29**
	Ao	**1.78**	**1.64**	**1.67**	**1.65**	**1.75**	**1.65**	**1.69**	**1.52**

4.6.3 Waveform Evaluation for Steel Ball Drop Testing

For steel- all drop testing, raw signals were used for wave mode detection and signal evaluation to avoid loss of imperative data. Such passive experiments are representative of low-velocity impacts that are of interest in real time SHM, where the impact type and source is unknown and signal filtering range is unpredictable. Experimental results showed that the steel ball drop testing produced both S_o and A_o wave modes, but the flexural A_o mode was predominant due to the stronger out-of-plane input condition as shown in Figure 4-11. The S_o wave mode amplitudes were comparable to those from the random noise signals making arrival time estimations difficult. While the nature of the signals remained similar, the Digital Wave B1025-T sensor exhibited a lower SNR of 9.58 dB and Acellent SSL showed the highest SNR of 39.62 dB.

As shown in Figure 4-11b, for the VS 900-RIC sensor that has an inbuilt preamplifier, the high-frequency S_o mode component was visible but of much lower amplitude and required higher magnification than the A_o wave mode. Similar to observations from active testing, the composite plate showed smaller wave packet amplitudes as compared to aluminum. For a passive testing condition such as a steel ball drop, the input signal produces multiple frequency responses with both high and low frequency components. As shown in Figure 4-11, the low-frequency A_o acoustic responses were dominant for all sensor types. The Acellent SSL, Vallen Systeme, Digital Wave and STEMiNC sensors showed a broadband wave packet response. The integrated preamplifier and calibration bypass used in Vallen Systeme's 900-RIC produced noise signal suppression and wave mode amplification within its effective operable range. The external preamplifier produced signal amplification for the other four sensors. However, signal filtering was not applied, and thus a broad spectrum response of both low frequency and high frequency components were observed in these cases. For the KRNBB-PC sensors, which are classified as *displacement* sensors, a significant signal response was recorded upon impact with greater amplitude than the subsequent acoustic responses. This initial response, believed to be the associated with the surface displacement upon impact, results from the sensor sensitivity to extremely low-frequency components. However, this additional response obtained during the steel ball drop impact testing produced a more complex overall sensor signal in comparison to the other sensors, which are primarily classified as *velocity* sensors and are less sensitive to surface displacements.

The SNR response of each sensor type with a 1σ error bar is calculated for all sensor types at both receiving locations of 178 mm and 228 mm. Figure 4-12 shows the SNR for steel ball drop testing using the composite plate. A similar response was observed for the aluminum plate. As expected, a considerable drop in the SNR is observed over an increased propagating distance. A comparable difference in SNR is observed for all sensor types between the two distances. The Acellent SSL, Vallen Systeme, STEMiNC and KRNBB-PC sensors exhibited higher SNRs and carried higher energy signals. The VS 900-M, DW B1025T and STEMiNC showed minimal error bar deviation in SNR estimation. Similar responses were observed in the case of the aluminum panel. A minimal SNR drop was observed for Acellent SSL, DW B1025T, STEMiNC and KRNBB-PC sensors for the isotropic aluminum panel.

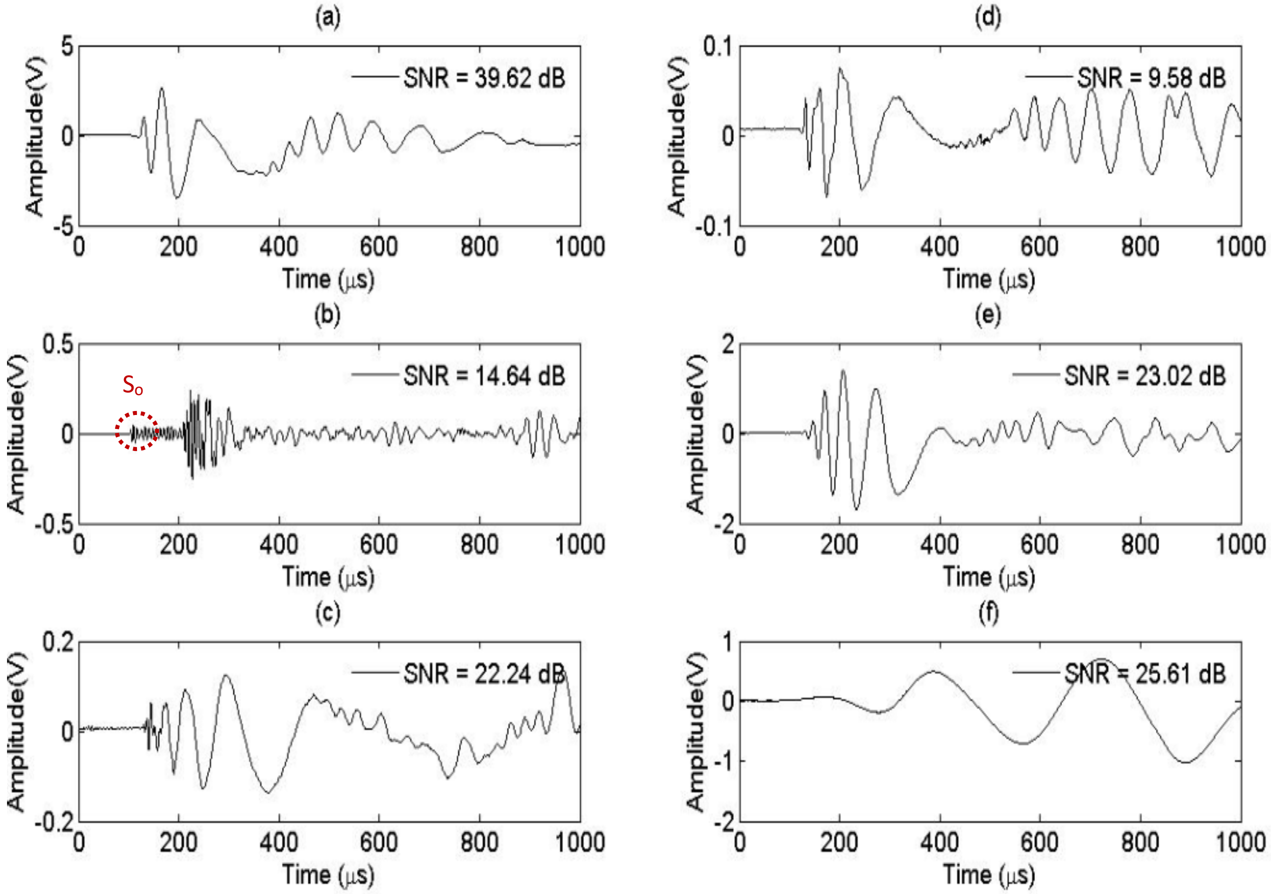

Figure 4-11. Steel ball drop testing results on composite. a. Acellent Single Smart Layer. b. Vallen Sensor 900-RIC. c. Vallen Sensor 900-M. d. Digital Wave B1025T. e. STEMiNC wire lead. f. SteveCo KRNBB-PC.

For low frequency input conditions on thin plate structures, the S_o modes show minimal velocity changes and therefore are considered less dispersive in nature. However, for lower frequency inputs, the modes attenuate much faster therefore making it difficult for time of arrival estimation in larger structures. In such cases, the A_o mode may be of greater use for structural health monitoring of larger areas.

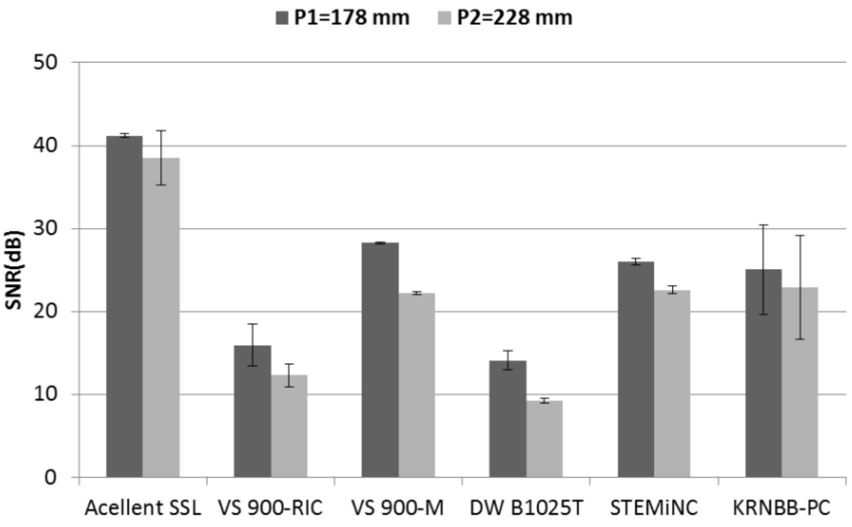

Figure 4-12. Signal-to-noise ratio (SNR) estimation at receiving locations P1 and P2.

For low frequency input conditions on thin plate structures, the S_o modes show minimal velocity changes and therefore are considered less dispersive in nature. However, for lower frequency inputs, the modes attenuate much faster therefore making it difficult for time of arrival estimation in larger structures. In such cases, the A_o mode may be of greater use for structural health monitoring of larger areas.

4.7 Summary and Conclusions

A comparative evaluation of six commercially-available piezoelectric AE sensors was performed to assess their performance in plate wave mode detection and received signal quality using both aluminum and composite panels. The sensors that exhibited higher signal strength and lower wave packet dispersion were preferred for wave mode assessment and time of arrival estimation. Active testing was performed using a transducer to produce an input signal to excite the structure while the receiving AE sensors recorded a response. Arrival times of both the S_o and A_o plate wave modes were determined for each sensor type. Wave mode velocities calculated from the measured arrival times were found to be in good agreement with predictions obtained using both the Disperse code and finite element analysis simulation. In general, the wave modes received in the laminated carbon/epoxy composite panel were more dispersive than in the aluminum panel. Differences in the relative strength of the received S_o and A_o wave modes as well as the overall signal strength and noise levels

were observed between the six sensor types. Additionally, steel-ball drop tests were performed using each sensor type to record the impact response. While both S_o and A_o wave modes were produced, the flexural A_o mode was dominant in the recorded signal response for all sensors investigated. Similar to active testing, lower signal amplitudes of wave modes were observed in the composite panel in comparison to the aluminum panel. Significant differences were observed in the received signal responses for the six sensor types, including the received signal strength and the signal-to-noise ratio.
Good correlation between the time of arrival predictions obtained using Disperse and FE analysis was observed. It was also observed that the signal strength and quality were highly affected by the material properties and instrument responses in addition to the structure response itself. For the impact location estimation algorithm developed in this investigation, accurate initial time of arrival estimation is vital for the impact location assessment and damage evaluation. While a majority of the damage for low-velocity impacts lead to delamination that carry lower frequency components, subsurface damages such as fiber breakage carry higher frequency components and must be identified for source localization. In such a case, sensors that permit accurate amplitude outputs to such event for accurate TOA estimation were desired. Additionally, comparable responses to both low-frequency and high-frequency wave mode components are desired to confidently characterize damage types. While all the sensor types showed comparable results for active testing, the Acellent SSL, VS 900-M, DW B1025T and STEMiNC Wire Lead sensors showed good frequency response results based on signal quality, TOA extraction and comparable SNR deviation over a propagating distance for passive testing conditions.

For in-situ applications, ease of sensor attachment and data acquisition was desired. Acellent's single smart layer and STEMiNC sensors are low profile and easy to bond to the outside of composite structures. However, the moveable Vallen Systeme and Digital Wave's sensors can be moved around as desired for impact location estimation. Additionally, Digital Wave's B1025-T and KRNBB-PC sensors have smaller diameter and are threaded on both ends therefore providing a secure bondage to the test structure. While preamplifiers were convenient for preliminary testing, use of multiple cables and extended transmission time to the data acquisition system may lead to the loss of imperative data. Moreover, reduced impedance mismatch was desired between the source of impact and sensing element for better signal response. Acellent, Vallen 900-M, Digital Wave and STEMiNC sensors have a smaller sensor element providing higher confidence for their depicted wave mode sensitivity and signal quality. Also, it was observed that the sensor element highly affected the mode dominance in these particular tests, with extensional mode prominent in active testing and flexural mode in out-of-plane impact testing.

Based on the testing of all six sensor types, four sensor types, Acellent SSL, Vallen Systeme's 900-M, Digital Wave's B1025T and STEMiNC's Wire Lead sensors showed the most promising results and were recommended for future studies with instrumented low-velocity impact conditions.

5. DAMAGE CHARACTERIZATION UNDER QUASI-STATIC LOADING

Several studies on AE propagation under quasi-static loading conditions in composite materials have been conducted to date. Some of these research studies have focused on time-domain analysis, such as counting the number of acoustic emissions. However, in most of the research on damage classification, AE signal analysis in the frequency domain, especially peak frequency, has focused on damage characterization methods. Figure 5-1 presents a summary of the published relationships between damage types and the peak frequencies (kHz) suggested in previous research [25, 28, 29] using different composites.

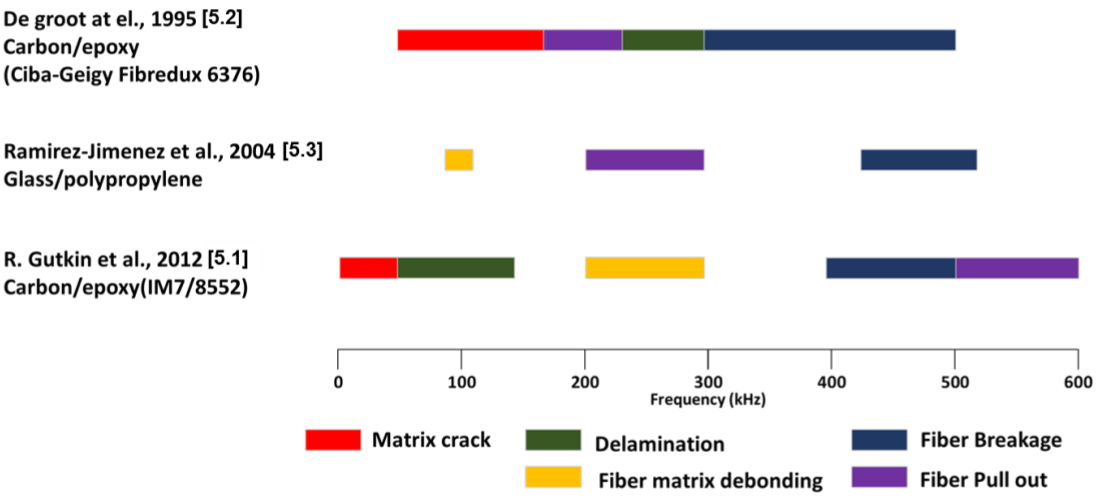

Figure 5-1. Summary of peak frequency findings from previous studies.

The findings of Gutkin et al. [25] are of particular interest because the composite material used in that previous study, IM7/8552 carbon/epoxy have similar material properties with the material IM7/8551 carbon/epoxy used in this investigation.

In these previous studies, several quasi-static test methods including compact tension (CT), end-notched flexure (ENF), and 3-point bending were used in order to produce specific types of damage and related AE signals. Each study provides different AE-signal analyses and classification methods in the frequency domain; however, a noticeable trend can be observed in the results shown in Figure 5-1. Damage types related to fiber failure (fiber breakage, fiber pull out) produce relatively higher frequency components than matrix damage and delaminations. Previous research [60-62] suggests that differences in material properties between fiber and matrix are a primary reason for this. Thus, the intrinsic frequency ranges of AE signals produced by fracture are related to the materials' properties.

Previous studies based on peak-frequency information, as shown in Figure 5-1, provide impressive results for damage classification using AE signals. However, damage classification using peak frequency has limitations for use in impact-AE-analysis because the peak frequency can indicate only the most dominant damage type. Considering that fractures in composite materials usually produce at least two types of damage at the same time, an AE signal can include information related to different types of damage, such as fiber breakage and delamination. For example, a single AE event produced by an impact resulting in severe damage may include information from multiple types of damage. In this case, a damage type estimated by peak amplitude cannot provide definitive information regarding multiple damage types. Thus, based on the peak-frequency findings of previous studies, modifications to existing damage characterization methods are required to characterize multiple-damage states accurately.

This investigation focused specifically on the damage characterization of carbon fiber reinforced polymer (CFRP) composites by means of AE signals produced under quasi-static loading conditions. Based on the findings of previous studies, this study emphasized effective damage-state characterization using AE signals produced by multiple damage types. Initially, matrix cracking (single damage state) and combined fiber /matrix damage (multiple damage state) were identified as the two targeted damage states for the development of the multiple-damage characterization method.

5.1 Experimental Methods

To produce the desired targeted damage types, both four-point bending tests using customized specimens and modified Double Cantilever Beam (DCB) testing were performed. All mechanical tests were performed using an Instron 4303 Universal Test Machine under constant displacement loading and a National Instruments PXIe-1073 Data Acquisition (DAQ) system.

Four-point bend-testing shown in Figure 5-2 was selected in an effort to produce strong AE signals at the moment of specimen failure. Because of the expected relationship between the AE signals produced by specimen failure and the resulting damage state, it was expected that a direct comparison was possible between the AE signals produced by different damage types. In order to produce the intended damage states using four-point bend- testing, suitable specimen and loading parameters were selected based on preliminary tests.

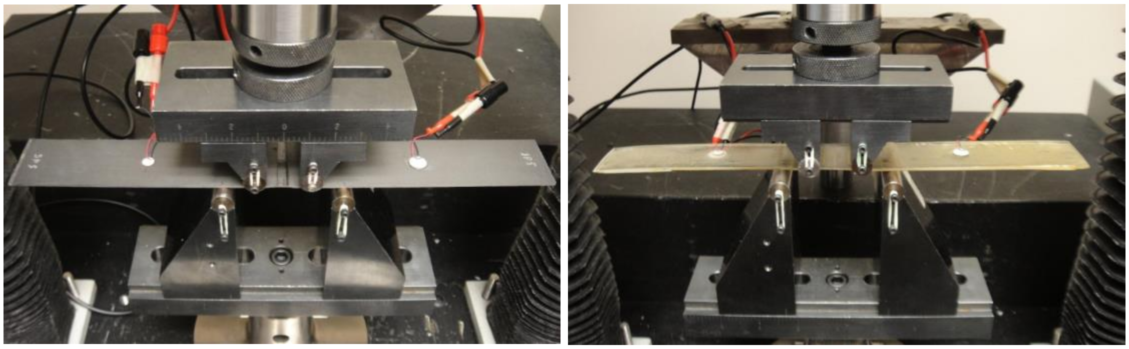

(a) (b)

Figure 5-2. Test setup of four-point bending and DCB tests. (a) Composite specimen. (b) Bulk matrix specimen.

Specialized specimens were fabricated for producing the two targeted damage types in the central section of test specimens. Bulk matrix specimens composed of Fiber Glast 2000 Epoxy Resin with Fiber Glast 2120 hardener were used for producing AE signals produced only by matrix failure. Unidirectional composite specimens fabricated from IM7/8551 carbon/epoxy prepreg tape were used to produce failure of both fiber and matrix materials. Considering the sensor position and fixture size, the composite specimens shown in Figure 5-3 were 300 mm in length, 38 mm in width, and 2 mm in thickness. However, changes in layup and geometry at the middle of the composite specimen were used to produce AE signals in the middle of the specimen thickness and to produce the desired signal strength. The different notch shapes used at the top and bottom of the specimen were designed to prevent the generation of delaminations prior to final failure and to provide sufficient strength to enable specimen failure at the intended loading condition.

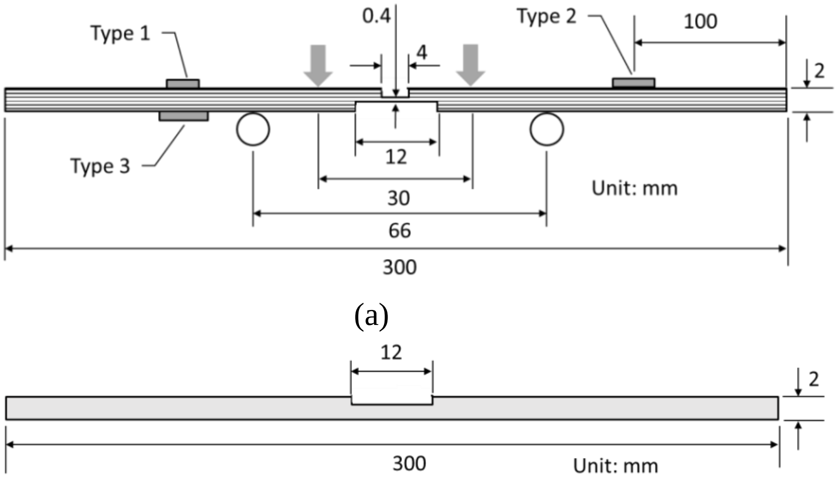

(a)

(b)

Figure 5-3. Schematics of test setup and specimens. (a) Composite specimen and setup. (b) Bulk matrix specimen.

The bulk matrix specimens were fabricated to the same size as the composite specimens. The middle section also was notched in an effort to produce a failure at the intended location and to produce the desired signal strength for the DAQ system.

Three different models of STEMiNC Piezo Disc type sensors listed in Table 5-1 were selected for receivers in order to compare responses from each sensor. Figure 5-4 shows the three types of sensors. A specialized adhesive was used for sensor attachment and the sensors were permanently attached to the specimens.

The three sensors were attached to the side, top, and bottom of the specimen while maintaining the same distance from the center of the specimen, as shown in Figure 5-3 (a).

Modified Double Cantilever Beam (DCB) testing, shown in Figure 5-5, was conducted to produce small increments of delamination growth and their associated AE signals under quasi-static loading. Unlike the conventional DCB test procedure used to measure facture toughness, a continuous 5 mm/min displacement loading was applied until the delamination reached a length of 125 mm.

AE signals collected from the DCB specimen were analyzed using traditional as well as newly suggested damage characterization methods. The relatively low amplitude AE signals produced by the small increments of delamination growth required that the trigger level for data acquisition was reduced to 0.02 volts. Due to the large number of AE signals from the DCB tests efficiently, a stochastic analysis method using 3D histogram was implemented to produce a representative set of AE signals produced by delamination. This test method was used to investigate effects due to changes in composite material, ply layup, laminate thickness, and delamination locations through the laminate thickness.

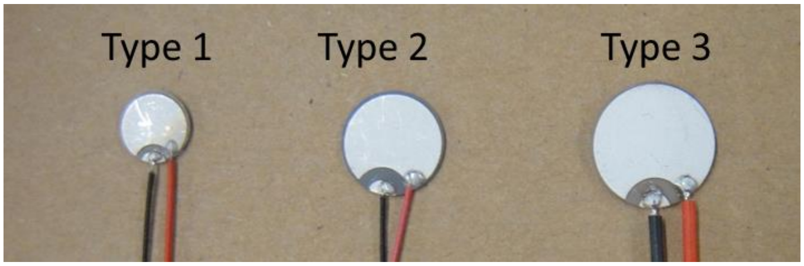

Figure 5-4. STEMiNC Sensors used for four-point bending and DCB test.

Table 5-1. Information Related to Sensors Used

ID	Model	Resonance frequency	Materials
Type 1	SMD07T05R412WL	4.25MHz	SM412
Type 2	SMD10T04R111WL	5MHz	SM111
Type 3	SMD12T06R412WL	3.4MHz	SM412

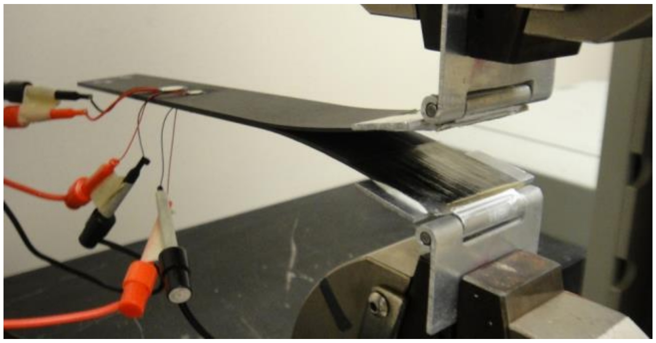

(a)

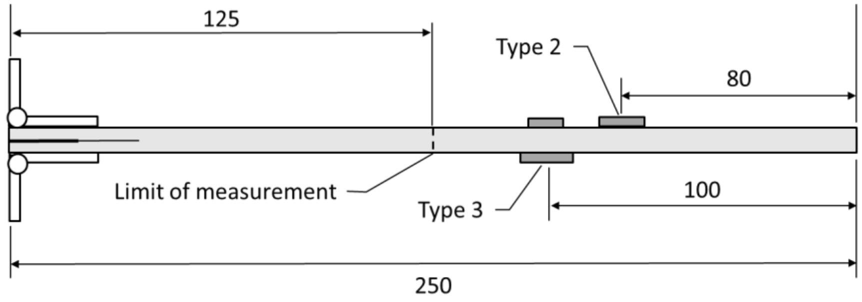

(b)

Figure 5-5. DCB test configuration. (a) Test setup. (b) Schematics of test specimen.

Various modifications were made to the DCB test specimen configuration (ply layup, delamination position, specimen size and thickness) to identify the characteristic changes of AE signals due to these configuration variations. Table 5-2 presents detailed information for each type of specimen investigated. Following mechanical testing, visual and digital microscope inspections were conducted to identify the damage states produced. All AE signals collected from DCB testing were filtered using a bandpass filter (20~ 600 kHz range) in order to remove sonic components in the low-frequency range and high- frequency range. Filtered signals were subsequently screened by peak amplitude in order to eliminate unrelated AE signals from other sources.

Table 5-2. Types of DCB Test Specimens

ID	Composite materials	Lay-ups	Delamination location	Thickness	Feature
Type A	IM7/8551	$[0]_{16}$	Middle	2.4	Reference
Type B	IM6/3501	$[0]_{28}$	Middle	2.2	Material
Type C	IM7/8551	$[0]_{32}$	Middle	4.8	Thickness
Type D	IM7/8551	$[0]_{32}$	Quarter	4.8	Delamination location

5.2 Results and Discussion

Figure 5-6 shows failed sections of both bulk matrix and composite four-point flexure specimens. The majority of the four-point bend specimens produced only one AE event corresponding to the final specimen failure. However, some bend tests produced multiple AE events following the triggering point that were also included in the data analysis. In total, 19 AE events were produced from four-point bending tests: 4 from bulk matrix specimens and 15 from composite specimens. Because three different types of STEMiNC sensors were used to record each AE event, a total of 57 recorded AE events were used for damage type characterization. Figure 5-7 (a) shows the time domain and FFT plots of AE signals produced by failure of the bulk matrix specimen. Figure 5-7 (b) presents the time domain and FFT plots of AE signals produced by failure of composite specimens.

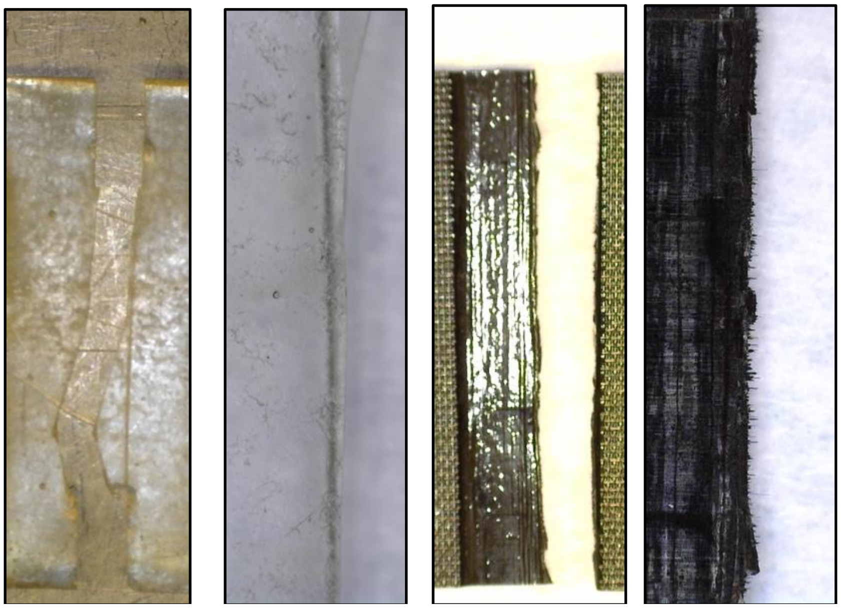
(a) (b) (c) (d)

Figure 5-6. Inspection of four-point bend specimen failure surfaces. (a) Bulk matrix specimen. (b) Magnified bulk matrix specimen, 35x. (c) Composite specimen. (d) Magnified composite specimen, 35x.

These results show that the three different types of sensors provide different frequency responses. Figure 5-7 (b) shows that differences exist in the AE signals recorded by the three sensor types for frequencies over 200 kHz. This finding suggests that the AE response within the frequency range for damage classification can be affected by the sensor type used. However, general trends may be observed by comparing the results obtained from the bulk matrix and composite specimens in Figures 5-8 (a) and (b), respectively.

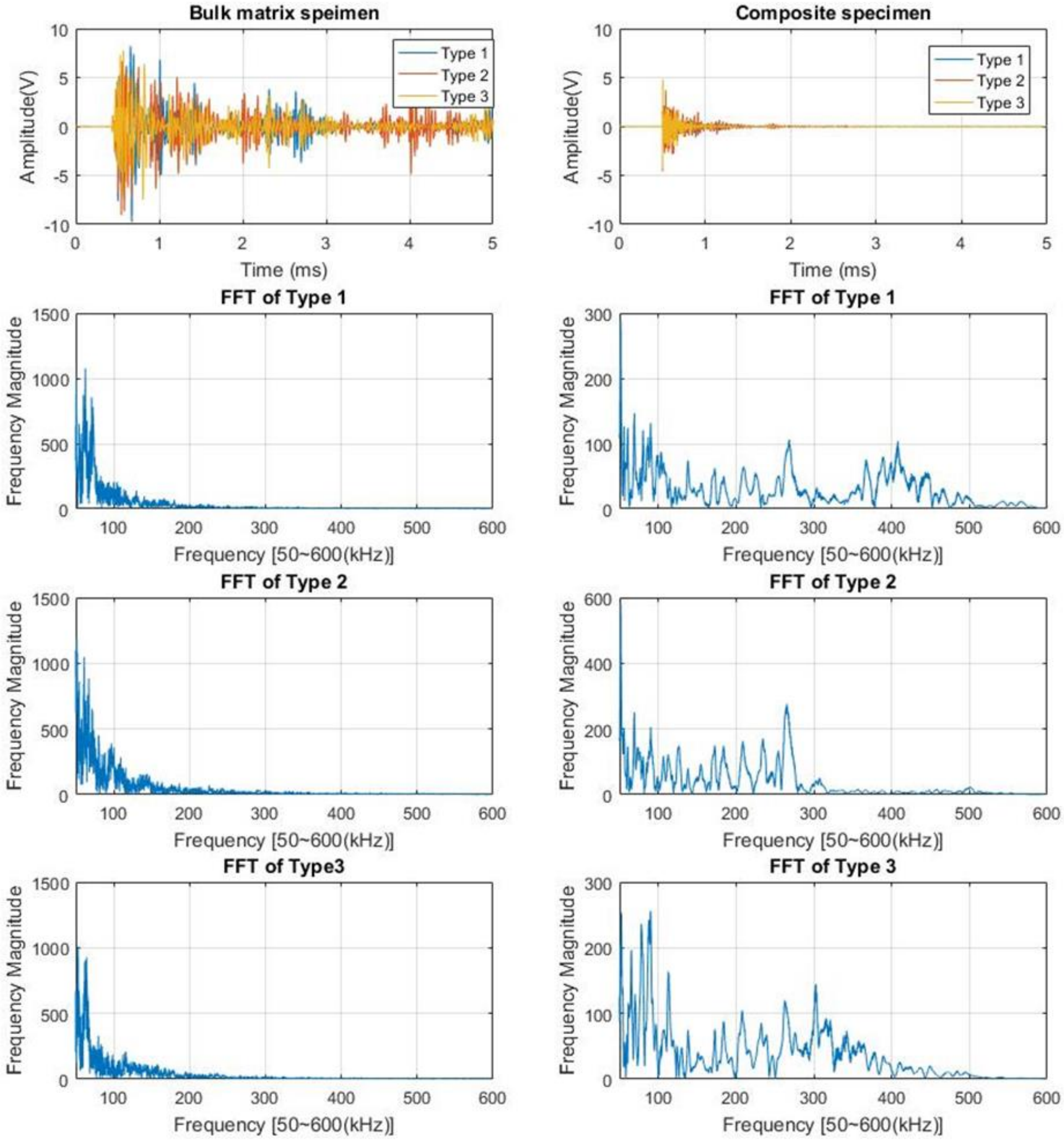

(a) (b)

Figure 5-7. Raw data and FFT plots of AE signals produced by three sensor types. (a) Bulk matrix specimen failure. (b) Composite specimen failure.

Based on the frequency response of the three AE sensors used as well as the findings of previous studies [25], the two wide-frequency ranges were identified for signal analysis: 0-200 kHz corresponding to matrix damage and 200 – 600 kHz corresponding to fiber damage.

Another important consideration is that the peak frequency of AE signals cannot provide correct information regarding the damage state when multiple types of damage are produced during the same AE event. The test conditions and inspection results shown in Figure 5-6 indicate significant fiber breakage occurred in the composite specimens; however, the peak frequencies shown in Figure 5-7 (b) are below 100 kHz because the frequency component related to matrix damage is hidden by the frequency component related to fiber damage. Thus, the peak frequency can indicate only one type of damage.

Figure 5-8 shows the peak frequencies of all AE signals from two different damage states. These results further suggest that the peak frequency cannot provide adequate information for damage characterization when multiple types of damage are created.

Frequency centroids of AE signals, which are also commonly used as an indicator of damage, are shown Figure 5-9 for both the bulk matrix and composite four-point bend specimen tests. The frequency centroid was found to provide improved identification of the different damage types relative to the peak frequency results. However, the frequency centroid method also cannot provide a clear identification of damage when multiple types of damage are produced because the relationships between the frequency range and damage type are not clearly defined.

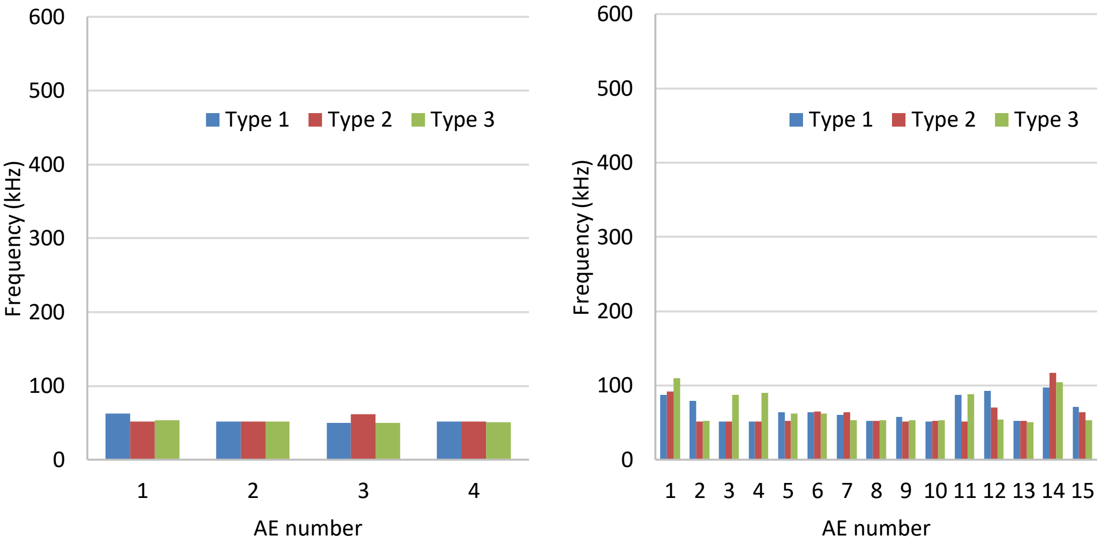

(a) (b)

Figure 5-8. Peak frequency of AE signals. (a) Bulk matrix specimens. (b) Composite specimens.

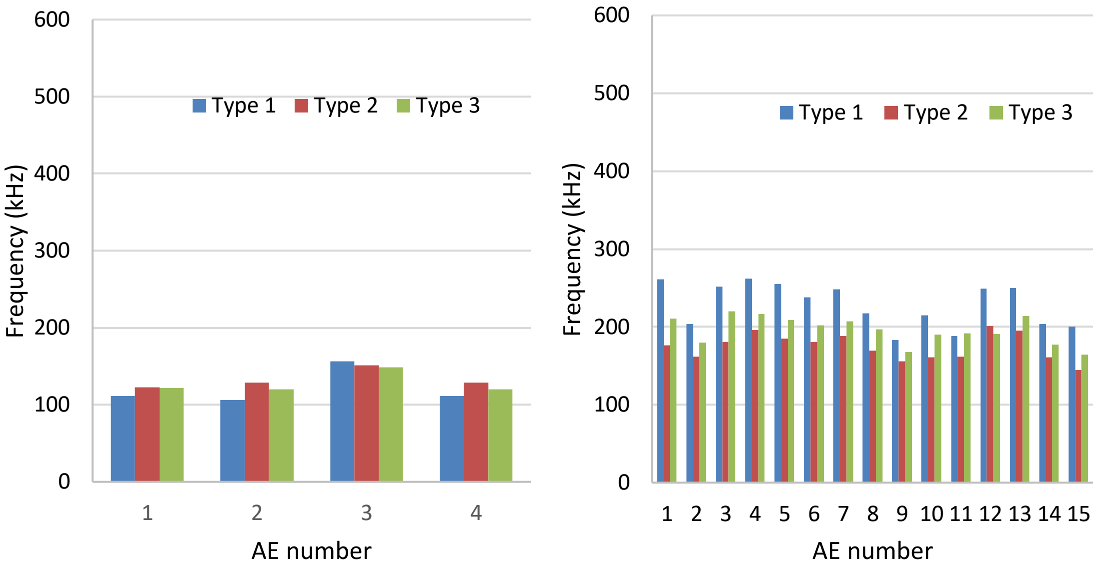

(a) (b)

Figure 5-9. Frequency centroid of AE signals. (a) Bulk matrix specimens. (b) Composite specimens.

Thus, both of the commonly used frequency parameters were unable to properly characterize multiple damage states.

In this investigation, the use of the frequency magnitude ratio was proposed for use in damage characterization of combined fiber/matrix damage states. The frequency magnitude ratio is defined as

$$\text{frequency magnitude ratio} = \frac{\sum_{M}^{N} f(n)}{\sum_{L}^{N} f(n)}, \qquad (3.1)$$

where L, M, and N are bin numbers of selected frequencies, respectively 50, 200, and 600 kHz.

Therefore, the sum of the frequency magnitude in the range of fiber damage (200 -600 kHz) is divided by the total of frequency magnitude in the entire range (50 – 600 kHz).

A ratio value close to 0 implies that the AE signal corresponds to matrix damage whereas a value close to 1 implies fiber damage. Ratio values in the mid-range between 0 to 1 imply a combined damage state.

Figure 5-10 shows the frequency magnitude ratio calculated from all recorded AE events during four-point bending testing. The results show a clear distinction between the matrix-only damage states and the combined fiber and matrix damage states. Figure 5-11 shows results from the inspection of fracture surfaces from DCB specimens using a digital microscope. The fracture surfaces were placed into four categories and labeled as type A, B, C, and D.

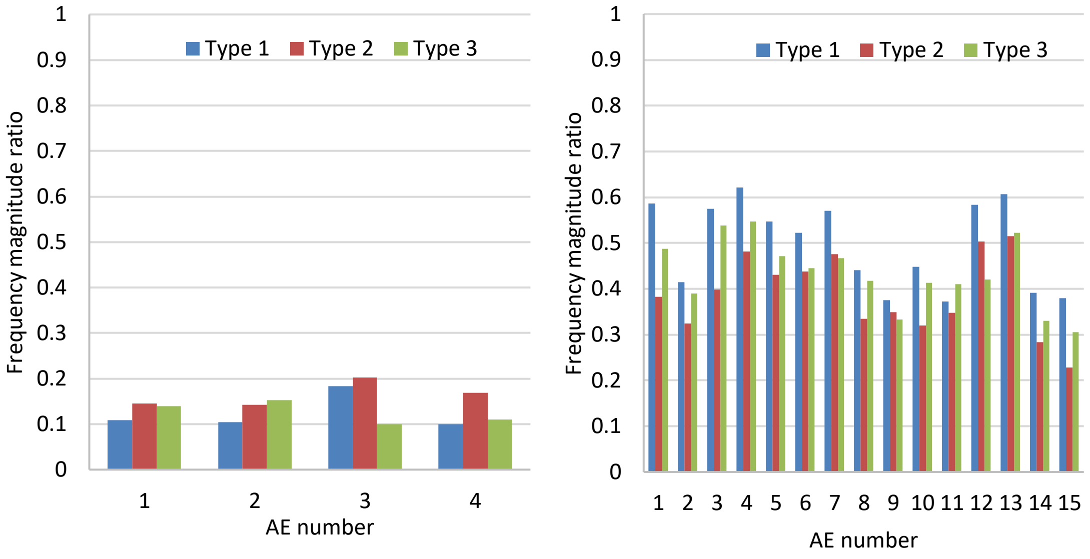

(a) (b)

Figure 5-10. Calculated frequency magnitude ratios for all AE events during four-point bend testing. (a) Bulk matrix specimens. (b) Composite specimens.

Surface type A, shown in Figure 5-11 (a) represents the reference case in Table 5-2 and shows a relatively clean surface with little fiber bridging. Surface type B, shown in Figure 5-11 (b), shows considerable fiber breakage due to fiber bridging, and was typical of the IM6/3501 used to investigate effects of different composite materials. Surface types C and D, which were produced in specimens with twice the normal thickness and with different through-thickness delamination positions, also showed increased fiber damage.

Additionally, the size of the broken-fiber bundles produced in surface types C and D were larger than those found in surface type B. Although surface types C and D have similar damage states, inspection results show that type D surfaces displayed longer broken-fiber bundles than type C surfaces.

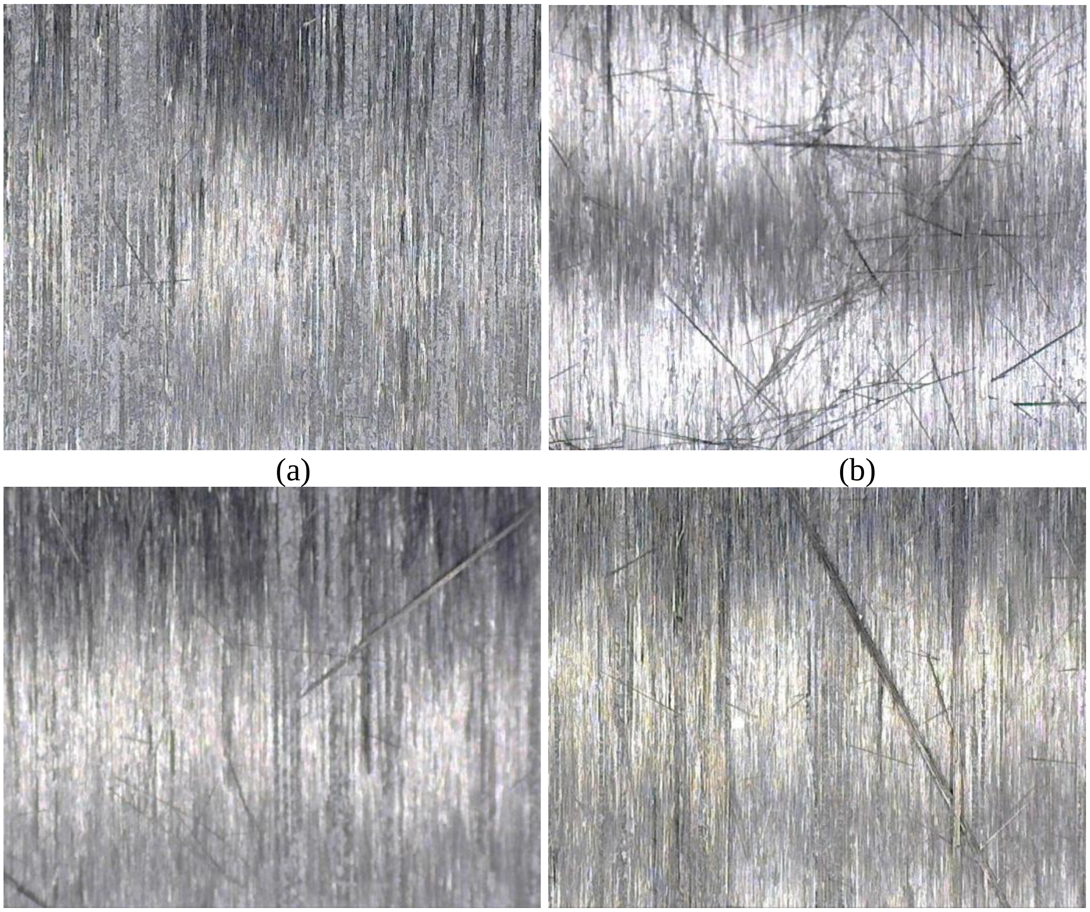

(a) (b)

(c) (d)

Figure 5-11. Magnified (220x) DCB specimen fracture surfaces. (a) Type A. (b) Type B. (C) Type C. (d) Type D.

Figure 5-12 shows the AE signal frequency that produced the peak amplitude in the DCB specimens with the Type A (reference) fracture surfaces. These results show that frequencies corresponding to the peak AE signal amplitude were concentrated in the 50 – 100 kHz range, in agreement with results from previous research [25].

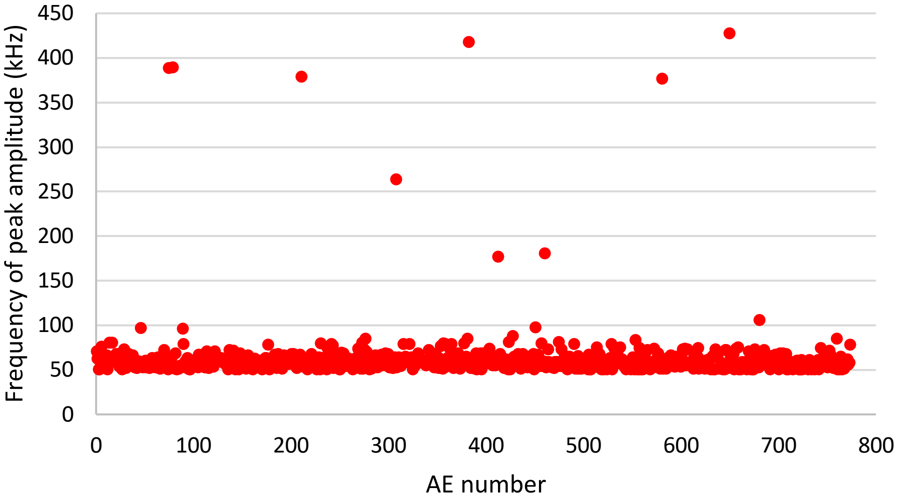

Figure 5-12. Peak amplitude AE signal frequency produced by Type A (reference) fracture surfaces.

Figure 5-13 shows the frequency magnitude ratio calculated using the same AE signals, which results show a more scattered distribution than the peak-frequency plot in Figure 5-12. This finding implies that many of the AE signals include fiber-damage related AE signals while preserving the frequency with the peak amplitude due to delamination. The plot shows that a majority of the AE events produce a frequency magnitude ratio between 0.3 and 0.5. Considering the range of frequency magnitude ratios produced from the 4-point bend tests shown in Figure 5-10, the ratio values obtained from DCB testing are located between the four-point bend testing of the bulk matrix specimens (0.1-0.2) and the composite specimen (0.4-0.6).

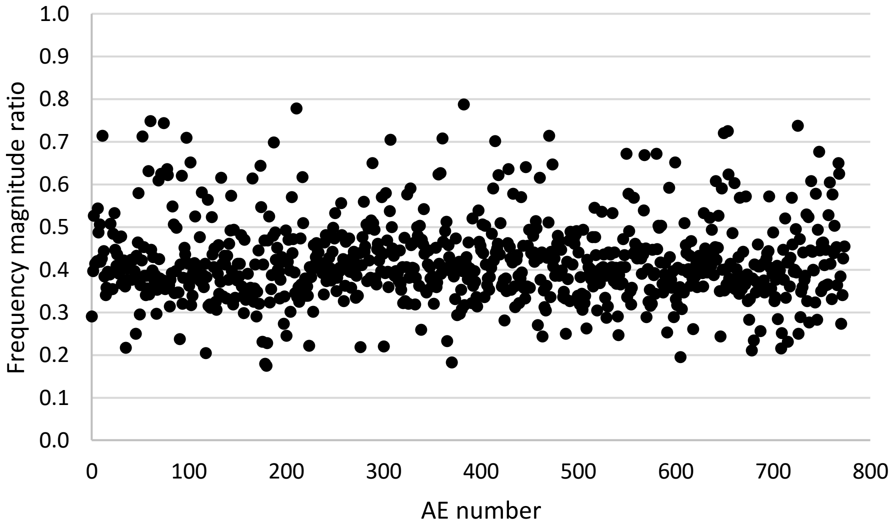

Figure 5-13. Frequency magnitude ratio of frequency magnitude sum of DCB test with Type A specimens.

In order to determine the two characterization parameters simultaneously based on a number of AE signals, a stochastic analysis was conducted using 3D histograms. Figure 5-14 shows the 3D histograms calculated using AE signals associated with all of the DCB fracture specimens. To produce a histogram for each characterization parameter, multiple bins were created with a range of 10 kHz for the frequency of peak amplitude and 0.02 for the frequency magnitude ratio. A representative AE signal can be estimated through these 3D histograms. For example, Figure 5-14 (a) shows a peak corresponding to a 50-60k Hz frequency of peak amplitude and 0.38-0.4 frequency magnitude ratio. Figure 5-14 (b) shows a similar frequency of peak amplitude, but corresponding to a higher frequency magnitude ratio value. Considering that a high frequency magnitude ratio corresponds with a large portion of fiber-damage related AE, the increased frequency magnitude ratio in Figure 5-10 (b) from the composite bend specimens reflects the inspection results shown in Figure 5-11 (b) for the DCB specimens with considerable fiber breakage due to fiber bridging.

The results of Figure 5-14 (c) and (d) show a more distinctive difference from the reference case shown in Figure 5-12 (a). The plots show two groups of AE signals which have peak frequencies in the 50-60 kHz and 380-390 kHz ranges. Both the frequency of peak amplitude as well as the frequency magnitude ratio suggest that the AE signals are primarily associated with fiber damage. The peak located at a frequency of 50 – 60 kHz peak was moved to a frequency magnitude ratio in the range of 0.6 - 0.7., suggesting that the specimen had a greater portion of fiber damage. An interesting trend is observed by comparing results corresponding to DCB fracture surface types B, C & D. These three cases have increased fiber damage; however, type B does not show the level of change relative to the reference configuration (type A) as for types C and D. This observation suggests that the AE signals produced by fiber breakage in the type B specimens were considerably weaker than those of types C and D. Note that the fiber breakage size shown in type B is considerably smaller than that observed in types C and D, primarily due to material differences. Thus, the fiber-breakage related AE signals in type B specimens may not have produced sufficient signal amplitude to significantly change either the frequency of peak amplitude or the frequency magnitude ratio.

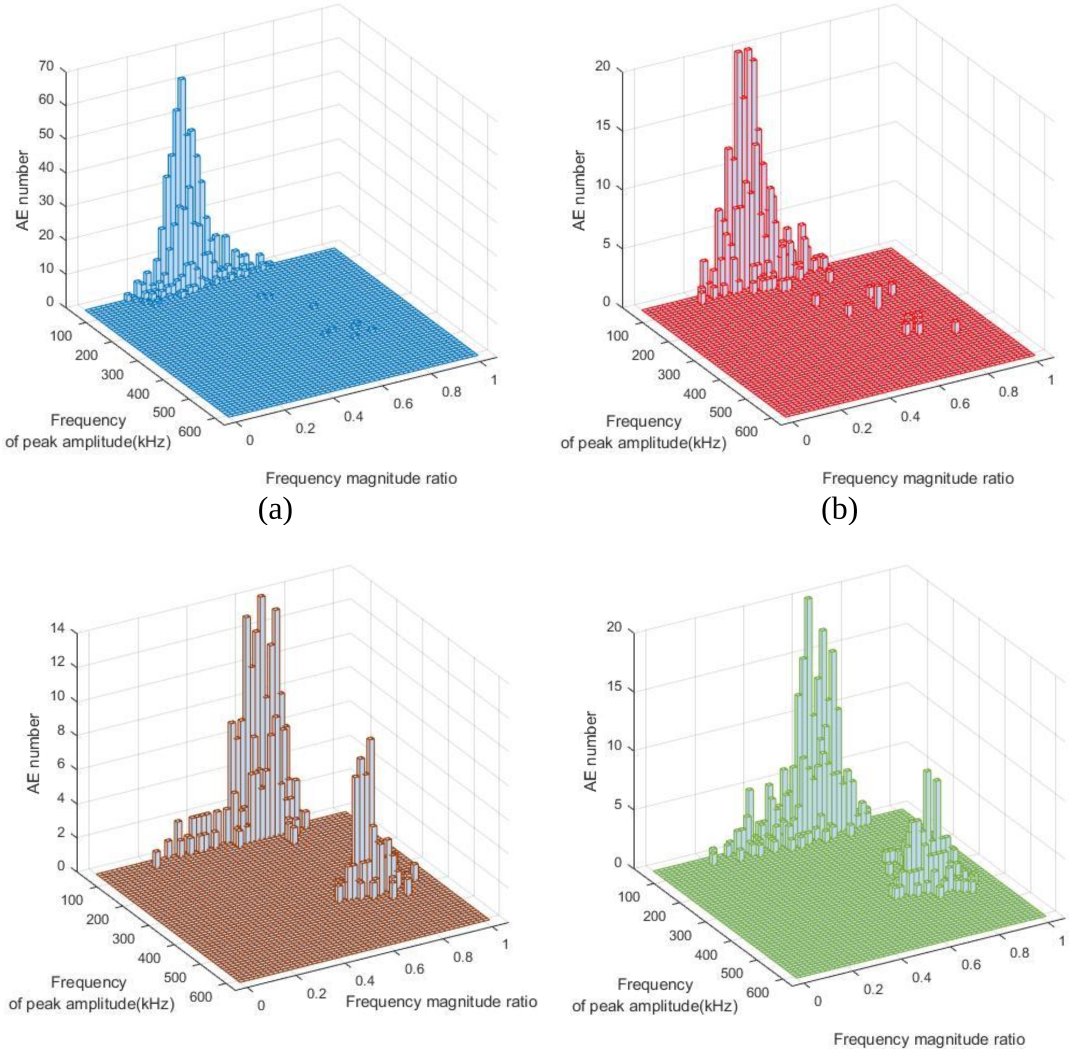

(a) (b)

(c) (d)

Figure 5-14. 3D histograms of AE signals from DCB fracture specimen. (a) Type A. (b) Type B. (c) Type C. (d) Type D.

Based on the results obtained from DCB testing, this evaluation method using 3D histograms shows potential as an AE-based damage characterization method. Tracking of the two proposed parameters, frequency of peak amplitude and frequency magnitude ratio, appears to be of use in determining types of damage when multiple damage types are produced.

5.3 Summary and Conclusions

Quasi-static testing of composite panels was performed to characterize damage states in composite materials using AE signals. The two representative types of damage, matrix failure as well as combined fiber and matrix failure, were investigated for classification using AE signals. A specialized four-point bend test specimen was developed to investigate each damage state under quasi-static loading. Additionally, DCB testing was performed on specimens that exhibited four different types of fracture surfaces that differed in the quantity and type of fiber breakage due to fiber bridging. The results of four-point bend testing with two customized types of specimen suggest that the peak frequency as well as the frequency centroid, traditional AE parameters in the frequency domain, do not provide useful information when a multiple-damage state is produced. However, a proposed damage characterization parameter, referred to as the frequency magnitude ratio, shows potential for identifying damage types produced in cases where both single and multiple damage types are produced in a test.

The inspection of fracture surfaces of DCB test specimens following testing suggests that frequency characteristic of the AE signals produced may be of use for identifying the occurrence of fiber breakage during the propagation of a delamination. Further, 3D histogram plots constructed using the frequency of peak amplitude as well as the frequency magnitude ratio provide additional detailed information on the damage state, especially when multiple damage types are produced.

6. IMPACT DAMAGE CLASSIFICATION IN COMPOSITE PLATES

Unlike most metallic materials, fiber-reinforced polymer matrix composites are composed of two different constituents that experience different types of fracture. Previous researchers [60, 61, 62] have suggested that the relationship between intrinsic frequencies f_i and elastic acoustic velocities C_i of acoustic emissions resulting from fracture are dependent on the elastic moduli E_i and densities ρ_i,

$$f_i \sim \frac{1}{\tau_i} \sim C_i \sim \sqrt{\frac{E_i}{\rho_i}} \tag{6-1}$$

Thus, different intrinsic frequencies produced by fractures in the reinforcing fiber and matrix material can be used for damage classification. Previous research on acoustic emission due to damage creation in fiber-reinforced composites under quasi-static loading suggests the relations in equation (6.1) are valid for damage classification [28, 29, 63-66]. Figure 6-1 presents a summary of published relationships between damage types and the resulting frequencies (kHz) observed from the six investigations that used different composite materials and loading methods. A total of four damage classifications are listed: matrix damage, fiber pull-out, interlaminar ply delamination, and fiber breakage. The summarized results suggest that fiber damage produces higher frequency emissions than matrix damage and delamination.

Although frequency domain-based damage classification in composite materials has shown progress under quasi-static loading conditions, it requires additional consideration for damage produced by impact loading.

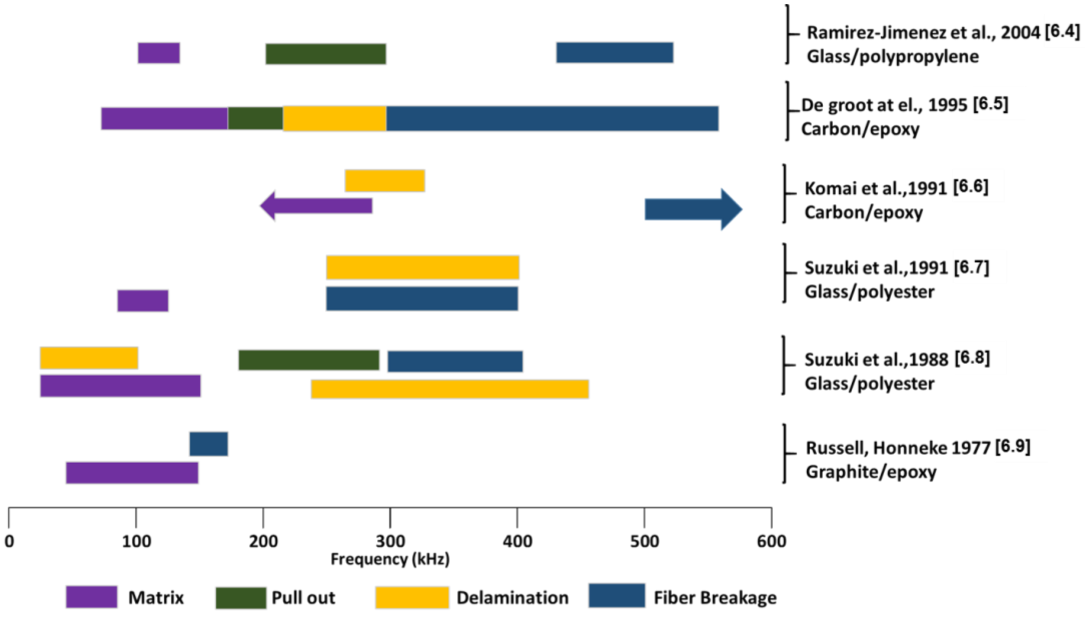

Figure 6-1. Damage type versus resulting frequency from previous investigations.

Variability in impact conditions, such as boundary conditions and impactor mass, shape, and impact energy can cause unexpected changes in damage state and acoustic emissions. Additionally, most impacts produce at least two types of damages at the same time and make it challenging to classify damage types using only acoustic emissions.

In this investigation, an experimental approach was used to classify impact damage in carbon fiber reinforced composite plates using acoustic emission signals. Initially, experimental procedures were developed to produce targeted damage types under impact loading. Damage states were characterized using both non-destructive and destructive inspection methods. Based on correlations between characterized damage and resulting acoustic emission signals, frequency ranges resulting from specific damage types were identified from impact force curves and waterfall FFT plots. Additionally, a damage evaluation method using filtering and enveloping of signals was investigated for use in quantifying the damage produced by the impact.

Although diverse damage states may be produced when impacting composite materials, two targeted damage types were identified for investigation: matrix damage dominated and fiber damage dominated. Additionally, drop-weight impacts that did not produce detectable damage were performed as well. Since the fiber reinforcements are of primary importance for both structural stiffness and strength, the detection of fiber damage, particularly fiber breakage, during impacting is of critical importance for an SHM system. However, post-impact inspections are typically performed using ultrasonic C-scanning, which provides information on the extent of matrix damage including interlaminar delamination damage. Therefore, the development of an SHM system that can detect the occurrence of both matrix damage and fiber damage is of great interest.

6.1 Experimental Methods

6.1.1 Impact Testing

Instrumented drop-weight impact testing was performed using a pneumatically-assisted Instron Dynatup 8250 HV drop tower as shown in Figure 6-2 (a). An impacting mass of 4.75 kg was used for all tests. To generate a range of damage severities, a series of impact energies ranging from 1.2J mm to 14.2J were used. All impact testing was performed using 152 mm x 304 mm IM7/8551carbon/epoxy composite panels. The 2.4 mm-thick panels were fabricated using eight unidirectional prepreg plies arranged into a $[0/90]_{2S}$ symmetric cross-ply layup.

Variations in the panel support conditions as well as the impactor geometry were used to produce the desired targeted damage states. Two types of support conditions were used to vary the global panel deflection allowed during impacting and thus the resulting damage states. A back face-supported condition, as shown in Figure 6-2 (b), was used to minimize global panel deflection and produce localized impact damage in the vicinity of the impactor. As a result, this support condition was expected to produce localized fiber damage and minimal matrix damage in the vicinity of the impact. In contrast, an edge-supported condition, as shown in Figure 6-2 (c), allowed for global deformations and thus matrix damage (primarily delamination) to occur, while reducing the localized impact force that produced fiber damage. To produce the edge-supported condition, a 76 mm x 127 mm rectangular central cut-out was machined into the lower support plate support and the edges rounded to prevent stress concentrations. For both support conditions, a 3.8 mm thick silicon rubber pad, as shown in Figure 6-2 (d), was placed under the specimens before placing the specimen onto the support.

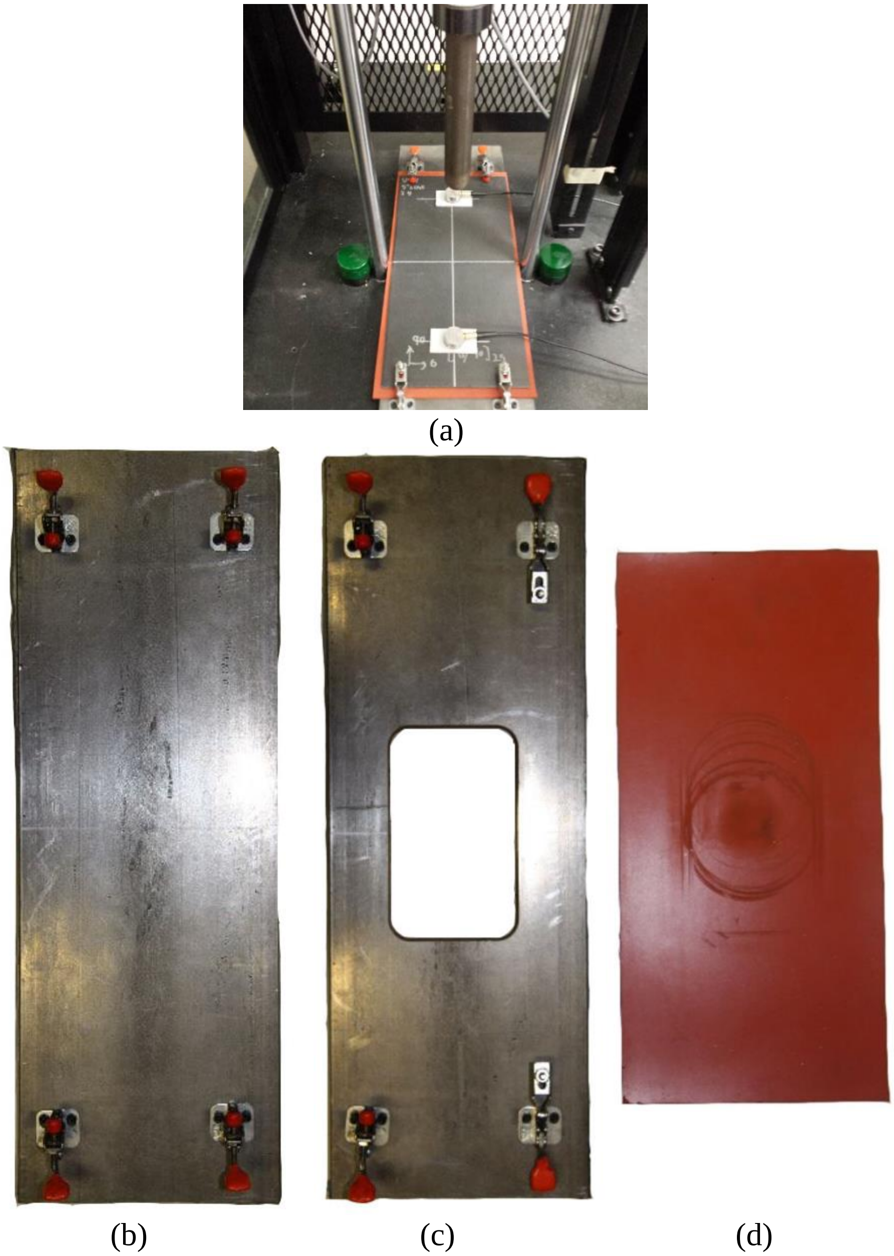
(a)

(b) (c) (d)

Figure 6-2. Test setup used for impact on composite panels. (a) Impact test setup. (b) Bottom plate for back face-supported condition. (c) Bottom plate for edge-supported condition. (d) Silicon rubber pad.

A 25 mm diameter hemispherical impactor was used in producing the two different damage states with both the back face-supported condition and the edge-supported condition. Depending on the support conditions used, the same impactor can produce fiber damage in the panel within the localized region of contact while minimizing matrix damage (back face-supported) or can alternatively minimize fiber damage while permitting matrix damage (edge-supported).

A total of 74 composite test panels were impacted—38 using the edge-supported conditions and 36 using the back face-supported conditions. All impacts were conducted on the geometrical center of the panel and two Vallen Systeme VS900-M acoustic emission sensors were placed 100 mm from the impact position on opposite ends of the panel as shown in Figure 6-2 (a). A National Instruments PXIe-1073 data acquisition system was used in conjunction with the Impulse data acquisition software to record the sensor signal responses using a 2MHz sampling rate. National Instruments LABVIEW and MATLAB scripts were used for subsequent signal processing. The impact force curves were synchronized with the AE signals for further analysis.

6.1.2 Inspection Methods

A series of impact conditions were selected in order to produce targeted damage states in a repeatable manner. The two different support conditions were selected as a primary parameter to produce different amounts of global deflection using the same impact energy, and thus different damage states. Figure 6-3 shows representative damage areas obtained from C-scan ultrasonic inspection for both the back-face supported and edge-supported impact conditions.

For each support condition, C-scan images are shown for the minimum impact energy at which damage was indicated as well as the maximum impact energy used (14.2J). Although the indicated damage area in the localized region of impactor contact may contain fiber damage, the majority of the indicated damage area shown is produced by interlaminar delaminations. The minimum impact energy for damage indication was 1.2J for the back face-supported condition and 4.7J for the edge-supported condition. At the maximum impact energy of 14.2J, the damage area produced using the edge-supported conditions were larger than those produced using the back-face supported conditions, in spite of the same impact energy. The elliptical damage shape produced using the edge-supported condition shown in Figure 6-3 (b) was believed to result from the 75 mm x 125 mm rectangular shaped cut-out in the lower support plate support: a longer delamination length was produced along the longer length of the cut-out.

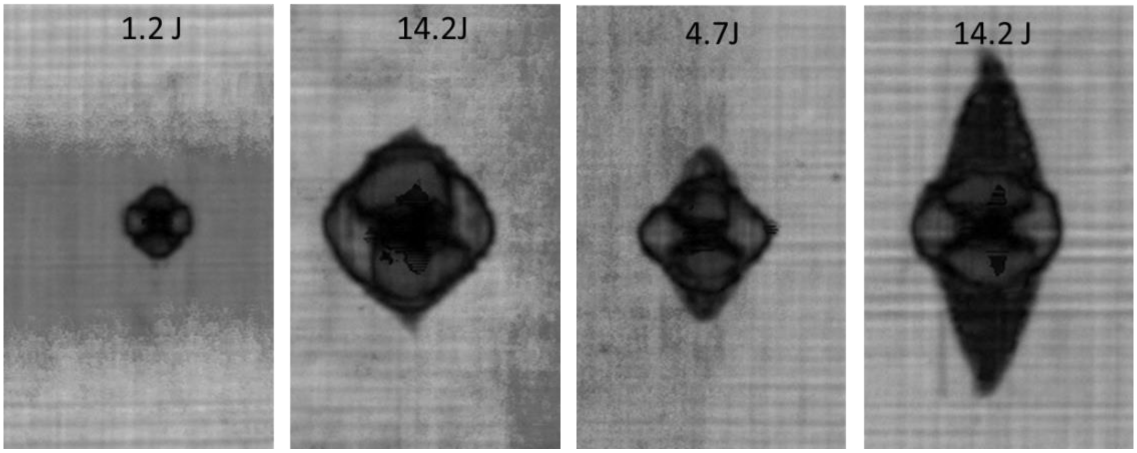

(a) (b)

Figure 6-3. C-scans of impacted specimens. (a) Edge-supported condition. (b) Back-face supported condition.

Following C-scan inspection, a thermal deply procedure was used to assess the fiber damage produced by impacting. Unlike the ultrasonic inspection, thermal deply is a destructive evaluation procedure in which the polymer matrix is pyrolyzed in a high-temperature furnace. A thermal deply system was configured using a Jelenko Accu-Thermal II 150 furnace combined with carbon and water filters, as shown in Figure 6-4. The central section of the composite panel containing the impact damage was cut out and placed into the furnace. Following pyrolysis of the polymer matrix, the remaining fibers from each ply of the laminate were separated and both surfaces of the ply were inspected and photographed using a digital microscope under 40X magnification.

Figure 6-4. Thermal deply system.

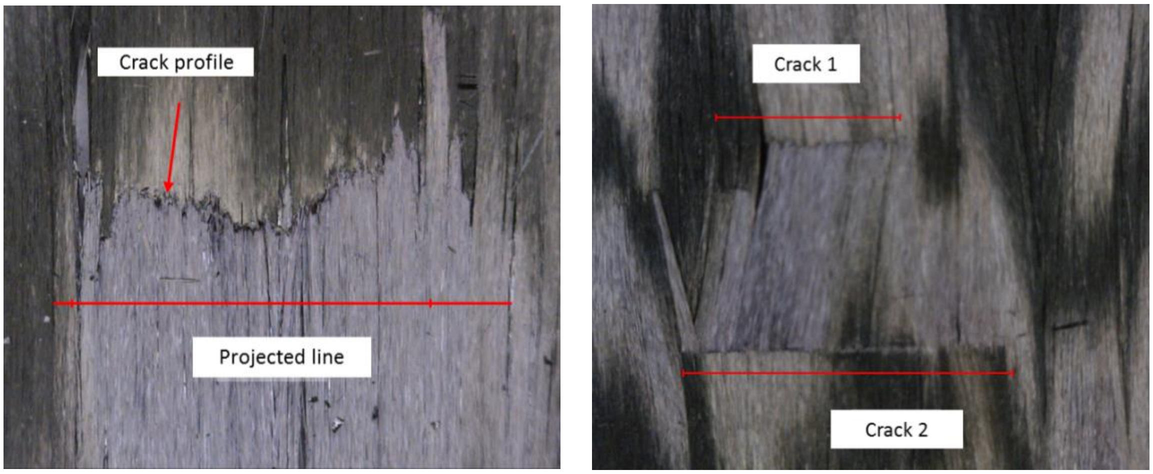

(a) (b)

Figure 6-5. Thermal deply of impacted specimens. (a) Fiber crack and projected line. (b) Multi cracks.

Representative fiber cracks observed following thermal deply are shown in Figure 6-5. When determining fiber crack lengths, measurements were made perpendicular to the fiber direction, although some cracks were oriented at other angles as shown in Figure 6-5 (a). Multiple fiber cracks produced at different locations along the same group of fibers, as shown in Figure 6-5 (b), were counted separately. Although the additional fiber cracks within the same fibers would not be expected to produce additional strength reductions, the additional cracks were included for the purpose of relating the total measured length of fiber cracking to the intensity of the received AE signal. Fiber crack length measurements were based on the visible length on the surface of the ply, independent on the depth of the crack or whether the crack extended throughout the ply.

6.2 Results and Discussion

6.2.1 Characterization of Damage States Produced by Impacts

Comparisons of the impact damage produced using the back-face supported condition versus the edge-supported condition are shown in Figure 6-6 for impacts produced at impact energies ranging from 1.2 J to 14.2 J. Figure 6-6 (a) shows the total planar matrix damage area in each panel obtained from ultrasonic C-scan inspection. Using the back face-supported condition, the planar matrix damage area increased with increasing impact energy. Above an impact energy of 9.5 J, however, the rate of increase in matrix damage area decreased. The maximum matrix damage areas measured were between 500-600 mm^2. Using the edge-supported condition, no significant delamination area was detected for impact energies ranging from 1.2 J to 4.7 J. At an impact energy of 5.7 J, matrix damage areas between 300-400 mm^2 appeared. With increasing impact energy, the matrix damage area continued to increase at a relatively constant rate to maximum values between 700-800 mm^2.

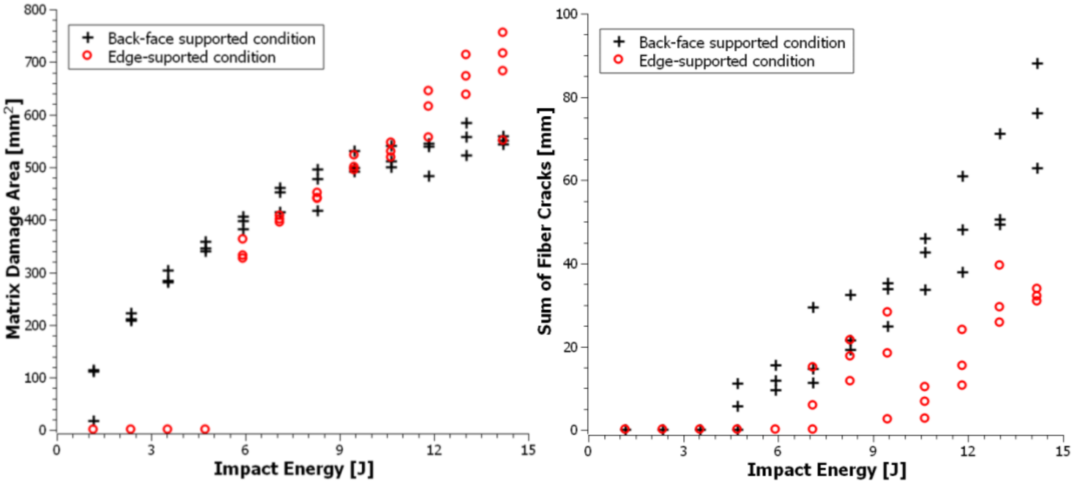

(a) (b)

Figure 6-6. Damage state versus impact energy. (a) Matrix damage. (b) Fiber cracks.

Figure 6-6 (b) shows the total length of fiber cracks produced in each panel obtained from optical measurements following thermal deply. For the back-face supported condition, fiber cracks were first detected at an impact energy of 4.7 J and the total crack length increased at a relatively constant rate up to a maximum total crack length between 60-90 mm at an impact energy of 14.2 J. For the edge-supported condition, fiber cracks were first detected at an impact energy of 7.1 J and the total crack length increased to a maximum value of between 30-40 mm at an impact energy of 14.2 J. Greater variability was observed in total fiber crack length measurements than matrix damage area measurements.

Considering results from both the delamination area and total length of fiber cracks presented in Figure 6-6 together provides an indication of the damage state produced for specific support conditions and impact energies. With the observation that minimal fiber damage occurs in the edge-supported condition for impact energies less than 7.5 J, it appears possible to produce significant matrix damage with minimal fiber damage using this support condition. However, since significant matrix damage area is produced using the back-face supported condition at impact energy of 4.7 J and above, it does not appear to be possible to produce significant fiber damage under any impact conditions investigated without significant matrix damage as well. Thus it was concluded that the two different damage states under investigation both had significant matrix damage, but one had minimal fiber damage whereas the other significant fiber damage.

6.2.2 Classification of Damage Types Using AE Signals

As an initial step towards interpreting the AE signals provided during impacting, impact force versus time curves were synchronized with raw AE signals. Figure 6-7 shows representative time-synchronized impact force and AE signal curves for the case of an elastic impact with no detectable damage and an impact producing detectable damage.
For both impact conditions, a strong AE signal is produced at the beginning of the impact

force curve. While a smooth loading curve is produced in the undamaged case shown in Figure 6-7 (a), a series of small force drops result from the impact damage created in Figure 6-7 (b). Corresponding to these load drops, additional high-amplitude AE signal peaks are produced. Comparing the time synchronized impact force and AE signal plots for the two impact events, it becomes clear that the AE signals positioned at the initial portion of the loading curves are produced by the impact event whereas the additional AE signal that is time-synchronized with the load drops in Figure 6-7 (b) are related to damage formation. Thus, the time-synchronization of load and AE signals permits the detection of specific features of the AE signals that are related to damage creation.

To further analyze the impact force curve as well as the AE signal in both the time and frequency domain, waterfall FFT plots were correlated with the load versus time plots. The waterfall FFT is a three-dimensional plot that displays frequency-characteristic changes over time. Figure 6-8 shows representative waterfall FFT plots corresponding to the three previously described damage types: undamaged, matrix damage, and fiber and matrix damage. Based on the sampling rates and the duration of the impact event, the time and frequency ranges for analysis were set at 0-10 ms and 1-600 kHz, respectively. Figure 6-8 (a), (b), and (c) provide a comparison of the initial AE caused by the impact and the subsequent AE resulting from damage creation across the entire frequency range. The undamaged specimen shown in Figure 6-8 (a) was impacted in the edge-supported condition using an impact energy of 3.6 J, conditions which did not produce any indications of matrix damage or fiber damage in the C-scan and thermal deply inspections. The smooth loading curve produced as well as the absence of any significant AE at the time of peak loading in Figure 6-8 (a) confirm that the impact did not produce damage. Additionally, the AE signals corresponding to the beginning of the impact force curve are observed at frequencies lower than 100 kHz. This result suggests that AE signals with frequencies lower than 100kHz cannot be used as a feature to classify damage creation or damage types.

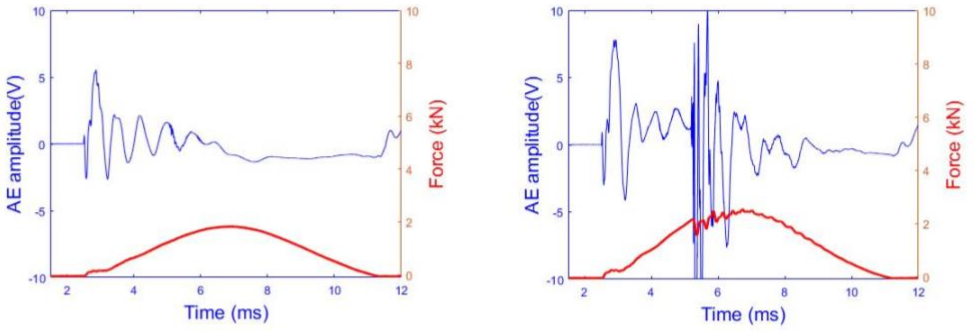

(a) (b)

Figure 6-7. AE signals and force curves. (a) Elastic impact with no detectable damage. (b) Impact producing detectable damage.

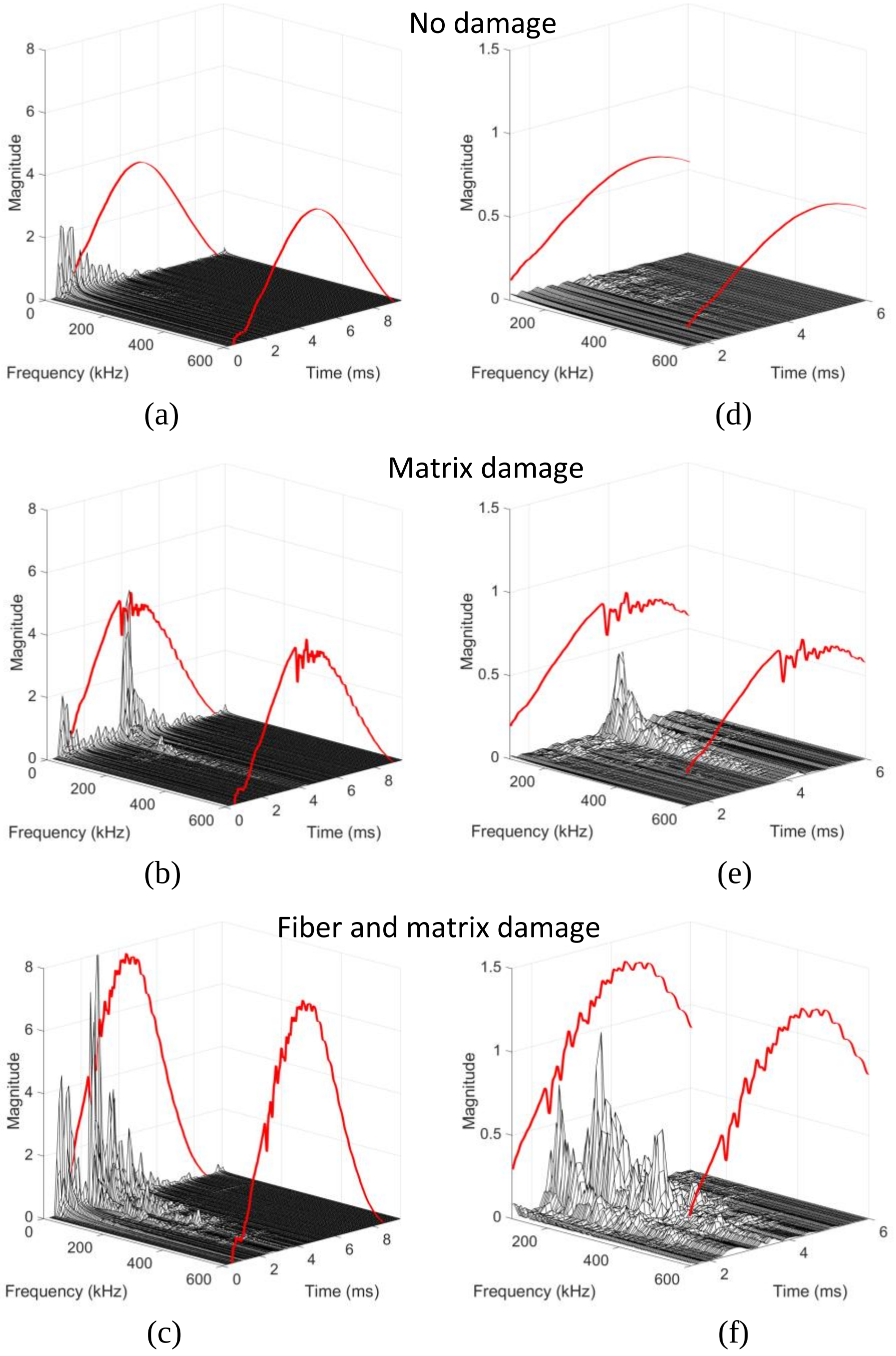

(a) (d)

(b) (e)

(c) (f)

Figure 6-8. Waterfall FFT correlated with force curves. (a) - (c) Full ranges (1 - 600 kHz, 0-9 ms), (d) - (f) Modified ranges (100 - 600 kHz, 1.5- 6 ms).

Figure 6-8 (b) shows the waterfall FFT plot from a matrix damage type specimen. The specimen was impacted in the edge-supported condition with an impact energy of 5.9 J, producing 326 mm^2 of matrix damage area and no detectible fiber damage. As expected, small load drops are visible in the peak region of the impact force curve. Corresponding to the load drops are additional high-amplitude AE signal peaks, including some AE at frequencies greater than 100 kHz that are believed to correspond to the formation of matrix damage.

The waterfall FFT plot shown in Figure 6-8 (c) was produced using the back-face supported condition and impacted with an impact energy of 14.2J, producing 756 mm^2 of matrix damage area and a 31 mm total length of fiber cracks. A series of load drops are observed during the specimen loading and through the peak region of the impact force curve. Corresponding AE signal peaks are produced, including those with significantly higher frequencies than exhibited in the matrix damage specimen of Figure 7b. These results suggest that both the occurrence of impact damage as well damage classification may be determined based on the frequency of AE signals produced during an impact event.

To further investigate damage detection and classification based on the frequency of received AE signals, the waterfall FFT plots for the three damage types were replotted using frequencies over 100 kHz, thus eliminating the AE signals believed to be produced by the impact event rather than damage formation. As shown in Figure 6-8 (d), the undamaged specimen showed no significant AE signals over 100 kHz. In contrast, both the matrix damage type specimen shown in Figure 6-8 (e) and the fiber and matrix damage specimen shown in Figure 6-8 (f) displayed significant AE signals over 100 kHz.

Closer examination of the potential for damage classification is possible using frequency domain views of these plots. For the matrix damage type specimen shown in Figure 6-8 (h), significant AE signal magnitude is observed between 100 - 200 kHz, and minimal magnitude is observed at higher frequencies. For the fiber and matrix damage specimen shown in Figure 6-8 (i), additional peaks of frequency magnitudes are observed between 200 - 500 kHz. Although the magnitudes of the frequency peaks above 200 kHz are smaller than those in the 100 - 200 kHz range that are believed to be produced by matrix damage, their presence only in the fiber and matrix damage specimen suggests that they may be used as an indicator of fiber damage during an impact. Overall, results obtained suggest that matrix damage corresponds to a frequency range of 100 - 200 kHz whereas fiber damage corresponds to a frequency range of 200 to 500 kHz. These results, suggesting that the AE frequency range produced by fiber damage is higher than the AE frequency range related to matrix damage during impacting, are in agreement with results from the literature [28, 29, 63-66] as shown previously in Figure 6-1.

6.2.3 Quantification of Damage Types

Once specific frequency ranges corresponding to each damage type were identified, information from the AE signals within each frequency range were further evaluated for use in establishing quantitative damage measures. Although the waterfall FFT plots correlated with impact force curves provide qualitative information for damage formation and classification, quantitative measures are desired for use in a SHM system. The use of a quantitative measure of damage classification reduces the need for experience on the part of inspectors, and allows for a less subjective determination.
In selecting a proper candidate method for AE signal quantification, the AE signals produced from the elastic impact must be identified and separated from those produced by damage formation in the composite material. The measured AE signals due to damage generally show an integrated wave packet, however the signals are composed of numerous AE signals produced by individual matrix cracks or fiber breakage.

While traveling from source to sensor, AE signals from individual damage events including fiber breakage could experience changes due to signal superposition or cancellation. Unlike an AE signal from an impact event itself, the collective AE signals from a collection of damage events may experience inconsistent variations of signal amplitudes. As a result, the power or energy of the signals that are typically used for signal quantification could produce inconsistent results. Note that these methods include square terms of amplitude, as given by

$$E_{\infty} = \sum_{n=-\infty}^{\infty} |x[n]|^2 \qquad (6\text{-}2)$$

$$P_{\infty} = \lim \underset{N\to\infty}{lim} \frac{1}{2N+1} \sum_{n=-N}^{N} |x[n]|^2 \,, \qquad (6\text{-}3)$$

for the case of n values $\{x_1, x_2, \ldots, x_n\}$.

In this investigation, the use of an enveloped area of the filtered AE signal was selected for damage state quantification due to its ability to properly convert the AE signal magnitudes to values without distortion due to peak amplitude effects. This enveloped area index is defined as

$$\mathrm{Index}_{envelope} = \sum_{i=1}^{i} \sqrt{\frac{1}{n}\left(x_{i+1}^2 + x_{i+2}^2 + \cdots + x_{i+n}^2\right)} \,, \qquad (6\text{-}4)$$

where sample number $i = 1,2,3\ldots i$, n is a window length.

Figure 6-9 presents an example of the enveloped area of the filtered AE signal. The raw signal shown in Figure 6-9 (a) was initially filtered. The filtered signal shown in Figure 6-9 (b) represents the net AE signals related to specific damage types. The envelope of the filtered signal, shown in Figure 6-9 (d), was calculated using the moving RMS envelope method using a window with a 10 samples length for each point of the envelope curve.

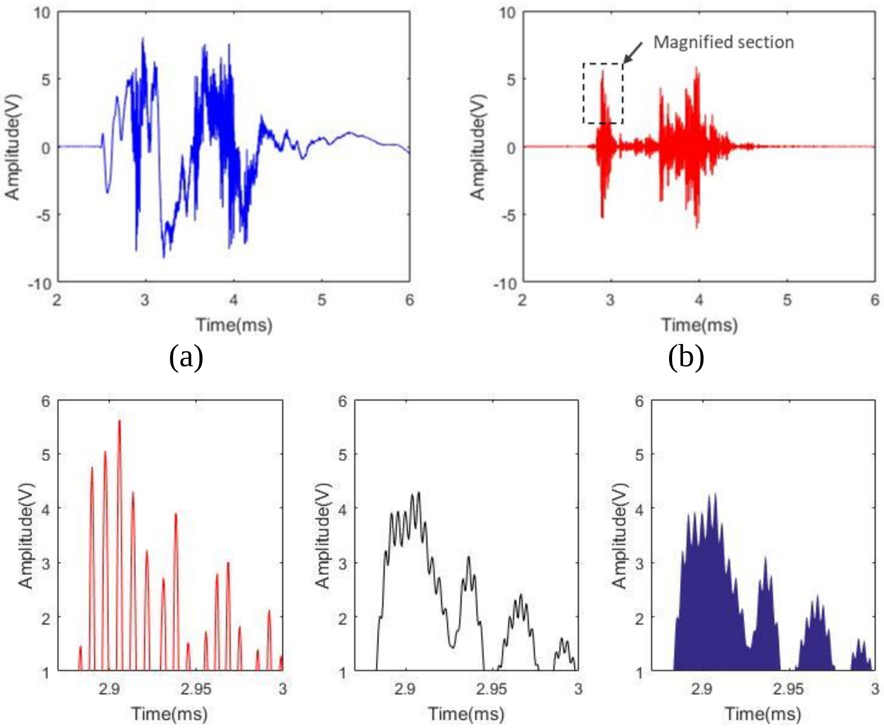

(a) (b)

(c) (d) (e)

Figure 6-9. Example of enveloped area of the filtered AE signal. (a) Raw signal. (b) Filtered signal. (c) Magnified filtered signal. (d) Envelope line. (e) Area under envelope.

Through the enveloping process, the effects of abnormal peaks or valleys in the wave can be reduced. The area under the envelope curve shown in Figure 6-9 (e) represents the quantified AE signals related to a specific damage type. Using this quantification method, two damage indices were calculated corresponding to matrix damage (100 – 200 kHz frequency range) and fiber damage (200-500 kHz frequency range). Additionally, the matrix damage index was investigated for use as an indicator of impact damage formation, since some level of matrix damage (delamination or matrix cracks) is produced in all damage-producing impacts.

Figure 6-10 shows the matrix damage index plotted as a function of the measured matrix damage area for all impacted panels. As expected, the undamaged specimens produced significantly lower matrix damage index values compared to specimens with measurable matrix damage areas. The horizontal dashed line shown in Figure 6-10 represents an estimated threshold value between undamaged and damaged specimens.

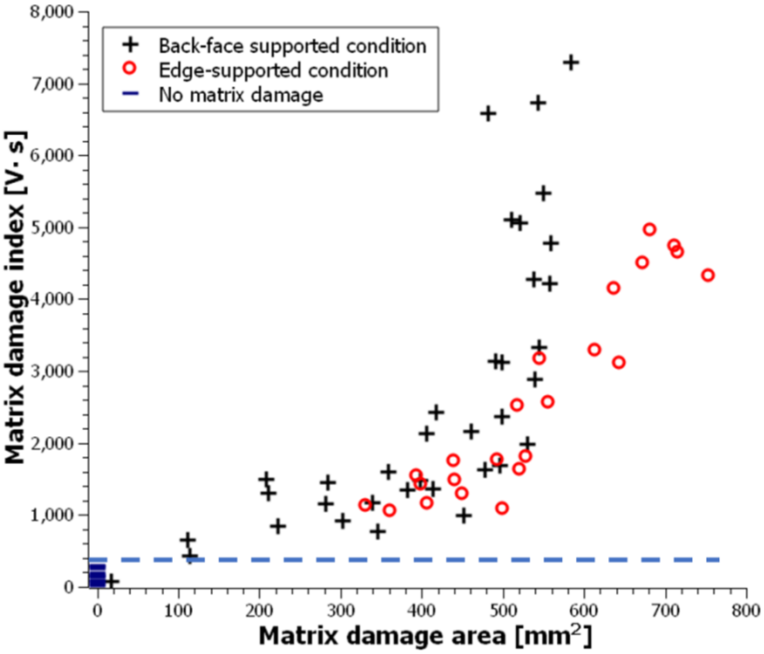

Figure 6-10. Matrix damage index for all impacted panels.

Above this damage threshold, higher matrix damage index values are produced from impacted panels with greater matrix damage areas. For matrix damage areas less than 500 mm^2, relatively small increases in the matrix damage index results from increasing matrix damage area for both back-face supported and edge supported impact conditions. For matrix damage areas greater than 500 mm^2, relatively large increases in matrix damage index are produced with relatively small increases in matrix damage area, especially for the back-face supported impacts. This finding suggests that some impacts with similar planar matrix damage areas produced a large range of matrix damage index values. A possible explanation is that the planar matrix damage areas from C-scan inspection do not account for multiple delaminations that may be produced through-the-thickness of the panel, especially from higher energy impacts.

Figure 6-11 shows the fiber breakage index plotted as a function of the total length of fiber cracks produced for all impacted panels. Similar to the matrix damage index, higher fiber breakage index values are produced from impacted panels with a greater total length of fiber cracks. For total fiber crack lengths up to 50 mm, increases in fiber breakage index result from increasing total fiber crack lengths. The highest values of fiber breakage index correspond with the greatest total length of fiber cracks, which were produced using the back face-supported impact conditions. In general, results show that a greater length of fiber cracks is required to produce the same fiber breakage index in the back-face supported panels than the edge supported panels. The shaded area shown in Figure 6-11 represents a transitional region between the undamaged and fiber damaged specimens. Unlike the matrix damage index, the fiber damage index does not show a clear distinction between undamaged and fiber damaged.

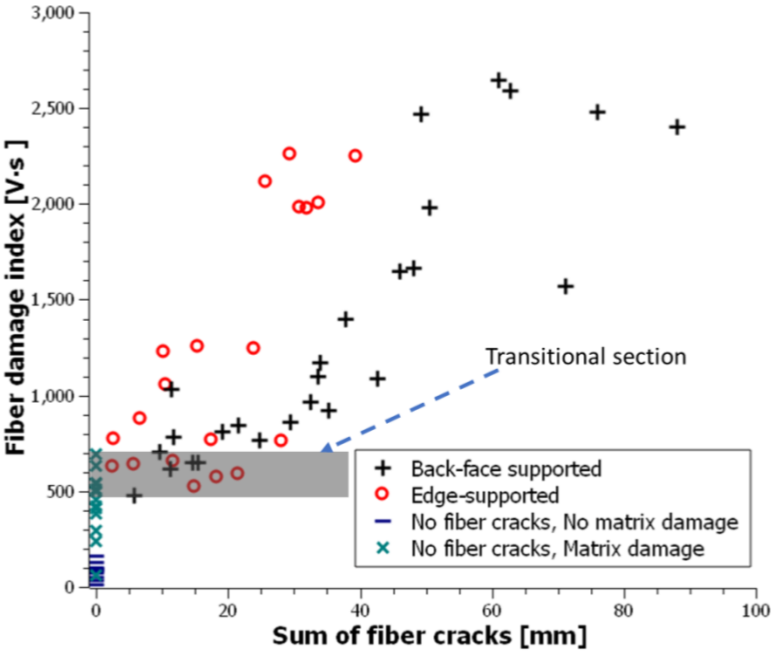

Figure 6-11. Fiber damage index for all impacted panels.

6.3 Summary and Conclusions

Through a process of testing, inspection, and analysis, an acoustic emission-based damage classification method was developed for use in identifying impact damage in composite panels. As an initial approach, three damage types were defined for impact tests and subsequent damage classification, considering applicable inspections methods and their usefulness in a SHM system. To produce targeted damage states with minimal changes in impact condition, back face-supported and edge-supported conditions were used during impacting. Using post-impact ultrasonic C-scan inspection and thermal-deply analysis, the edge-supported condition was determined to produce matrix damage including delamination with minimized fiber damage whereas the back-face supported condition tends to produce localized matrix damage with an increased amount of fiber damage. Waterfall-FFT plots correlated with the impact force curves were useful in identifying frequency ranges related to both matrix damage and fiber breakage. A frequency range of 100 – 200 kHz was identified for matrix damage whereas 200-500 kHz was identified for fiber damage, in agreement with previous research. Based on these frequency ranges for each damage type, a method for damage quantification was proposed, based on the enveloped area of the filtered AE signals. The proposed quantification method shows potential for damage state quantification; however development and analysis of the quantification method is suggested for use in future SHM systems.

7. EFFECTS OF GEOMETRICAL COMPLEXITIES

To date, much research on Lamb wave propagation has been performed experimentally, theoretically, and numerically. Numerical analysis using the finite element method (FEM) has been used to investigate wave propagation characteristics for use in NDI methods. As part of this research investigation, Lamb wave propagation was investigated in a thin composite plate using the finite element method. Results of the finite element simulations, especially arrival times and wave velocities were compared with predictions from the software code Disperse [53]. These analyses were used to assist in the development of impact location estimation algorithms which use the arrival time of the signals. Characteristics of Lamb waves due to changes in wave propagation directions are investigated in quasi-isotropic carbon/epoxy composite panels and numerical predictions are compared to experimental results. Finally, finite element analysis was performed to model wave propagation in plates with simple geometric discontinuities such as stiffeners and holes. Additionally, the structural health monitoring of larger structures leads to larger distances between sources of acoustic emissions and the sensors used for detection and issues associated with dispersion, and energy or amplitude reduction. In addition to numerical modeling, experimental approaches and signal analysis methods were used to assess the effects of geometrical complexities and large AE source to sensor distances in composite structures. To investigate changes in AE signals due to geometrical complexities, a series of steel ball drop tests as well as instrumented drop-weight impact testing were conducted on composite plates modified with a bonded stiffener or a through hole. To investigate changes in AE signals due to distance variations between impact source and AE sensors, a series of impact tests on a large composite cylinder barrel were performed. AE signals were analyzed in both the time and frequency domains to investigate changes in peak amplitude and signal-decay ratios.

7.1 Finite Element Model Development

Finite element modeling of Lamb wave propagation requires special consideration of the signal input method, including the window function types, central frequency, and appropriate time duration. Separate inputs can be used to investigate S_0 (Symmetric) and A_0 (Asymmetric) wave modes, but the modeling method used for excitation of each wave mode must be developed separately.

Although both time domain and frequency domain results can be used in NDI and SHM methods, time domain results are used in many impact location estimation algorithms. For finite element simulations, proper spatial and temporal sizes are important for obtaining accurate and efficient results using explicit dynamic methods. For finite element modeling of wave propagation, the required element length and time steps of wave propagation analysis using explicit finite element methods are given by [67]

$$L_e = \frac{\lambda_{min}}{20}, \tag{7-1}$$

where L_e and λ_{min} are the recommended element length and minimum wave length, respectively, and

$$\Delta t = \frac{1}{20 f_{max}}, \tag{7-2}$$

where Δt and f_{max} are the recommended time step and maximum frequency, respectively.

The material model and element type selection used in the analysis can have a significant effect on results. The elastic properties of the composite material, including the interlaminar properties must be known, and the layer stacking sequence needs to be considered. For modeling composite laminates, the selection of the material model and the element type are related, as layer homogenization may be used, or individual layers may be modeled with separate elements. The size and shape of the modeled region may affect these considerations.

In this study, the commercial finite element code ANSYS [54] was used to investigate Lamb wave propagation in composite plates. The initial focus of the analysis was to investigate the velocities of each wave mode. Figure 7-1 shows the modeling method used. Quarter-symmetry boundary conditions were applied to the front and left edges of the modeled region and far-field displacements were applied at the left edge to simulate pinned supports. The in-plane dimensions of the modeled region were 400 mm x 5mm, with a thickness of 2.3 mm. The element size was 0.285 mm, the thickness of each layer of the composite laminate. Each layer of the 8-layer [0/45/90/-45]s carbon/epoxy composite laminate was meshed with eight-node brick-type elements. To produce the correct properties corresponding to the fiber orientation in each layer, the elastic properties were transformed prior to inputting in the global model coordinate system. The orthotropic material properties used for the carbon/epoxy composite material were the same as presented previously in Table 7-1.

The input signal used, a 200 kHz five-cycle tone burst signal with a 25 μsec duration, was selected to avoid higher S and A wave modes. A time step size of 0.0625 μsec (corresponding to 16 MHz) was used, which permits a total of 80 samples per cycle. The input signal was modeled as an applied displacement condition to produce the same input amplitude regardless of model type, material, and boundary conditions. As shown in Figure 7-1, in-plane and out-of-plane input signals were modeled separately. In both cases, the prescribed displacements were applied to all nodes at the left cross-sectional area of the model, producing wave propagation along the long axis of the modeled region without reflections from the side wall surfaces. In an effort to reduce the mesh size, both models used symmetry conditions along the two side walls. For the model with the A mode input, an additional symmetry boundary condition was applied at the left cross-sectional area. Attenuation was not considered in the finite- element analyses.

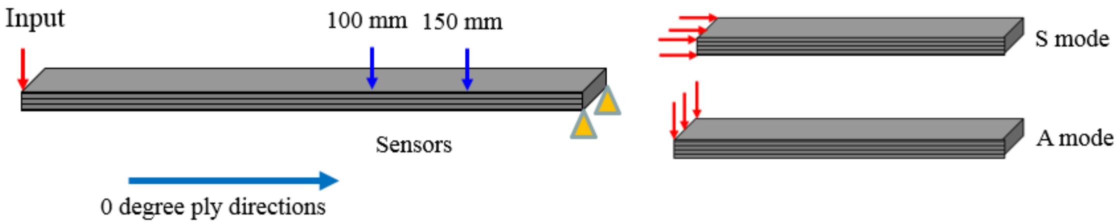

Figure 7-1. Finite element modeling method for wave velocity investigation.

Figure 7-2 shows the S_0 and A_0 mode responses measured at a distance of 100 mm from the source signal. These results show that both the A_0 and S_0 wave mode signals have similar amplitudes as the input signal, which has a displacement amplitude of ± 1 µm. At this relatively short distance, the S_0 mode signal shows relatively greater wave shape distortion than the A_0 mode. Such wave distortion, as well as dispersion, makes the calculation of wave velocity difficult. In this investigation, the group velocity for each wave mode was determined by counting wave numbers and locating peak amplitudes at both input and receiving signal.

The commercial software code Disperse [53] was used to obtain Lamb wave velocities for the S_0 and A_0 modes and to investigate higher modes of Lamb wave propagation. Since attenuation was not considered in the finite element analyses, an attenuation factor was not included in the Disperse modeling. Table 7-1 provides a comparison between finite element and the Disperse code predictions of group velocities at two different distances from the input location: 100 mm and 150 mm. Good agreement is observed between the two methods, with maximum differences of 3% and 8% for the S_0 and A_0 modes, respectively.

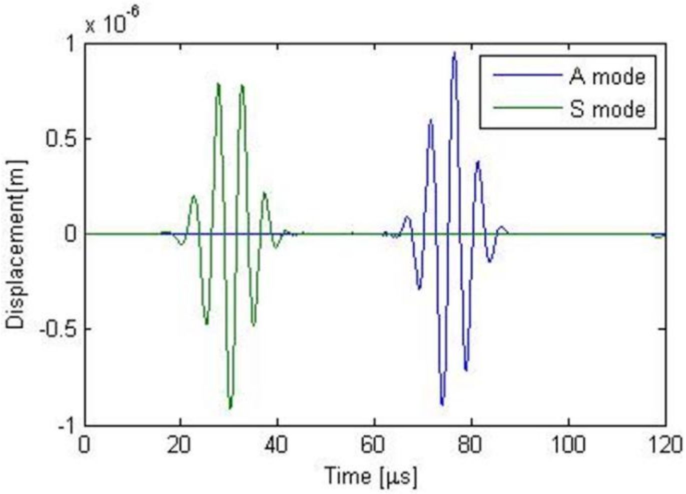

Figure 7-2. Displacement response of S_0 and A_0 wave mode at 100 mm from source signal.

Table 7-1. S and A Mode Wave Group Velocity Comparison

Mode	FEM (mm/μsec)		Disperse (mm/μsec)
	100 mm	150 mm	
S mode	6.06	6.06	6.22
A mode	1.60	1.57	1.71

7.2 Lamb Wave Propagation in Composite Plates: Directional Dependence

Some impact location estimation algorithms for SHM require time-of-arrival information from the first wave packet at each sensor location. In such cases, the differences between theoretical and actual measurements can be significant sources of error in impact location estimation. For anisotropic materials, such as composite materials, wave velocity is expected to be directionally dependent, since the phase velocity of wave propagation is dependent on the material stiffness. In composite laminates, layers of orthotropic material are typically stacked with different fiber orientations, producing effective laminate stiffnesses that are direction dependent. Of particular interest in this investigation is whether the effective homogenized laminate stiffness in a particular direction prescribes the wave velocity, or whether the individual layer stiffnesses and through-the-thickness placement of specific layers also play a role in the wave velocity.

To investigate these effects, an eight-layer $[0/45/90/-45]_S$ quasi-isotropic composite laminate was considered. Since quasi-isotropic laminates have the same effective stiffness properties in all in-plane directions, they may not be expected to have any directional dependence on wave velocity. However, the stiffness of the surface layer as well as the other layers of the laminate will vary with orientation. For example, the $[0/45/90/-45]_S$ quasi-isotropic laminate effectively becomes a $[90/-45-0/45]_S$ laminate when wave propagation shifts from the 0° to 90 ° direction.

Both experiments and finite element analyses were performed to investigate the directional dependence of the S_0 mode Lamb wave velocity. Finite element analyses were performed using the models described above for wave mode velocity comparisons. A 1.2 m square carbon/epoxy composite panel was fabricated for the experiments and Vallen System 900-RIC AE sensors [49] were used for both producing the excitation signal and for receiving the signal. As shown in Figure 7-3, a template was used to maintain a fixed distance of either 127 mm or 229 mm between the source and receiving sensors.

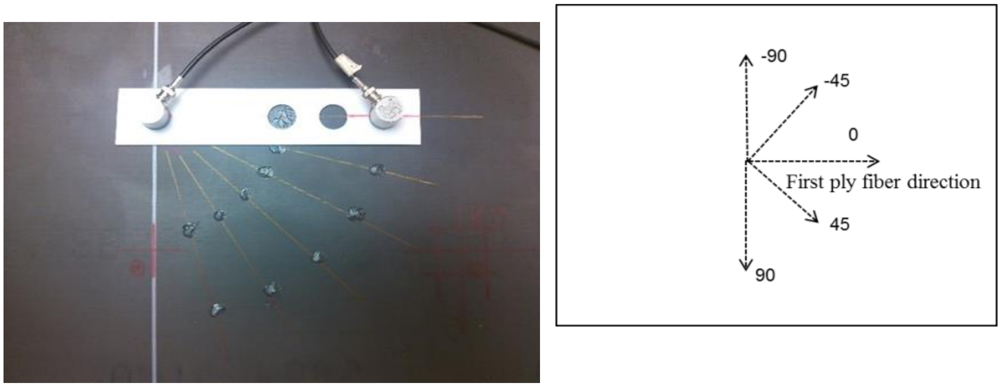

(a) (b)

Figure 7-3. Experiment configuration for directional dependence on quasi-isotropic lay-up. (a) Use of template for arrival time measurement. (b) Angle measurement.

A National Instruments PXIe-7073 32 channel data acquisition system with a 2 MHz sampling rate and 14 bits/sample resolution in each channel was used. The active experiment was performed with the receiving signal rotated in 15º increments from 0º to ±90º relative to the top layer fiber orientation. A total of twenty tests were performed and averaged for each receiving sensor position. The wave velocities were calculated from the travel time and the distance between the two sensor positions (102 mm). Experimental results suggest that a small directional difference in wave velocity is present in the quasi-isotropic composite panel, with the lowest wave velocities at wave propagation angles closer to the fiber orientation of the surface ply (0º). However, the relatively short distance used for velocity measurement limits their accuracy. Follow-on experiments with longer measurement distances are planned to improve measurement accuracy. Finite element results also suggest some directional dependence of wave velocity, with the highest wave velocities predicted at wave propagation directions transverse to the fiber orientation of the surface ply (0º).

Table 7-2 lists the measured and calculated travel times and calculated S_0 wave velocities for wave propagation directions ranging over 180º. Additionally, it is noted that the measured 0º wave velocity (6.16 mm/µsec) is in good agreement with finite element (6.20 mm/ µsec) and Disperse code (6.46mm/ µsec) predictions using a 150 kHz frequency condition.

Table 7-2. S_0 Wave Propagation Angle Effect on Travel Time and Velocity

Propagation angle	**Travel time of 102 mm (μsec)**		**Velocity(mm/μsec)**	
(degrees)	**Experiment**	**Finite element**	**Experiment**	**Finite element**
-75	15.50	16.13	6.55	6.30
-60	15.50	16.13	6.55	6.30
-45	16.50	16.26	6.16	6.25
-30	16.50	17.37	6.16	5.85
-15	16.50	17.50	6.16	5.81
0	16.50	16.38	6.16	6.20
15	16.00	19.13	6.35	5.31
30	16.50	20.50	6.16	4.96
45	16.00	16.25	6.35	6.25
60	16.00	16.25	6.35	6.25
75	16.00	16.13	6.35	6.30
90	16.00	15.78	6.35	6.44

7.3 Analysis of Lamb Wave Propagation Associated with Geometrical Complexity

7.3.1 Effects of Cutouts on Lamb Wave Propagation

Additional finite element analyses were performed to investigate the effects of geometric variations on Lamb wave propagation in composite panels. Since cutouts, build-ups, and thickness transitions are common in composite structures for which SHM is of interest, an understanding of the effects of such geometric variations on Lamb wave propagation is desired. Circular cutouts in composite structures are perhaps the most common type of geometric discontinuity, and are the focus of the current investigation. While this initial investigation is more fundamental in nature, follow-on analysis and experimentation is intended to assist with the development of SHM algorithms for estimating impact locations as well as designing the placement of AE sensors on actual composite structures.

To investigate the effects of circular cutouts in composite panels on Lamb wave generation, the finite element model shown schematically in Figure 7-4 was developed. By using two symmetry boundary conditions, only one-fourth of the panel was modeled. The input signal was applied at the corner of the modeled region, representing the center of the panel. Two circular holes, 25 mm and 50 mm in diameter, were modeled at a distance of 200 mm from the signal input. Additionally, two simulated sensor positions were located 350 mm and 400 mm beyond the circular hole location, as shown in Figure 7-4 (a). The placements of the hole and sensor locations relative to the input signal were selected to produce sufficient time separation of the initial arriving modes (S_0 and A_0) to allow for the identification of waveform disturbances and reflections produced from the circular cutout. Similarly, the overall model dimensions of 600 mm x 400 mm were selected to prevent boundary reflections from arriving at the sensor locations during the arrival time of the initial wave modes.

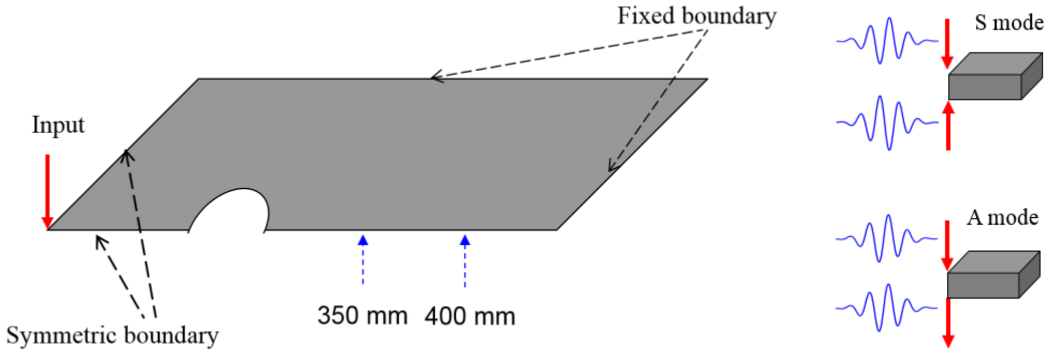

(a)
(b)

(b)

Figure 7-4. Schematics of finite element model for cutout shape and dual point- input method. (a) Schematics of finite element model. (b) Point-input method.

Due to the relatively large size of the required modeled region, efforts were made to reduce the mesh refinement, particularly in the thickness direction of the panel, and thus reduce computational cost. Since, in most cases, the element size associated with modeling the individual layers of the composite laminate were smaller than the recommended element size given in Equation 7-1, effective homogenized laminate properties were generated using laminated plate theory [68]. The modeled region was meshed with higher-order 20-node brick type elements, with three nodes per element edge to improve out-of-plane displacement results. The mesh density of the homogenized, orthotropic composite laminate was selected to minimize computational costs while maintaining model accuracy. With these simplifications, the resulting model had similar computational costs to the layer-by-layer strip model described in the previous section. For the case of no cutout, the wave velocities of the S_0 and A_0 modes were calculated as 6.29 (mm/µsec) and 1.78 (mm/µsec), respectively, in good agreement with results from the Disperse code presented in Table 7-1. Thus, this homogenized laminate modeling approach was determined to be suitable for investigating the effects of cut-outs on Lamb wave propagation, while recognizing that any directional differences in wave velocity and localized ply-level effects could not be investigated.

Similar to the previous analysis, 200 kHz five-cycle tone burst input signals were input as prescribed displacements. Separate inputs were applied in an attempt to excite and focus individually on either the S_0 or A_0 wave mode. As shown in Figure 7-4 (b), the displacements were applied at a set of two surface node points at the center of the panel. For the S mode input, the same displacement input was applied at the top and bottom surfaces of the panel. For the A mode input, the same signal magnitudes were applied at the two surfaces, but in opposite directions.

Table 7-3 lists the arrival times of the S_0 and A_0 wave modes at the two simulated sensor positions (350 mm and 400 mm) for the two cutout diameters investigated (25 mm and 50 mm), as well as the case of no cutout. Additionally, the time delays due to each hole size are shown. These results suggest that there are no simple, linear relationships between arrival time and hole size.

Figure 7-5 shows the S_0 wave mode response at a distance of 400 mm from the hole. Results from analyses of both the 25 mm and 50 mm hole diameters are shown, as well as the case of no hole for comparison purposes. Comparing the peak displacements occurring between 77 and 79 µs, these results suggest that the presence of the cutout affects both the received signal amplitude and arrival time. However, neither of these effects appear to be linearly related to hole size.

7.3.2 Effects of Stiffeners on Lamb Wave Propagation

Additionally, to investigate the effects of stiffeners on Lamb wave generation in composite panels, the finite-element model shown schematically in Figure 7-6 was developed. The same finite element modeling methods were used as shown previously in Figure 7-1; however, additional build-up geometries were modeled and analyzed to evaluate the effect of the build-up width and height on signal propagation. By using two symmetry boundary conditions, only half of the panel was modeled. The input signal was applied at the corner of the modeled region.

Table 7-3. Arrival Times of S_0 and A_0 Modes With Circular Cutouts

Wave Mode	**Distance From Source (mm)**	**Cutout Diameter**			**Time delay due to hole (µsec)**	
		No Cutout	**25 mm**	**50 mm**	**25 mm**	**50 mm**
S_0	350	55.8	56.5	58.0	0.75	2.25
	400	63.6	64.3	65.8	0.62	2.12
A_0	350	196.2	197.7	200.9	1.45	4.65
	400	223.4	224.7	227.4	1.30	4.00

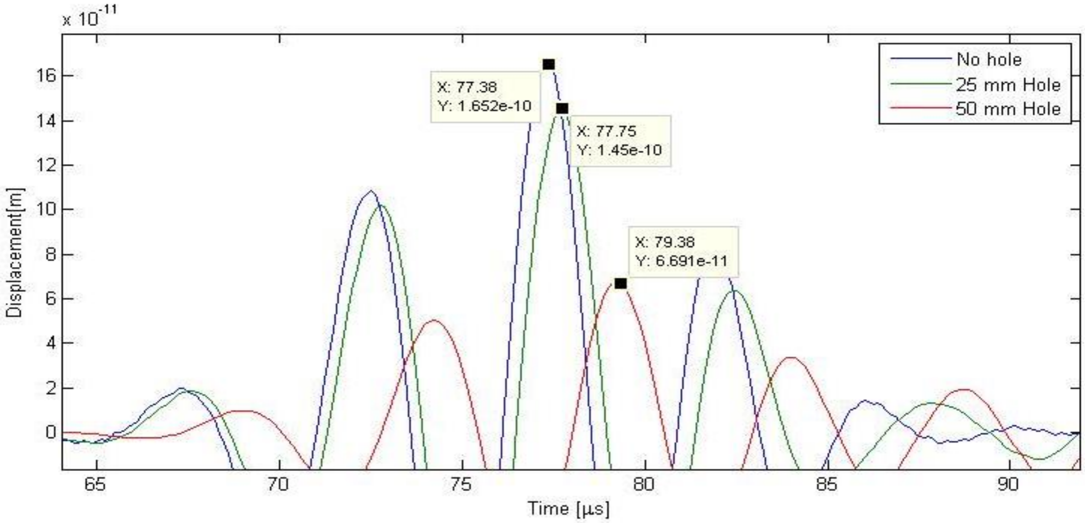

Figure 7-5. Effect of circular cutout on S_0 mode response, 400 mm from source signal.

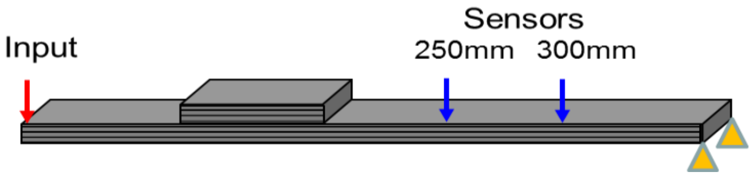

Figure 7-6. Schematics of finite element model for stiffener shape.

Example time domain response plots for build-ups with different thicknesses and widths are shown in Figure 7-7. The results show that changes in the build-up thickness and width can cause wave distortion as well as velocity changes. Amplitude reduction and wave distortion due to thickness changes were noticeable in Figure 7-7 (a), which provides a comparison of thickness variations. However, the arrival-time delay due to wave velocity changes was a noticeable change in Figure 7-7 (b), which provides a comparison of stiffener-width variations. Because the wave distortion caused by both thickness and width changes of the stiffener were very complex, further investigation with diverse conditions in the size and shape of stiffeners is recommend in order to characterize the effects of each condition change.

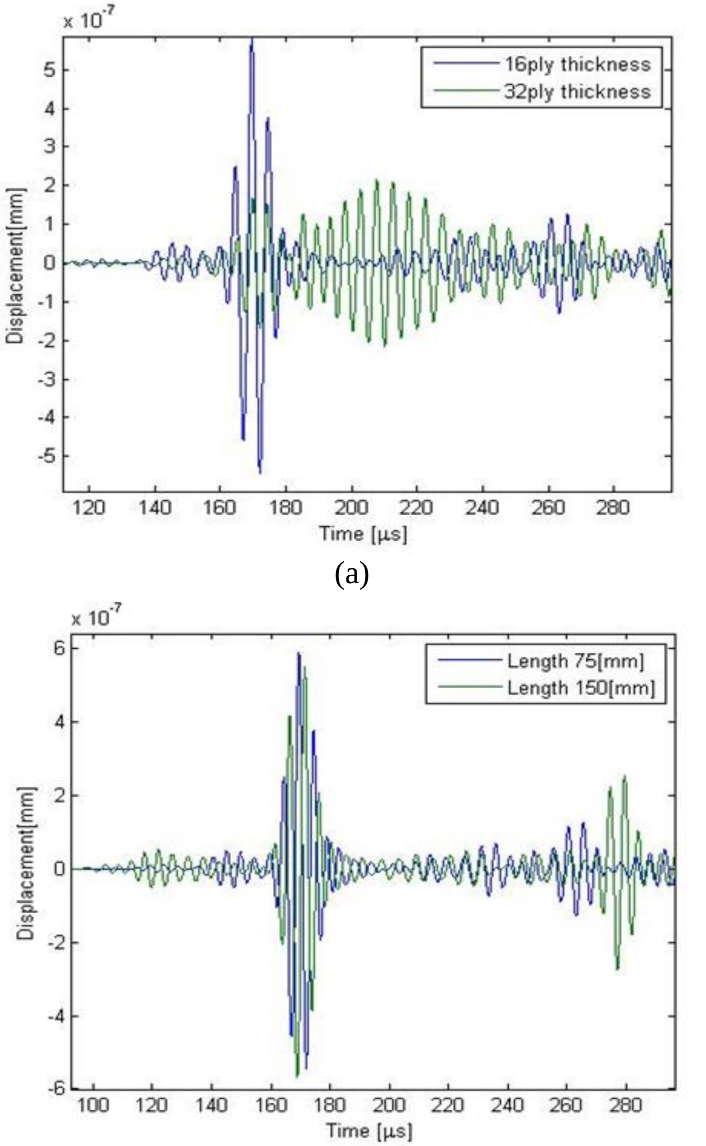

(a)

(b)

Figure 7-7. Effect of a stiffener located 300 mm from source signal. (a) Thickness change. (b) Stiffener-length change.

7.4 Experimental Analysis of Geometrical Complexity

Two types of geometrical complexities were selected as representative of those commonly found in composite structures: a through hole and a flat stiffener. Both were investigated using 500 mm × 125 mm flat quasi-isotropic composite panels fabricated using Hexcel IM7/8552 unidirectional prepreg tape. The hole diameter and stiffener height and width were determined using results of previously conducted numerical analyses and passive AE tests. The diameter of the machined hole was 51 mm and was positioned as shown in Figure 7-8. The cross sectional dimensions of the stiffener were 25 mm in width and 10 mm in height. The stiffener was fabricated of unidirectional carbon/epoxy composite and was secondarily bonded to the composite plate using a room temperature curing epoxy. A total of six STEMiNC Piezo Disc 5x0.4mm 450 kHz sensors were bonded along the length of the panel as shown in Figure 7-8. The position of the steel ball drop was located near the end of the panel, such that AE signals produced would be received by AE sensors both before and after encountering the geometric complexity.

A National Instruments PXIe-1073 Data Acquisition System, which has 2MHz sampling rates, was used for AE signal recording. Force measurements collected from the impactor were also recorded when instrumented drop-weight impact testing was performed.

A series of steel-ball drop tests were performed initially, which do not produce damage to the composite panels. As with pencil-lead breakage (PLB), which is considered as a reproducible artificial AE source [69], steel-ball drop tests can create a reproducible AE signal with higher AE energy than produced using PLB.

A total of 20 steel ball drop tests were conducted on each plate before either machining a through hole or bonding of a stiffener, after which 20 additional steel ball drop tests were conducted. The peak-to-peak amplitudes of AE signals from individual tests were normalized, and the normalized amplitude ratios of the 20 tests were averaged.

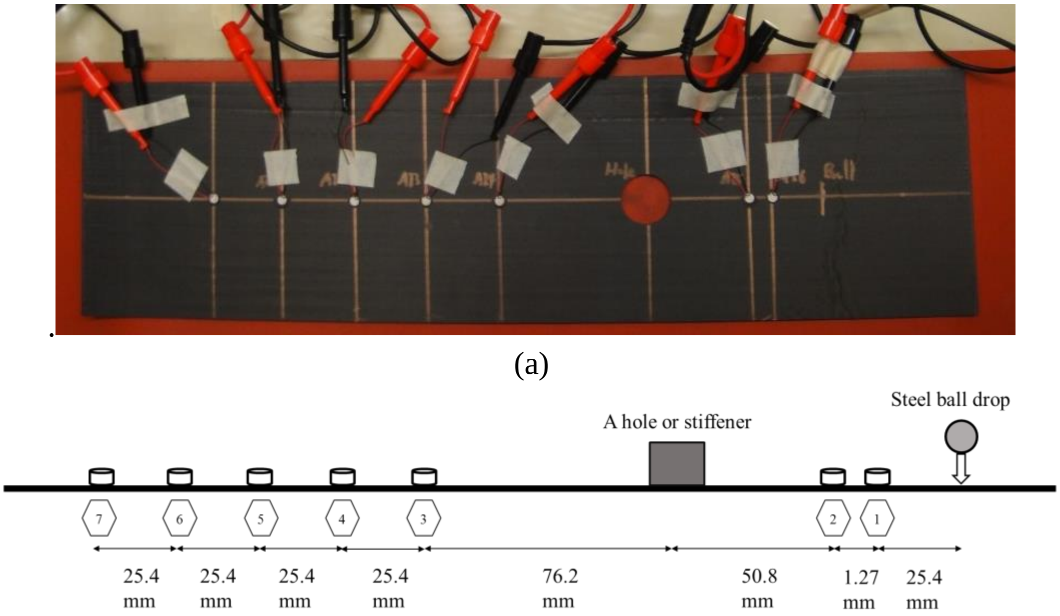

(a)

(b)

Figure 7-8. Locations of sensors for steel ball drop tests. (a) Test configuration for a specimen with hole. (b) Locations of sensors and excitations.

For instrumented impact testing, an Instron 4088, an instrumented drop-weight impact machine was used. These impact tests were intended to produce AE signals related to different types of damage and with frequency components in a wide-frequency range. The impact energy levels used were varied to produce matrix-related damage and fiber breakage. Considering the signal strength and the frequency ranges of the AE signal due to impact, two STEMiNC Piezo Disc 7x0.5mm R sensors with a resonance frequency of 4.25MHz were installed 100 mm from each end of the plate. A back-face support condition was used in which a 3.8 mm-thick silicon rubber pad was placed between the test panel and the impactor base as shown in Figure 7-9. In addition to investigating the two geometrical complexities discussed above, changes to the type of carbon/epoxy composite material, ply lay-up, and panel thickness were also investigated.

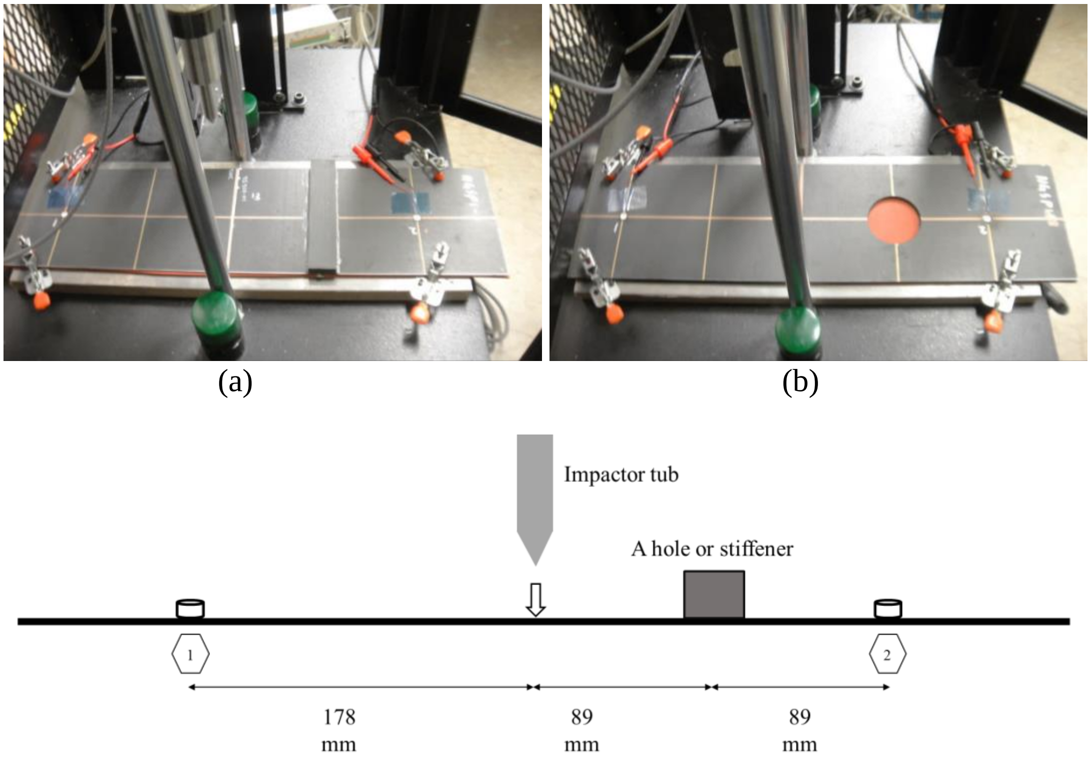

(a) (b)

(c)

Figure 7-9. Locations of sensors and geometrical complexity used for drop-weight impacting. (a) A stiffener-added specimen. (b) A hole-added specimen (c) Dimensions of specimens.

Table 7-4 summarizes the test conditions used for drop weight impact testing. Both IM7/8551 and AS4/3501-6 unidirectional carbon/epoxy prepreg materials were used to produce the material variations. A [0/45/90/-45]$_{2S}$ quasi-isotropic lay-up and [0/90]$_{4S}$ symmetric cross-ply lay-up were used for the two lay-up sequences. The two panel thicknesses used were 2.4 and 4.8 mm, obtained by doubling the number of plies of prepreg material used in each layer. Figure 602 and Table 7-4 represent the configuration of sensors for geometrical complexity, and facesheet configurations for machine impacting, respectively.

Table 7-4. Test Conditions Used For Drop Weight Impacting

Case ID	Materials	Lay-ups	Thickness (mm)	Geometrical complexity	Features
1	IM7/8551	$[0/45/90/-45]_{2S}$	2.4	Stiffener	Reference
2	AS4/3501	$[0/45/90/-45]_{2S}$	2.1	Stiffener	Materials
3	IM7/8551	$[0/90]_{4S}$	2.4	Stiffener	Lay-ups
4	IM7/8551	$[0/45/90/-45]_{4S}$	4.8	Stiffener	Thickness
5	IM7/8551	$[0/45/90/-45]_{2S}$	2.4	Hole	Reference
6	AS4/3501	$[0/45/90/-45]_{2S}$	2.1	Hole	Materials
7	IM7/8551	$[0/90]_{4S}$	2.4	Hole	Lay-ups
8	IM7/8551	$[0/45/90/-45]_{4S}$	4.8	Hole	Thickness

Figure 7-10 presents measured AE signals from steel ball drop testing performed both before and after the addition of a bonded stiffener. Measurements from three AE sensors, labeled 2, 4, and 6 in Figure 7-8 (b), were used to investigate signal changes due to the stiffener. The AE signals shown from Sensor 2, shown in Figure 7-10 (a) and (d) show similarities in the amplitude and shape before and after the stiffener installation. This result was expected, as sensor 6 is positioned on the same side of the stiffener as the steel ball drop location. However, AE signals from Sensor 4, shown in Figure 7-10 (b) to (e), display a reduction in peak amplitude following the addition of the stiffener. Additionally, the lower frequency components shown in the shaded area of Figure 7-10 (b) and (e) are affected more than high frequency components. Comparing the shape and amplitude of the AE signal in these two plots after a time of 3 ms, which is composed low frequency reflections, more prominent amplitude reduction is observed than signals before 3 ms, which include higher frequency components. Similarly, the AE response from Sensor 2 before and after stiffener addition, shown in Figure 7-10 (a) and (d), also showed similarities in both signal amplitude and shape.

Figure 7-11 compares measured AE signals from steel ball drop testing performed both before and after the addition of a through hole in each panel. Unlike the results for a bonded stiffener shown in Figure 7-10, no significant reductions in peak signal amplitude were observed at any of the sensor locations due to the addition of the 51 mm diameter hole. This finding suggests that the low frequency component of the AE signal is not affected significantly by the presence of the hole. However, some sensors showed a signal amplification, as shown in the shaded boxes within Figure 7-11 (b) and (e). This signal amplification may result from superposition of reflected waves due to geometry change. Additionally, a comparison of the AE signals shown from Sensor 6, shown in Figure 7-11 (c) and (f) suggests that relatively high frequency components were reduced by the addition of the hole.

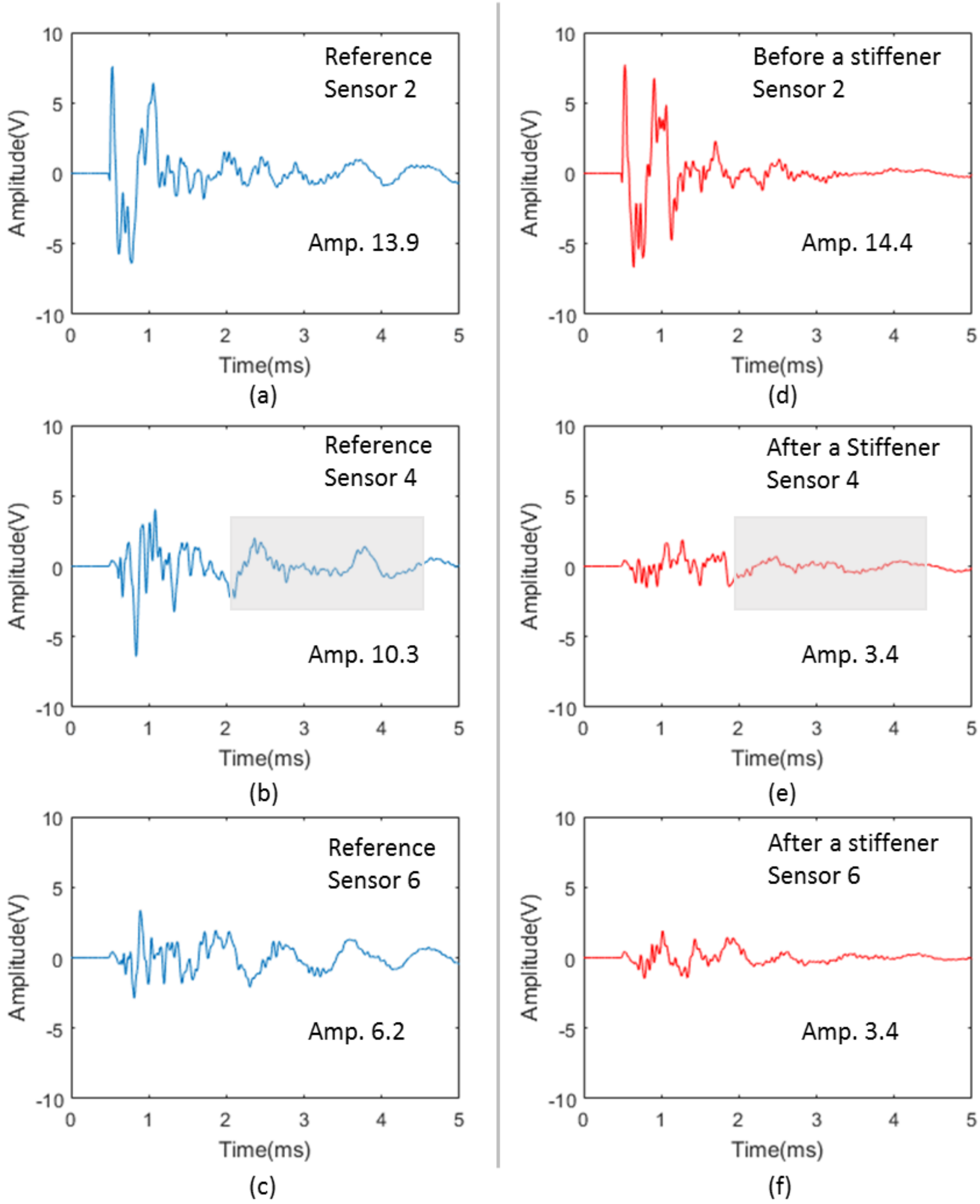

Figure 7-10. Time domain response before and after adding a stiffener. (a), (b), (c) Before stiffener bonding. (d), (e), (f) After stiffener bonding.

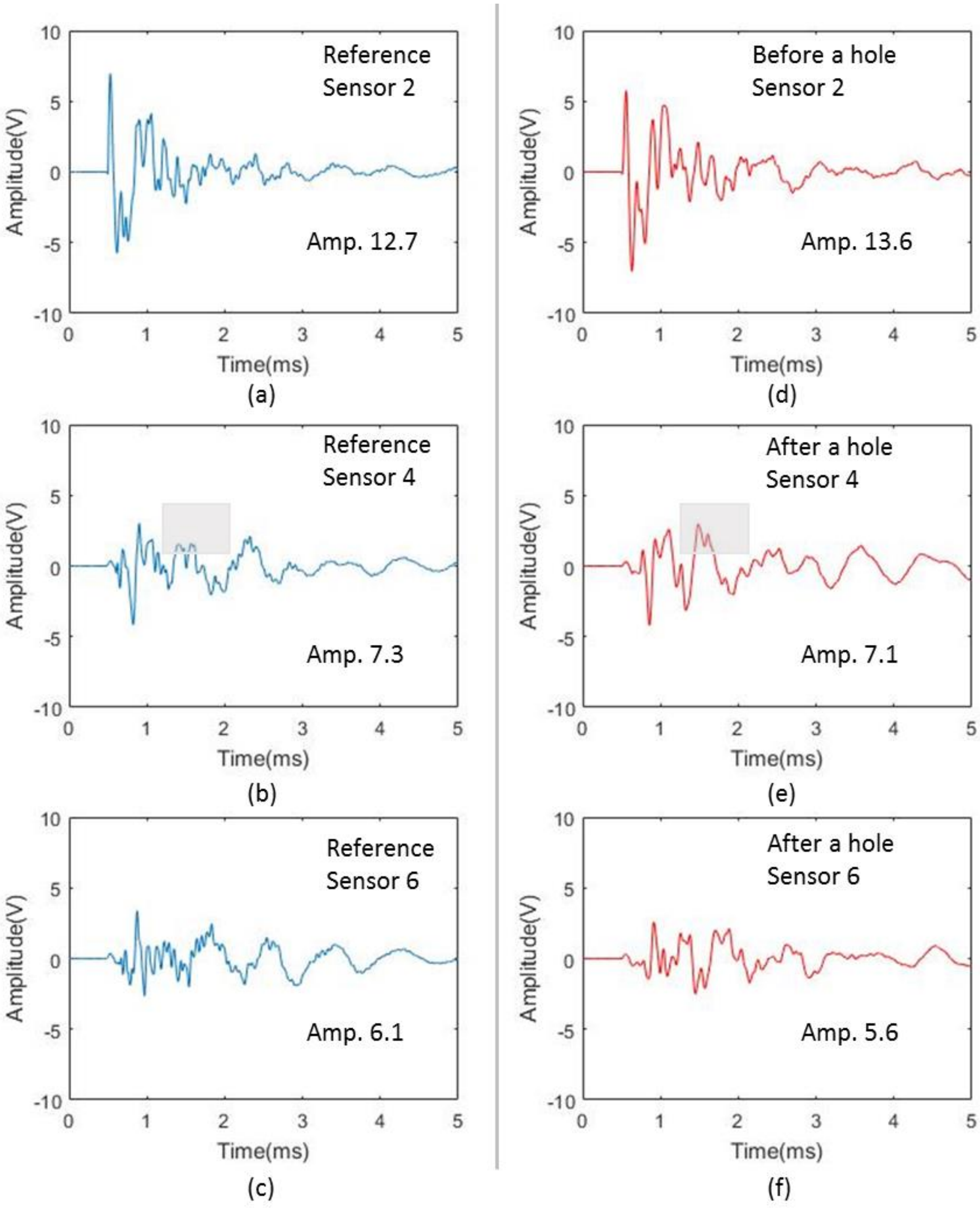

Figure 7-11. Time domain response before and after adding a hole. (a), (b), (c) Before hole cutting. (d), (e), (f) After hole cutting.

In summary, the AE sensor signals shown in Figure 7-10 and Figure 7-11 for an added stiffener and through hole, respectively, display different trends due to the addition of the two different geometrical complexities. Further investigation is required before it will be possible to generalize the results since the AE signal frequency range is limited to a few kHz, which is within the sonic region, and the different types of geometric variations cannot be directly compared.

Figure 7-12 shows the normalized and averaged AE signal amplitudes for the case of the added stiffener. The results show a significant reduction in AE signal amplitudes due to the addition of the bonded stiffener. The stiffener appears to act as an AE signal damper since all of the reflected signals, both backward as well as forward, showed a peak amplitude reduction.

Figure 7-13 shows the normalized and averaged AE signal amplitudes for the case of the through hole. A noticeable difference from the case of an added stiffener (Figure 7-12) is the absence of a significant peak amplitude reduction produced by the addition of the hole. This result suggests that for the case of the 51 mm central hole, pathways remain along either edge of the panel for unaffected wave propagation. In contrast, the bonded stiffener extended across the entire width of the panel producing de-amplification and energy absorption.

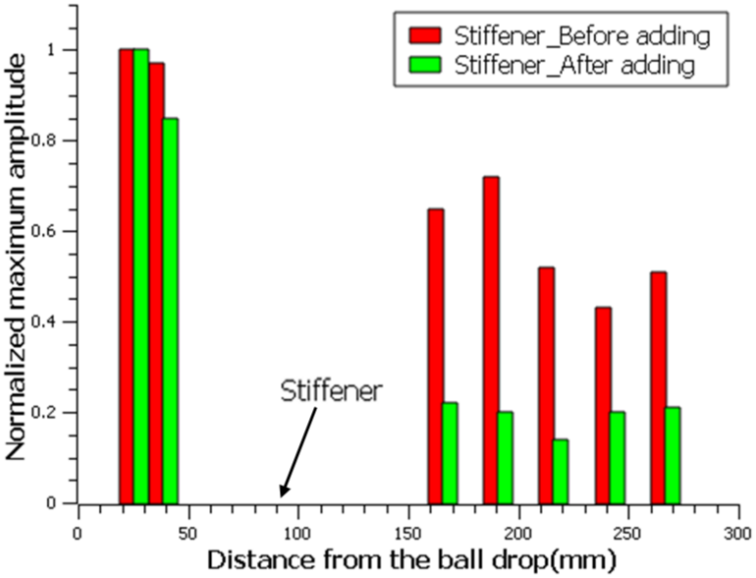

Figure 7-12. Normalized maximum amplitude change by an added stiffener.

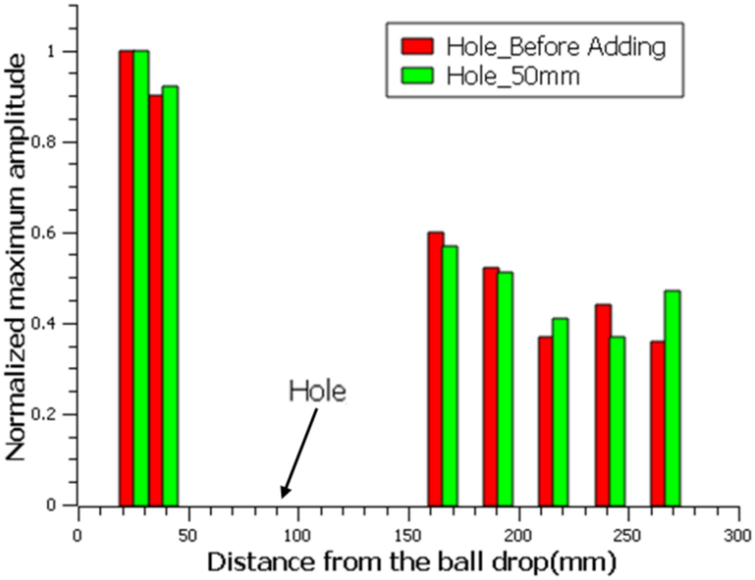

Figure 7-13. Normalized maximum amplitude change produced by a through hole.

Figure 7-14 shows the measured AE signals as well as waterfall FFTs with time-coordinated force curves resulting from instrumented drop-weight impact testing on a composite plate with and without a bonded stiffener. Reductions in signal amplitude due to the addition of the stiffener are observed by comparing the AE signals of Figure 7-14 (a) and (c). In addition to the wave amplitude reduction in the peak signals that were received in the 3 to 5 ms range, additional larger signal reductions were produced in the initial wave packet located in 2 to 3ms range. Because the first arriving wave packet is often used for impact location estimation, an amplitude reduction in this first wave packet due to this type of geometric discontinuity is of some concern. The wave amplitude reduction can also be observed in the overall frequency range through a comparison of the two waterfall FFT plots shown in Figure 7-14 (b) and (d).

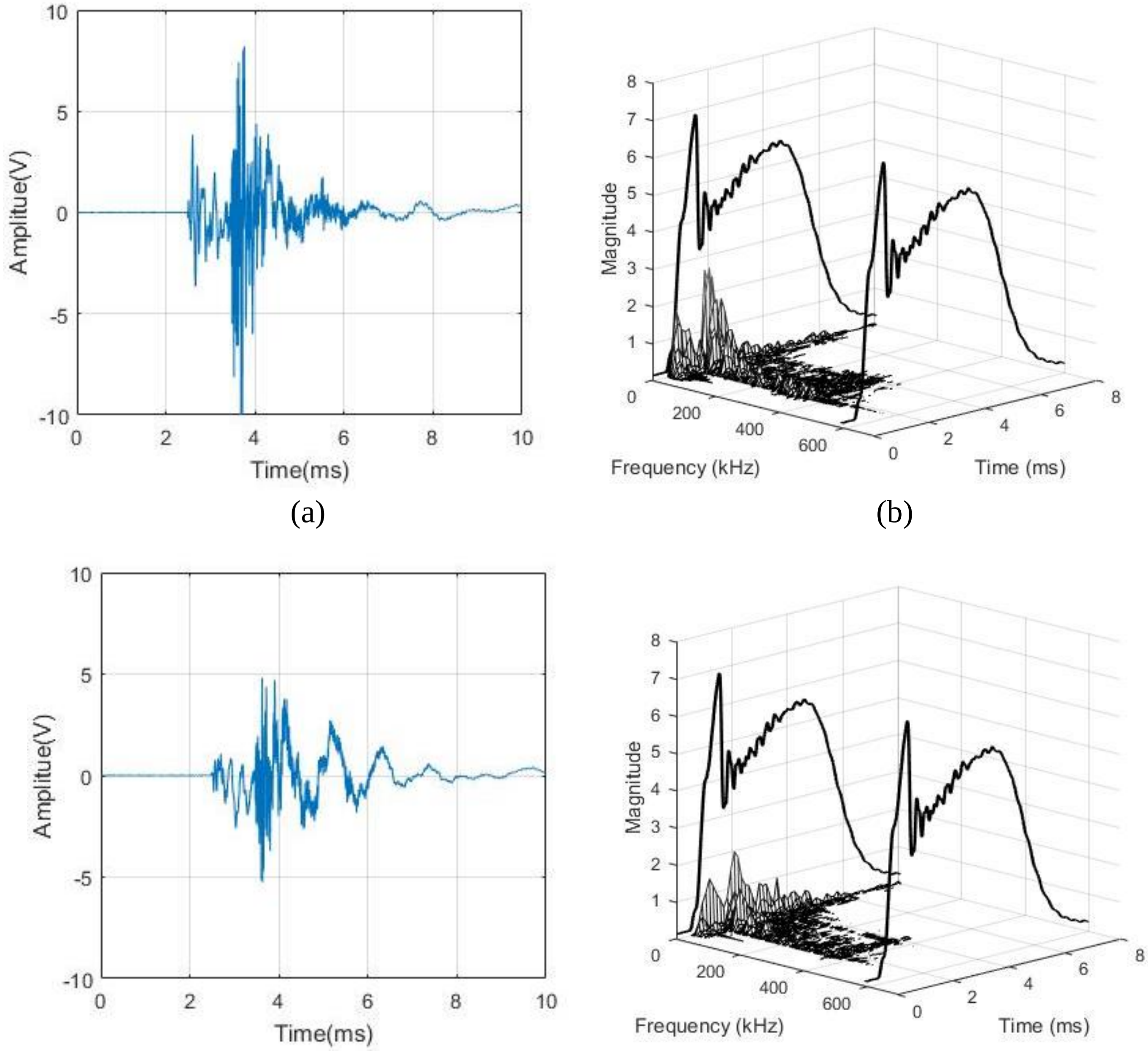

(a) (b)

(c) (d)

Figure 7-14. Raw AE signal and waterfall FFT plots due to impact of a plate with the addition of a stiffener. (a) Without stiffener, raw signal. (a) Without stiffener, waterfall FFT. (c) With stiffener, raw signal. (d) Without stiffener, waterfall FFT.

Figure 7-15 shows the measured AE signals and waterfall FFTs resulting from instrumented drop-weight impact testing on a composite plate with and without a through hole. The AE signals show some different trends in comparison to those produced by the bonded stiffener. The maximum amplitude of AE signals measured after passing the hole is larger than the AE signals measured before passing the hole. This finding is in agreement with the signal magnitude trends observed from the steel ball drop tests shown previously in Figure 604 and Figure 606. Another interesting observation may be made by comparing the two reference AE signals shown in Figure 7-14 (c) and 7-15 (c), While the reference signal for the plate with the through-hole in Figure 7-15 (c) shows noticeable low frequency components in the 4 -7 ms time range, the reference signal for the plate with stiffener condition in Figure 7-15 (c) shows reduced amplitude AE signals within the same time range. Considering the position in the time domain as well as the wave speed and wavelength of the low frequency wave, the higher amplitude AE signal wave could be a reflection from the hole. Alternatively, the difference shown in Figure 7-14 (c) and Figure 7-15 (c) in the 4-7 ms time range could be explained by the stiffener bonded to the plate producing a de-amplification of the low frequency component. It is noted that a similar amplitude reduction was observed in low frequency composites and attributed to the stiffener for the steel ball drop experiments as shown in Figure 7-11. For the case of the through hole, the waterfall FFT plots in Figure 7-15 (b) and (d) show that the magnitudes of the low frequency component were increased after passing through a hole. While analysis using the raw signals and waterfall FFT plots are useful for investigate wave behavior, however, these plots do not provide quantitative comparisons for use in composite damage classification analysis.

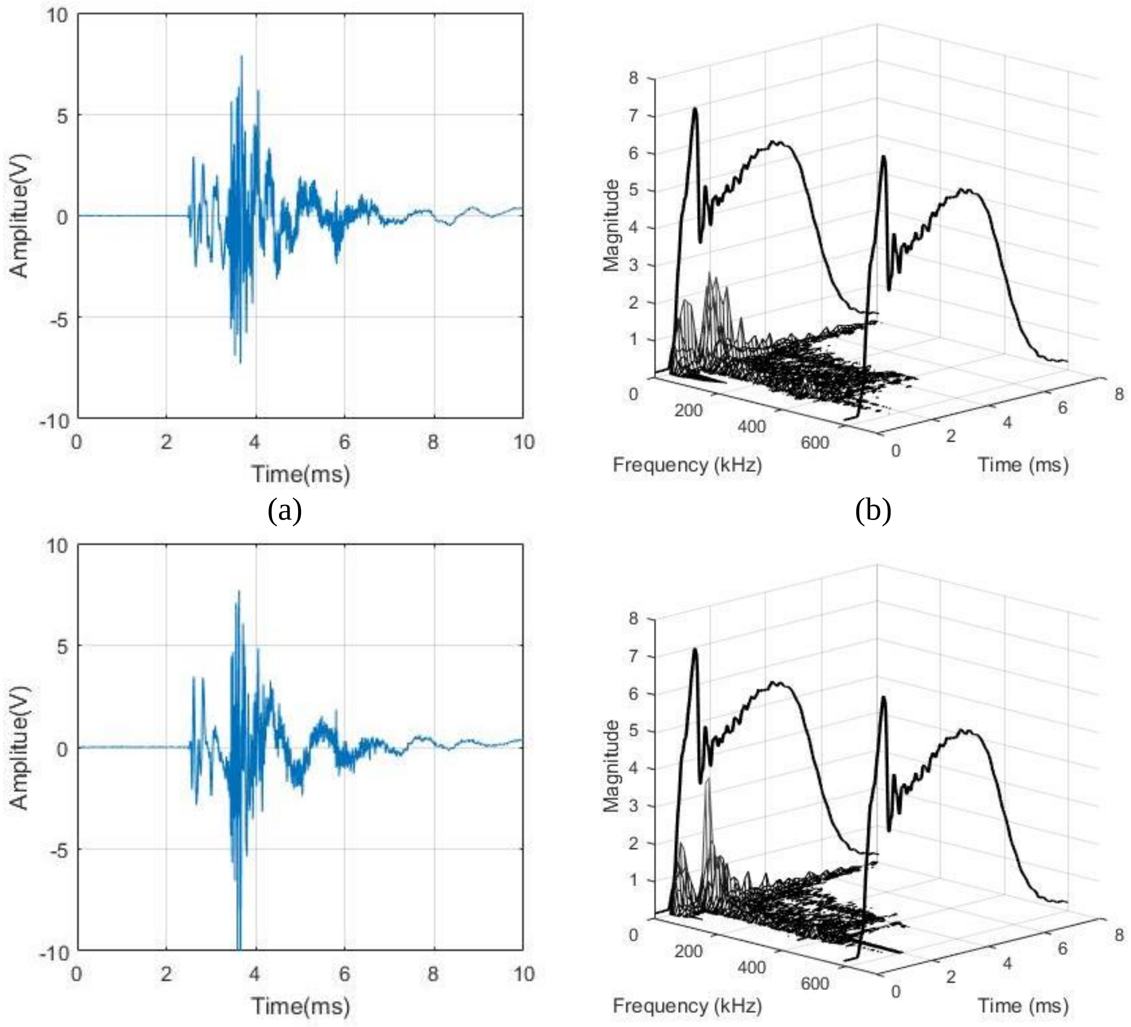

(a) (b)

(c) (d)

Figure 7-15. Raw signals and waterfall FFT plots due to impact of a plate with the additional of a through hole. (a) Without hole, raw signal. (a) Without hole, waterfall FFT. (c) With hole, raw signal. (d) Without hole, waterfall FFT.

In this context, the enveloped area of filtered signals was used as an AE-index in the frequency domain for damage classification analyses. Four frequency ranges were selected for filtering. The frequency range from 1-50 kHz represents low-frequency ranges, which are usually used for impact location estimation. The frequency range from 50-200 kHz represents AE signals produced by matrix cracks or delamination. The frequency ranges from 200-600 kHz, which usually represents AE signals related fiber breakage, was divided into two sub-ranges, from 200-400 kHz and from 400-600 khz, in order to maintain a similar interval.

In order to estimate the effects of facesheet configuration changes, the area under envelope values of reference signals were divided by division of over ones of signals after a hole or stiffener. Figures 7-16 and 7-17 represent the area under envelope index comparisons for impacted composite panels with differences in composite material types, ply layups, and thickness with a bonded stiffener and through hole, respectively.

From these figures, a difference is made apparent between the impacted panels with a bonded stiffener and those with a through hole. The presence of the through hole produces higher area under envelope ratios in all four frequency range than the bonded stiffener. As in the case of the steel ball drop tests, the existence of wave propagation paths on either side of the hole as well as the complexity of wave superposition behavior are possible explanations for increased the area under envelope ratio values.

A prominent trend shown in Figure 7-17 is the rapid value drop of the area under envelope ratio over all frequency ranges. This trend is believed to result from a combination of two different factors. First, there is a noticeable increase of ratio values in the 50-200 kHz range. Second, significant ratio value decrease is observed in the remaining three frequency ranges. For the larger ratio value drop, the higher frequency ranges are observed. Because changes in the ply layup produce differences in material stiffness, these stiffness changes may play a role in the observed trend. Comparing the quasi-static lay-ups (used as the reference condition) and the cross-ply lay-ups, the stiffness in the 0° and 90° directions of the cross-ply lay-up are higher than those using quasi-isotropic lay-up. However, the stiffness of the other angles such as 45° for the cross-ply layup is lower than for the quasi-isotropic layups. Differences in wave velocities are known to result from material stiffness differences, and thus the directional dependence in stiffness in the cross-ply laminate may affect wave propagation around the perimeter of the hole as well as reflections from walls. In general, these observations suggest that changes in received AE signals are dependent on the frequency range as well as the directional dependence of material stiffness. Because of the numerus factors that affect AE signal propagation, a more extensive experimental investigation is needed to provide additional insights.

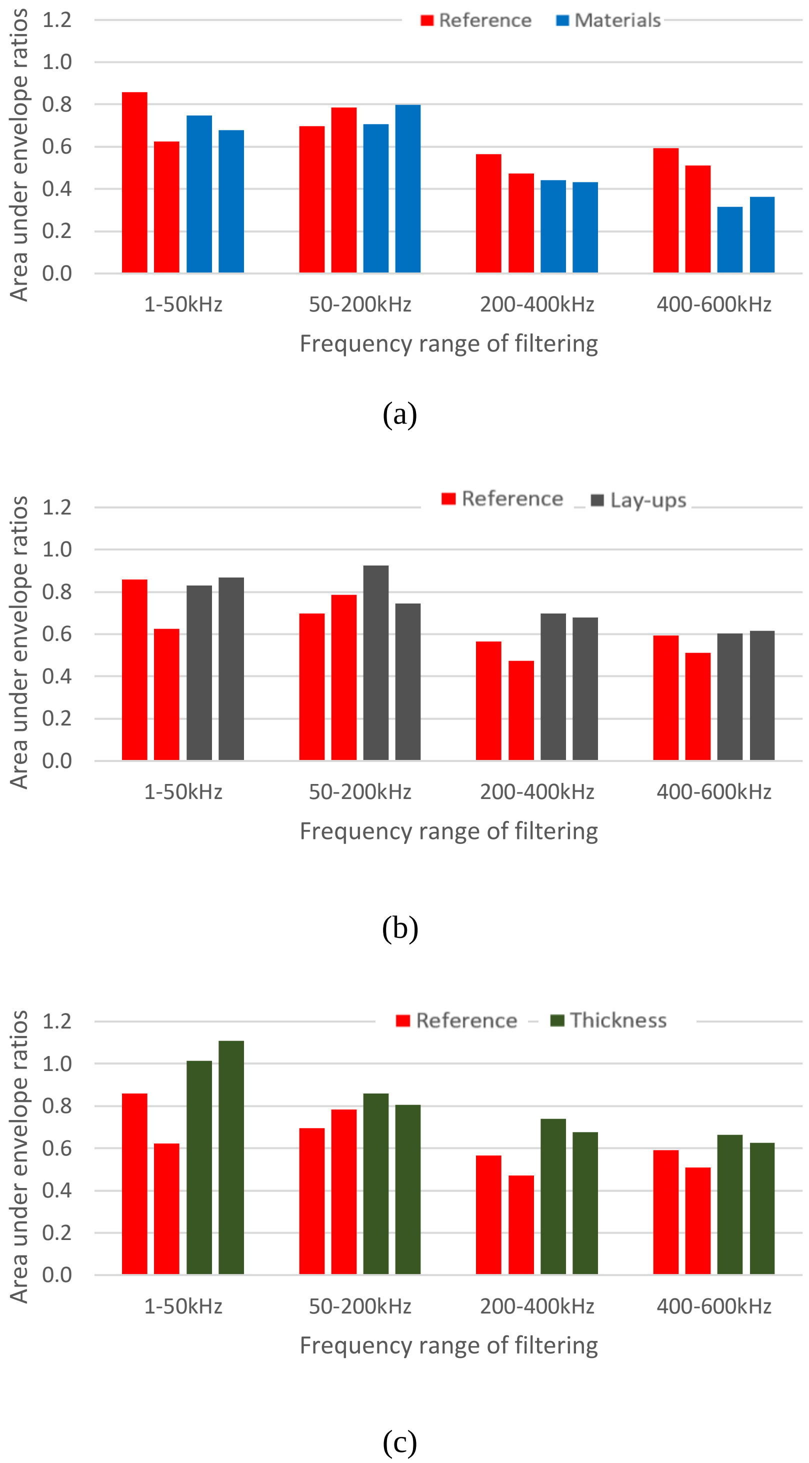

(a)

(b)

(c)

Figure 7-16. AE index comparisons for impacted panels with bonded stiffener. (a) Material differences. (b) Lay-up differences. (c) Thickness differences.

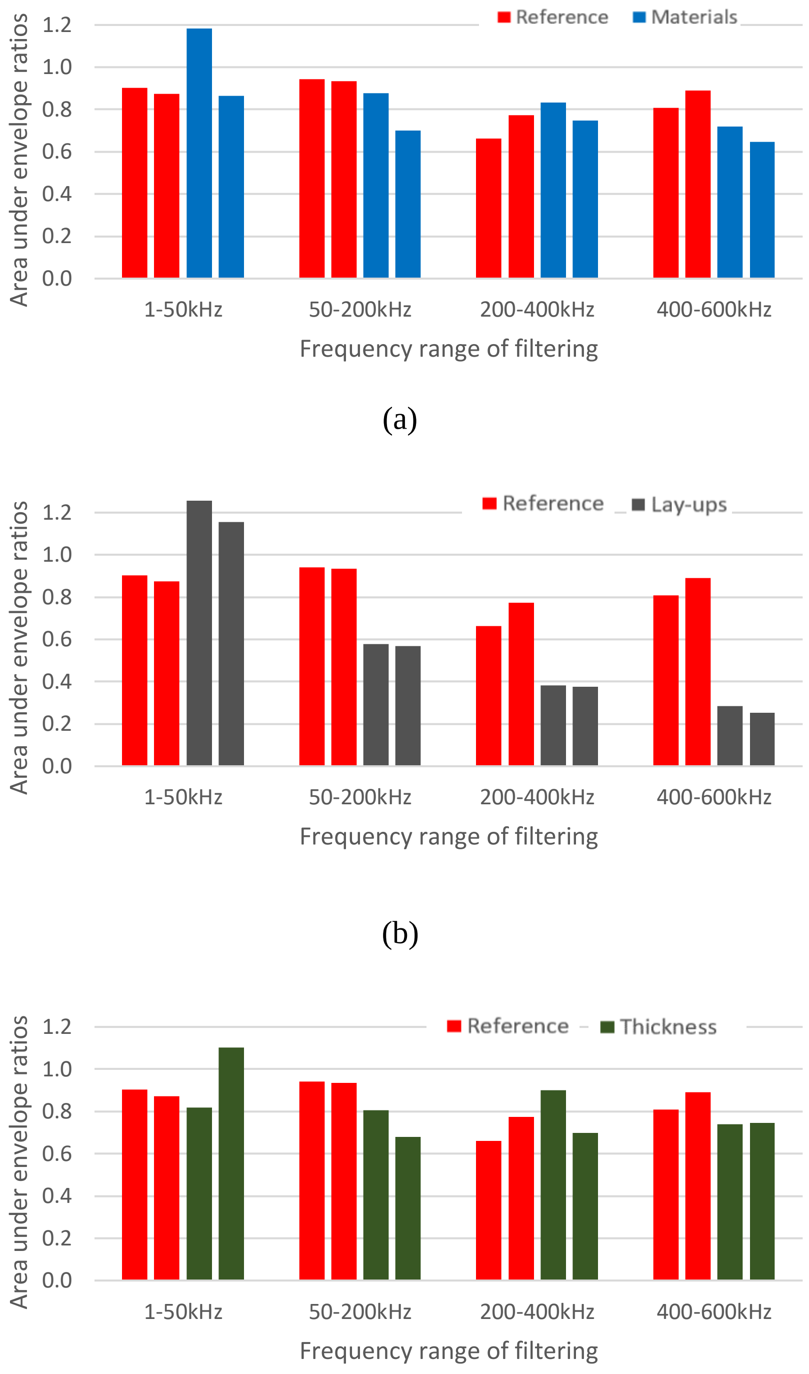

(c)

Figure 7-17. AE index comparisons for impacted panels with through hole. (a) Material differences (b) Lay-up differences. (c) Thickness differences.

7.5 Experimental Analysis of Sensor Distance Variation

A total of twenty impact tests were performed on a large composite cylinder at NASA Marshall Space Flight Center. The composite cylinder had a 1.2 m diameter, 1.8 m length, and a 20 mm wall thickness. A total of 21 AE sensors were installed on the cylinder: 15 Acellent Single Smart Layer piezoelectric sensors and 5 Digital Wave B1025 sensors. The Acellent sensors have a limited frequency range (1 - 50 kHz), which is insufficient for damage classification purposes. However, these sensors provide consistency in AE signal measurement due to their permanent attachments and suitable sensitivity for the impact conditions used.

Figure 7-18 (a) shows the positions of the installed AE sensors and the impact locations on the cylinder. Five Acellent sensor clusters, each composed of three Acellent sensors, were placed randomly on the cylinder, but outside of all impact locations. One Digital Wave sensor was attached in close proximity to each Acellent sensor cluster for comparison of received signals from the two types of sensors.

A total of 10 manually performed impact tests were conducted using a steel ball to produce AE signals causing only an elastic impact without the formation of any damage to the composite cylinder. Due to the curved surface and the thickness of the composite cylinder, a slingshot-type devise was used to provide greater impact energy and higher amplitude AE signals.

After conducting the steel-ball impact tests, ten drop-weight impact tests were performed using the drop-weight impactor shown in Figure 7-18 (b) at the positions of on the cylinder as the elastic impacts. Because only one large composite cylinder was available, all impact tests were performed using the same cylinder. However, due to the 300 mm minimum spacing of the damage-producing impacts, it is believed that the damage produced by previous impacts did not have a significant effect on AE signal propagation. To combine several impact locations, the intended impact energies, and impactor shapes, listed in Table 7-5, were selected to maximize the number of impact conditions while keeping the total number of impact tests to less than 10.

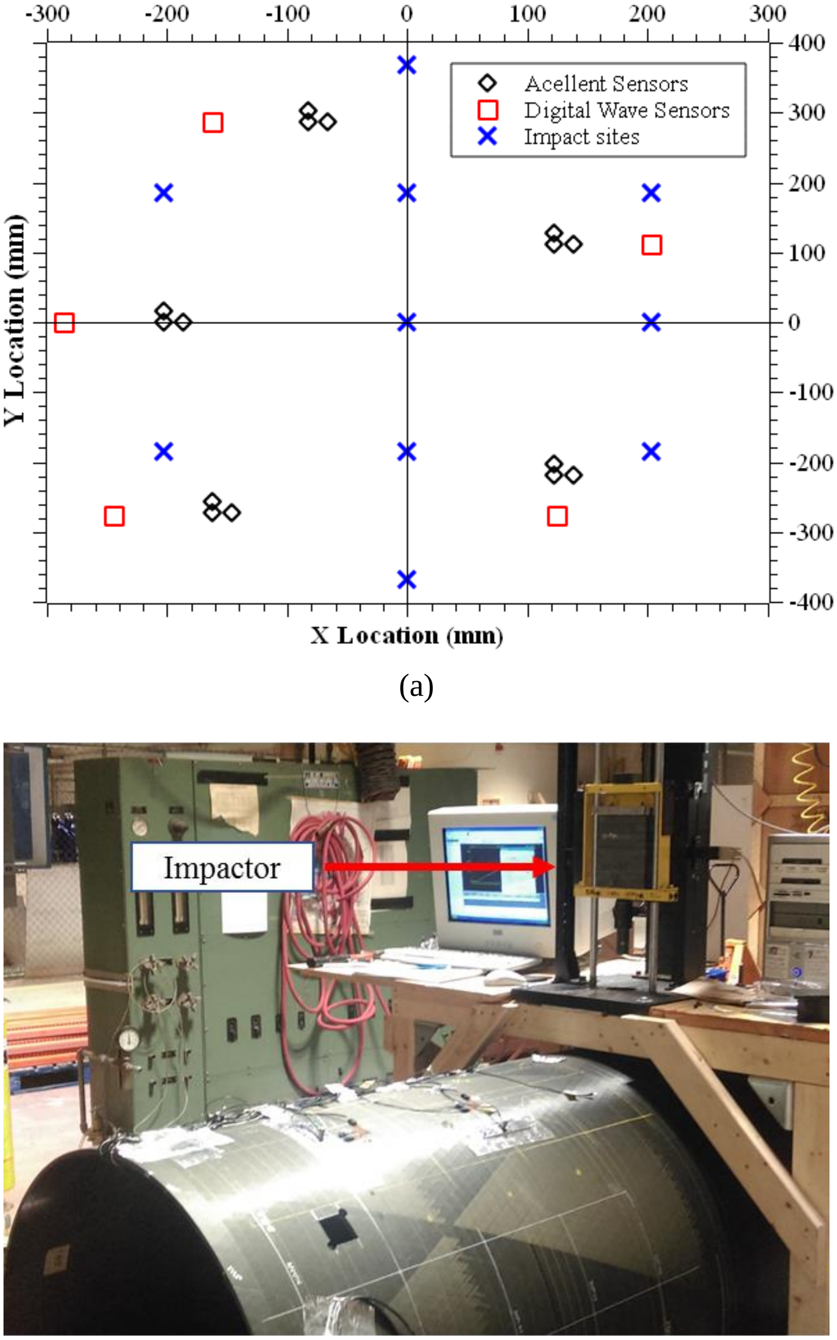

(a)

(b)

Figure 7-18. Impact test configuration for large composite cylinder. (a) AE sensor positions and impact locations (b) Instrumented drop-weight impact tester and the impacted composite cylinder.

Table 7-5. Impact Test Conditions Used For Large Composite Cylinder

Impact ID	impactor shape	Impact energy (N m)	X Location (mm)	Y Location (mm)
1	Round	34	0	-185
2	Round	68	0	0
3	Round	95	0	185
4	Round	136	203	-185
5	Round	136	203	185
6	Round	176	0	-369
7	Sharp	95	-203	-185
8	Sharp	136	-203	185
9	Sharp	199	203	0

A 32-channel Digital Wave FM1 data acquisition system was used for all AE-signal recording with 1 MHz sampling rate per channel. Before the analysis of the AE signals, a preliminary screening of valid AE signals was conducted in order to identify incorrectly collected signals. The screening was performed by raw time-domain signals. AE signals which had high noise-level signal strength, excessive signal saturation, and abnormal sensitivity (compared with other sensors in the same cluster) were removed from further analysis. Additionally, force information from the impactor was also collected when impacting was performed. Force versus time curves were collected from the instrumented drop-weight impact testing and used as an indicator of damage state instead of non-destructive inspections results, such as C-scan or thermal-deply, because no inspections were conducted on the impacted structure. Two assumptions were considered in order to estimate the damage state by means of the force versus time curves. First, a sudden and reasonably large force-drop in the force versus time curve indicates significant damage production. Second, high-impact energy produces more severe damage. Thus, there is potential that an impact with a significant force drop and high energy produces more AE signals from damage creation than an impact with lower energy. Because the mechanisms leading to the impact damage formations in composite materials are complex, the occurrence and size of delaminations or fiber breakage cannot be estimated merely through data provided by the force versus time information.

AE signals produced by ten elastic impact tests using a steel ball were used to estimate the amplitude reduction ratio of AE signals in the large composite cylinder. After an initial screening of AE signals, three Acellent sensors were eliminated from the data set because of abnormal sensitivity and the averaged peak-to-peak AE amplitude was calculated for each Acellent sensor cluster. Figure 7-19. (a) shows an example of a AE signal decay curve in which the coefficients of the fitted curve were calculated using five data points. A general form of the exponential function was used for curve fitting, given as

$$f(x) = Ae^{-Bx}. \tag{7-3}$$

Signal decay ratios of AE signals can be affected by a variety of factors, including geometry, material damping ratios, and attenuation. Considering the nonlinearity of these factors, exponential decay functions are appropriate for primary estimation of a signal-decay curve. For each of the ten elastic impact tests performed, a data set of location versus amplitude was generated and the results for the calculated coefficients A and B were averaged.

Figure 7-19. (b) shows the calculated coefficients A and B from each elastic impact test. Although an outlier is observed in the plot of coefficient A, the remaining calculated coefficients suggest that this estimation method used for characterizing the signal-decay rate is appropriate.

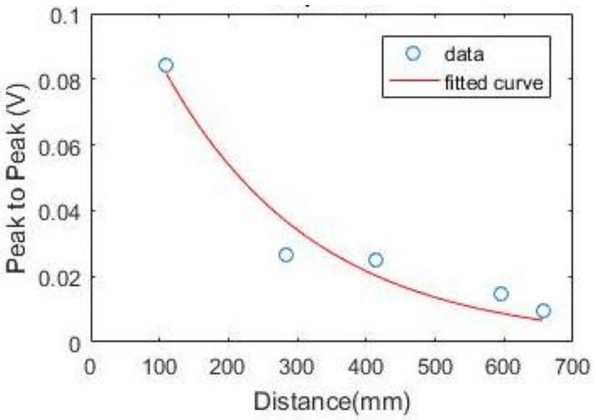

(a)

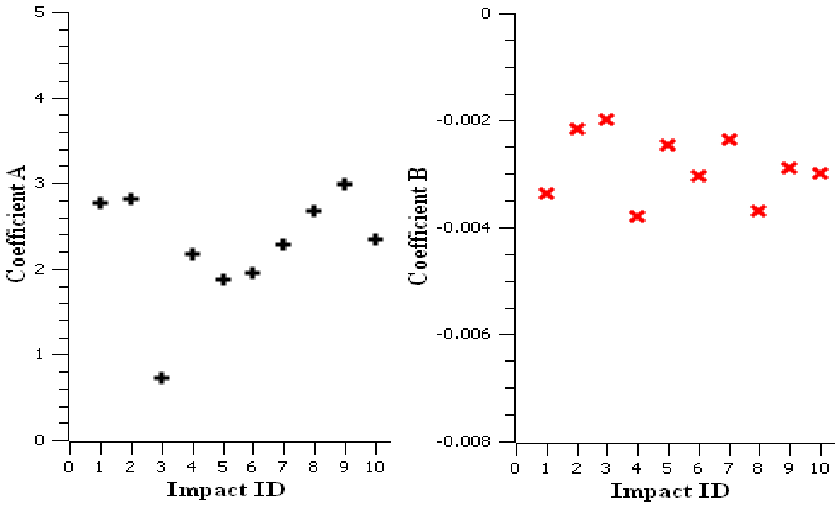

(b)

Figure 7-19. Calculation of signal decay coefficients. (a) Signal decay curves estimated from an impact (b) Calculated coefficients A and B from all impacts.

Figure 7-20 shows the estimated signal-decay curve obtained from the averaged coefficients in the exponential-decay formula. Based on the results obtained, the preferred range of sensor-to-impact distances to minimize compensation error appears to be in the range of 200 mm to 400 mm. Through a preliminary screening of the received AE signals and their related load curves from drop-weight impact testing, incorrectly recorded AE signals were eliminated from further analysis. As a result, a total of nine impact test results were analyzed using the data obtained from four Digital Wave sensors.

Figure 7-21 shows the AE signals plotted versus time for the four Digital Wave sensors for a representative drop-weight impact test. Because the distance from the impact location to each sensor was different, the recorded AE signals have differences in amplitude magnitudes as well as overall signal shape.

As a preliminary approach for the compensation of AE signal strength, a simple weighting factor was applied using the signal-decay rate function given in equation 7-3. The weighing factor used for signal compensation is defined as

$$g(x) = \frac{1}{Ae^{-Bx}} \cdot f(x)\,, \tag{7-4}$$

where $g(x)$ is the compensated signal and $f(x)$ is the original signal from equation 7-3.

Because the inverted signal decay rate in equation 7-4 produces low values for sensors near the impact location and high values for sensors at large distances, the differences in signal strength of the original AE signals can be compensated for.

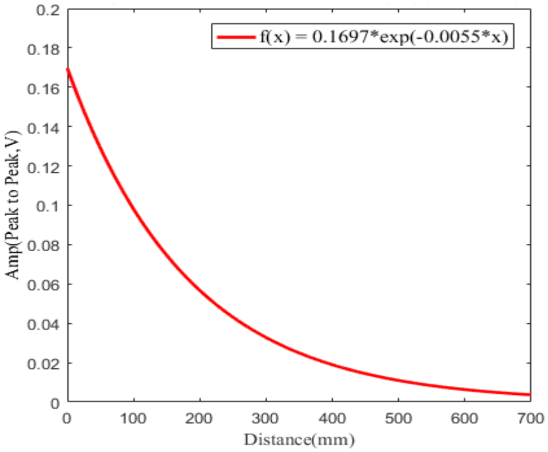

Figure 7-20. Estimated signal decay rate curve of the cylinder.

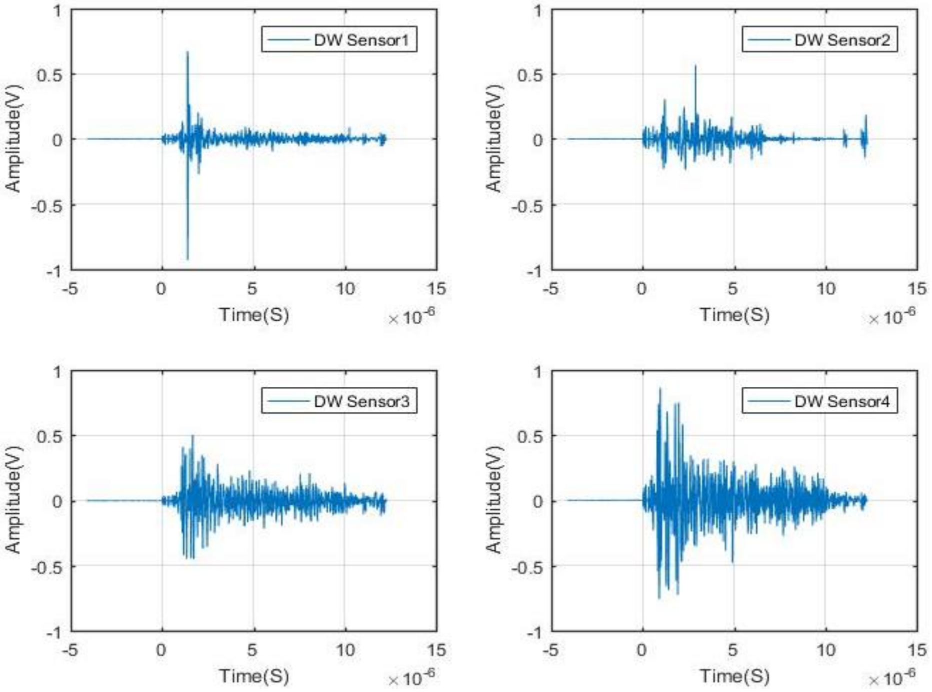

Figure 7-21. Raw AE signals of Digital Wave sensors from an impact.

Figure 7-22 shows the effects of applying the weighting factor to the damage index for impact experiments using a sharp and round impactor. The damage index, which uses the enveloped area of filtered signals method, was suggested previously in Chapter 4.3.3 as a means to convert AE signal magnitude to values. The index was calculated separately for each Digital Wave sensor and then compensated by the weighing factor. Since the determination of damage type was not a consideration for the current analysis, the frequency range for all damage types, between 100 kHz and 600 kHz, was used for filtering. For the sharp impactor, results in Figure 7022 (a) show that before using the compensation factor, an irregularly high damage index value was produced for the lower energy 70 J impact and a relatively low damage index value for the higher energy 147 J impact. Using the compensation factor, the damage index value for the three impact energies are consistent with the undamaged versus damaged conditions observed visually.

Similarly, for the round impactor, uncompensated damage index values shown in Figure 7-22 (b) do not display a direct correlation between the damage index and impact energy. When the compensation factor is applied, however the correlation is improved. The only impact test that did not result in a load drop during impacting, indicating no impact damage produced was the 25 J impact. Note that when using the compensated damage index values, this impact condition is significantly different than the others. Thus, the use of distance compensation for the damage index shows potential for use in the assessment of damage formation in composite structures. However, further improvements may be possible through the use of improved estimation methods for the signal decay curve and the weighing factor equation.

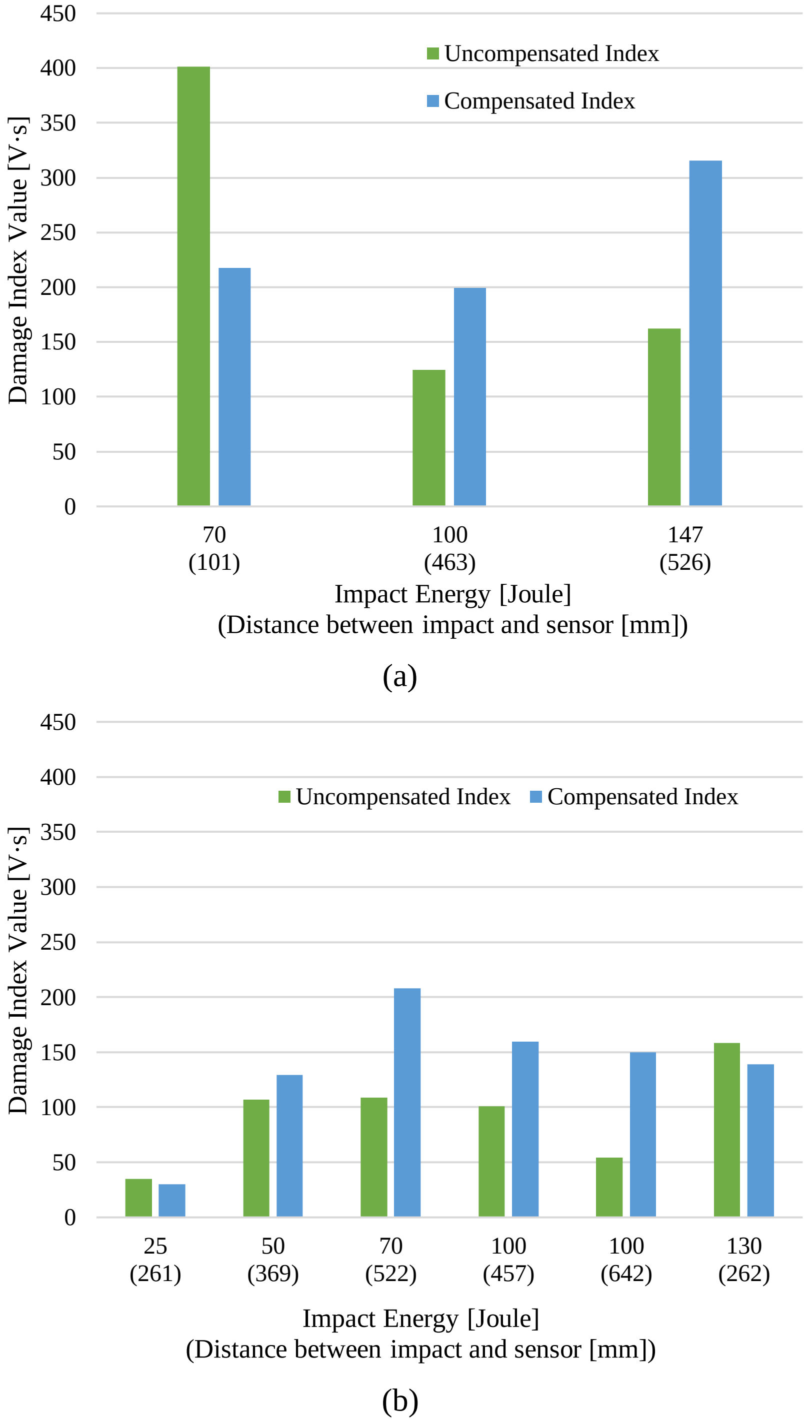

Figure 7-22. Comparison of damage index before and after compensation. (a) Sharp impactor. (b) Round impactor.

7.6 Summary and Conclusions

As the impact location-estimation algorithm developed in this project for SHM utilizes Lamb wave time-of-arrival information, the characteristics of such wave propagation in composite structures are of particular interest. Two particular Lamb wave propagation characteristics were investigated using numerical analysis. First, the directional dependence of Lamb wave velocity in composite laminates was investigated. Finite element analyses featuring layer-by-layer modeling and applied displacement signal inputs were used to explore directional dependence of wave propagation in a quasi-isotropic carbon/epoxy composite laminate. Additionally, experimental measurements were obtained using AE sensors for both the excitation source and the signal receiver. Results from both analysis and experiment suggest that directional dependence of Lamb wave propagation may occur in a quasi-isotropic composite laminate, even though the effective, homogenized elastic properties are the same in all in-plane directions.

Additionally, finite element analyses were performed to investigate the characteristics of Lamb wave propagation in composite panels with simple geometric discontinuities. Of particular interest were changes in time-of-arrival of Lamb waves due to circular cutouts in the path of Lamb wave propagation. Candidate modeling methodologies were explored for these analyses, and a homogenized material model was found to be suitable for investigating time-of-arrival effects. Results suggest that the relationship between hole diameter and time delay as well as amplitudes does not appear to be a simple linear relationship. Results from finite element analysis with an added stiffener showed complex wave behavior, suggesting that changes to the cross-sectional geometry of the stiffener produce significant changes in wave amplitudes and arrival times.

AE propagation was investigated experimentally in composite structures with geometrical complexities as well as with relatively large distances between impact location and sensor positions. Experimental approaches and signal analysis methods were developed to evaluate changes in AE signals caused by these structural variations. To investigate AE signal changes due to geometrical complexity, bonded stiffeners or through holes were added to composite plates. AE signals resulting from both elastic steel ball drop impacts and damage-producing drop-weight impacts were recorded. Through analyses in both the time and frequency domains, the amplitude of AE signals was found to be affected by each type of geometrical complexity. Through the use of a calculated damage index, different frequency ranges were found to have different signal reduction ratios. In general, higher frequency ranges experienced greater signal loss due to the geometrical complexities investigated.

To investigate AE signal changes due to distance variations from the impact, a series of elastic steel ball drop impacts and damage-producing drop-weight impacts were performed using a large composite cylinder. Based on AE signals produced from the steel ball drop impacts, signal-decay curves were developed. A distance-compensation method for the damage index was developed using a weighing factor based on the signal-decay ratio. Results obtained suggest that the use of the proposed distance compensation method for the damage index may be useful for assessing damage formation in composite structures.

REFERENCES

1. Wang, H. and Chu, P. "Voice source localization for automatic camera pointing system in videoconferencing," *IEEE International Conference on Acoustics, Speech, and Signal Processing (ICASSP)*, pp. 187–190, Munich, Bavaria, Germany, April 1997.

2. Schau, H.C. and Robinson, A.Z., "Passive source localization employing intersecting spherical surfaces from time-of- arrival differences," *IEEE Transactions on Acoustics, Speech, and Signal Processing*, vol. 35, no. 8, pp. 1223–1225, 1987.

3. Huang, Y., Benesty, J., Elko, G.W., and Mersereau, R.M., "Real-time passive source localization: A practical linear-correction least-squares approach," *IEEE Transactions on Speech and Audio Processing*, vol. 9, no. 8, pp. 943–956, 2001.

4. Coverley,, P.T., and Staszewski, W.J., "Impact damage location in composite structures using optimized sensor triangulation procedure," *Smart Materials and Structures*, vol. 12, no. 5, pp. 795–803, 2003.

5. Salehian, A., "Identifying the location of a sudden damage in composite laminates using wavelet approach," *MS Thesis*, Worcester Polytechnic Institute, 2003.

6. Meo, M., Zumpano, G., Piggott, M., and Marengo, G., "Impact identification on a sandwich plate from wave propagation responses," *Composite Structures*, vol. 71, no. 3, pp. 302–306, 2005.

7. Kundu, T., Das, S., and Jata, K.V. "Detection of the point of impact on a stiffened plate by the acoustic emission technique," *Smart Materials and Structures*, vol. 18, no. 3, pp. 1–9, 2009.

8. Hajzargerbashi, T., Kundu, T., and Bland, S., "An improved algorithm for detecting point of impact in anisotropic inhomogeneous plates," *Ultrasonics*, vol. 51, no. 3, pp. 317–324, 2011.

9. Papulak, T.S., "An inverse acoustical phased array technique for impact detection and location," *MS Thesis*, University of Utah, 2012.

10. Putkis, O., Dalton, R.P., and Croxford, A.J., "The influence of temperature variations on ultrasonic guided waves in anisotropic CFRP plates," *Ultrasonics*, vol. 60, pp. 109–116, 2015.

11. Lu, Y.H., and Michaels, J.E., "A methodology for structural health monitoring with diffuse ultrasonic waves in the presence of temperature variations," *Ultrasonics*, vol. 43, no. 9, pp. 717–731, 2005.

12. Hiche, C., Coelho, C.K., and Chattopadhyay, A., “A strain amplitude-based algorithm for impact localization on composite laminates,” *Journal of Intelligent Material Systems and Structures*, vol. 22, no. 17, pp. 2061–2067, 2011.

13. Ciampa, F. and Meo, M., “A new algorithm for acoustic emission localization and flexural group velocity determination in anisotropic structures,” *Composites Part A: Applied Science and Manufacturing*, vol. 41, no. 12, pp. 1777–1786, 2010.

14. Zhou, J., Mathews, V.J., and Adams, D.O., “Impact location estimation in anisotropic structures,” *41st Annual Review of Progress in Quantitative Nondestructive Evaluation*, pp. 1081–1090, Boise, Idaho, USA, July 2014.

15. Zhou, J., Mathews, V. J., and Adams, D.O., “Impact location estimation in anisotropic media,” *IEEE International Conference on Acoustics, Speech and Signal Processing (ICASSP)*, pp. 2614–2618, Brisbane, Australia, April 2015.

16. Zhou, J., Mathews, V.J., and Adams, D.O., “Acoustic emission-based impact location estimation for composite structures,” *The 10th International Workshop on Structural Health Monitoring*, pp. 1510–1518, Stanford University, USA, September 2015.

17. Kundu, T., Nakatani, H., and Takeda, N., “Acoustic source localization in anisotropic plates,” *Ultrasonics*, vol. 52, no. 6, pp. 740–746, 2012.

18. Rima, R.A. , and Banerjee, S., “Novel approach for acoustic source localization using spiral sensing,” *The 9th International Workshop on Structural Health Monitoring*, pp. 2643–2650, Stanford University, USA, September 2013.

19. Ciampa, F. and Meo, M., “Impact detection in anisotropic materials using a time reversal approach,” *Structural Health Monitoring*, vol. 11, no. 1, pp. 43–49, 2012.

20. Ing, R.K., Quieffin, N., Catheline, S., and Fink, M., “In solid localization of finger impacts using acoustic time-reversal process,” *Applied Physics Letters*, vol. 87, no. 20, pp. 1–3, 2005.

21. Manikas, A., Kamil, Y.I., and Karaminas, P., “Positioning in wireless sensor networks using array processing,” *IEEE Global Telecommunications Conference (GLOBECOM)*, pp. 1–5, New Orleans, LA, USA, November 2008.

22. Manikas, A., Kamil, Y.I., and Willerton, M., “Source localization using sparse large aperture arrays,” *IEEE Transactions on Signal Processing*, vol. 60, no. 12, pp. 6617–6629, 2012.

23. Zhong, Y., Yuan, S. and Qiu, L., “Near-field 2D-MUSIC algorithm based impact localization using linear array,” *The 9th International Workshop on Structural Health Monitoring*, pp. 2659–2666, Stanford University, USA, September 2013.

24. Griva, I., Nash, S.G., and Sofer, A., *Linear and nonlinear optimization*, SIAM, Philadelphia, PA, USA, 2009.

25. Gutkin, R., Green, C.J., Vangrattanachai, S., Pinho, S.T., Robinson, P. and Curtis, P.T., "On acoustic emission for failure investigation in CFRP: Pattern recognition and peak frequency analyses," *Mechanical Systems and Signal Processing*, vol. 25, no. 4, pp. 1393–1407, 2011.

26. Shahidan, S., Pulin, R., Bunnori, N.M., and Holford, K.M., "Damage classification in reinforced concrete beam by acoustic emission signal analysis," *Construction and Building Materials*, vol. 45, pp. 78–86, 2013.

27. Kim, S., Uprety, B. Adams, D.O., Mathews, V.J., and Harley, J.B., "Acoustic emission based damage characterization in composite plates using low-velocity impact testing," in *10th Int. Workshop Structural Health Monitoring*, Stanford University, CA, USA, 2015, pp. 1477–1484.

28. Ramirez-Jimenez, C.R., Papadakis, N., Reynolds, N., Gan, T.H., Purnell, P., and Pharaoh, M., "Identification of failure modes in glass/polypropylene composites by means of the primary frequency content of the acoustic emission event", *Compos. Sci. Technol.*, vol. 64 no. 12, pp. 1819–1827, 2004.

29. de Groot, P.J., Wijnen, P.M., and Janssen, R.B.F., "Real-time frequency determination of acoustic emission for different fracture mechanisms in carbon/epoxy composites", *Compos. Sci. Technol.*, vol. 55, no. 4, pp. 405–412, 1995.

30. Yan, Y.J., Hao, N.H., and Yam, L.H., "Vibration-based construction and extraction of structural damage feature index," *International Journal of Solids and Structures*, vol. 41, no. 24, pp. 6661–6676, 2004.

31. Ying, Y.J., Garrett, J.H. Jr., Harley, J.B., Oppenheim, I.J., Shi, J., and Soibelman, L., "Damage detection in pipes under changing environmental conditions using embedded piezoelectric transducers and pattern recognition techniques," *Pipeline Syst. Eng. Practice*, vol. 4, no. 1, pp. 17–23, 2013.

32. Ying, Y.J., Garrett, J.H. Jr., Oppenheim, I.J., Soibelman, L., Harley, J.B., Shi, J., and Jin, Y.W., "Toward data-driven structural health monitoring: application of machine learning and signal processing to damage detection," *J. Comput. Civil Eng.*, vol. 27, no. 6, pp. 667–680, 2013.

33. Dua, R., Watkins, S.E., Wunsch, D.C., Chandrashekhara, K., and Akhavan, F., "Detection and classification of impact-induced damage in composite plates using neural networks," *International Joint Conference on Neural Networks*, pp. 681–686, Washington, D.C., USA, July 2001.

34. De Lautour, O. R. and Omenzetter, P., “Damage classification and estimation in experimental structures using time series analysis and pattern recognition,” *Mechanical Systems and Signal Processing*, vol. 24, no. 5, pp. 1556–1569, 2010.

35. Johnson, M., “Waveform based clustering and classification of AE transients in composite laminates using principal component analysis,” *NDT & E International,* vol. 35, no. 6, pp. 367–376, 2002.

36. Zhou, W., Chakraborty, D., Kovvali, N., Papandreou-Suppappola, A., Cochran, D, and Chattopadhyay, A., “Damage classification for structural health monitoring using time-frequency feature extraction and continuous hidden Markov models,” *The 41st Asilomar Conference on Signals, Systems and Computers,* pp. 848–852, Pacific Grove, CA, USA, November 2007.

37. Chakraborty, D., Kovvali, N., Wei, J., Papandreou-Suppappola, A., Cochran, D., and Chattopadhyay, A., “Damage classification structural health monitoring in bolted structures using time-frequency techniques,” *Journal of Intelligent Material Systems and Structures*, vol. 20, pp. 1289–1305, 2009.

38. Abdel-Latif, A.M., “An overview of the applications of NDI/NDT in engineering design for structural integrity and damage tolerance in aircraft structures,” in *Damage and Fracture Mechanics*, pp. 93–100. 2009.

39. Dobson, A.J. and Barnett, A., *An Introduction to Generalized Linear Models,* CRC Press, Boca Raton, FL, USA, 2008.

40. Friedman, J., Hastie, T., and Tibshirani, R., *The Elements of Statistical Learning*, Springer Series in Statistics, New York, NY, USA, 2001.

41. Lin, J., Weng, R.C., and Keerthi, S.S., “Trust region newton method for logistic regression,” *J. Mach. Learn. Res*., vol. 9, pp. 627–650, 2008.

42. Balanda, K.P. and MacGillivray, H.L., “Kurtosis: a critical review,” *Am. Stat.*, vol. 42, no. 2, pp. 111–119, 1988.

43. Stoica, P. and Moses, R.L., *Introduction to Spectral Analysis*, Prentice Hall, Upper Saddle River, NJ, USA, 1997.

44. Tibshirani, R., “Regression shrinkage and selection via the lasso,” *J. R. Stat. Soc. Series B Methodol*., vol. 58, no. 1, pp. 267–288, 1996.

45. Friedman, J., Hastie, T., and Tibshirani, R. “Regularization paths for generalized linear models via coordinate descent,” *J. Stat. Softw*., vol. 33, no. 1, pp. 1–22, 2010.

46. Kohavi, R. and Provost, F., “Glossary of terms,” *Machine Learning*, vol. 30, no. 2, pp. 271–274, 1998.

47. Fawcett, T., “Roc graphs: Notes and practical considerations for researchers,” *Machine Learning*, vol. 31, no. 1, pp. 1–38, 2004.

48. Acellent Technologies, Inc.. *Standard Smart Layer*, retrieved from http://www.acellent.com/blog1/products/sensors/standard-smart-layer/ .

49. Vallen Systeme. *Acoustic Emissions Sensors Specification*, retrieved from http://www.vallen.de/sites/default/files/sov1212_0.pdf , 2009.

50. Digital Wave, *B1025T- Broadband Acoustic Emission Sensor*, retrieved from http://digitalwavecorp.com/MAE-051414-%20B1025T%20Sensor.pdf .

51. Steiner and Martins, Inc., *Piezoelectric Ceramic Plate Transducer 240 KHz - STEMINC.*, retrieved from http://www.steminc.com/PZT/en/piezo-ceraminc-plate-7x8x02mm-wire-lead-240-khz .

52. KRN Services, *SteveCo KRNBB-PC Point Contact Sensor*, retrieved from http://www.krnservices.com/documents/krnbb-pc_specs.pdf .

53. Lowe, M., Disperse Software, Imperial College London , 2013.

54. ANSYS Inc., *ANSYS Help Manual Version 15.0*, 2013.

55. Grosse, C.U., and Ohtsu, M., Introduction, in *Acoustic emission testing: Basics for research, applications in civil engineering,* pp. 3-6, Berlin: Springer, 2008.

56. Prosser, W.H., “The propagation characteristics of the plate modes of acoustic emission waves in thin aluminum plates and thin graphite/epoxy composite plates and tubes”, *Doctoral dissertation*, John Hopkins University, 1991.

57. Ponnala, L. “Analysis of genetic translation using signal processing”, p. 13, *Doctoral dissertation*, North Carolina State University, 2007.

58. Proakis, J.G., & Manolakis, D.G., “Frequency domain analysis of LTI system”, *Digital Signal Processing,* pp. 312-314, NJ: Pearson Prentice Hall, 2007.

59. Harley, J.B., & Moura, J.M., “Sparse recovery of the multimodal and dispersive characteristics of Lamb waves”, *Journal of the Acoustical Society of America, 133*(5), pp. 2732–2745, 2013.

60. Oskouei, A.R. and Ahmadi, M., "Acoustic emission characteristics of Mode I delamination in glass/polyester composites", *J. Compos. Mater*., vol. 44, no. 7, pp. 793–807, 2010

61. Bohse, J., "Acoustic emission characteristics of micro-failure processes in polymer blends and composites", *Compos. Sci. Technol.*, vol. 60, pp. 1213–1226, 2000.

62. Giordanoa, M., Condeilib, L, and Nicolaisb, L, “Acoustic emission wave propagation in a viscoelastic plate,” *Compos. Sci. Technol.*, vol. 59, no. 11, pp. 1735–1743, 1999.

63. Komai, K., and Minoshima, T “Investigations of the fracture mechanism of carbon/epoxy composites by AE signal analyses,” *JSME Int.Journal. Ser. 1: Solid Mech., Strength Mater.*, vol. 34, no. 3, pp. 381–388, 1991.

64. Suzuki, M., Kida, S., Shimbo, M. and Miyano, Y., “Effects of fiber content on fracture mechanisms of short fiber reinforced PET composites.” Proc. *8th Int. Conference on Composite Materials*, Vol. 3., 1991.

65. Suzuki, M., Nakanishi, H., Iwamoto, M., and Jinen, E., “Application of static fracture mechanisms to fatigue fracture behavior of class A-SMC composite,” in Proc. *4th Japan-US Conference on Composite Materials*, pp. 297–306, 1988.

66. Russell, S. S., and Henneke, E. G., “Signature analysis of acoustic emission from graphite/epoxy composites,” Interim report, *NASA Grant NSG 1238*, vol. Report No., no. VPI-E-77-22, 1977.

67. Bagheri, A., Li, K., and Rizzo, P., “Reference-free damage detection by means of wavelet transform and empirical mode decomposition applied to Lamb waves,” *J. Intell. Mater. Syst. Struct.*, vol. 24, no. 2, pp. 194–208, 2012.

68. Gibson, R.F., Principles of Composite Material Mechanics, Third Edition. CRC Press, 2011.

69. Sause, M.G.R., “Investigation of pencil-lead breaks as acoustic emission sources,” *J. Acoust. Emiss.*, vol. 29, pp. 184–196, 2011.

REPORT DOCUMENTATION PAGE

Form Approved
OMB No. 0704-0188

1. REPORT DATE *(DD-MM-YYYY)*
01–09–2019

2. REPORT TYPE
Contractor Report

3. DATES COVERED *(From - To)*

4. TITLE AND SUBTITLE
Acoustic Emission-Based Health Monitoring
of Space Launch System Structures

5a. CONTRACT NUMBER
NNM13AA12G

5b. GRANT NUMBER

5c. PROGRAM ELEMENT NUMBER

6. AUTHOR(S)
D.O. Adams*, J. Zhou*, S. Kim*, and B. Uprety*
V.J. Mathews**

5d. PROJECT NUMBER

5e. TASK NUMBER

5f. WORK UNIT NUMBER

7. PERFORMING ORGANIZATION NAME(S) AND ADDRESS(ES)
George C. Marshall Space Flight Center
Huntsville, AL 35812

8. PERFORMING ORGANIZATION REPORT NUMBER
M–1489

9. SPONSORING/MONITORING AGENCY NAME(S) AND ADDRESS(ES)
National Aeronautics and Space Administration
Washington, DC 20546–0001

10. SPONSORING/MONITOR'S ACRONYM(S)

11. SPONSORING/MONITORING REPORT NUMBER
NASA/CR—2019–220138

12. DISTRIBUTION/AVAILABILITY STATEMENT
Unclassified-Unlimited
Subject Category
Availability: NASA STI Information Desk (757–864–9658)

13. SUPPLEMENTARY NOTES
*University of Utah, Salt Lake City, Utah
**Oregon State University, Corvallis, Oregon

14. ABSTRACT

This investigation focused on the development of a structural health monitoring system for space launch system vehicles based on acoustic emission (AE) signals. The AE-based impact location estimation method developed does not require knowledge of the location and direction-dependent velocities of wave propagation in the structure. To investigate impact damage classification based on received AE signals, an efficient machine learning approach, based on logistic regression, was developed. Quasi-static and impact testing was performed to characterize damage produced using received AE signals. Results suggest that impact damage classification is possible in composite structures through the analysis of AE signal features.

15. SUBJECT TERMS
Structural health monitoring; Composite structures; Acoustic emission; Impact location estimation; Impact damage classification; Space launch systems.

16. SECURITY CLASSIFICATION OF:			17. LIMITATION OF ABSTRACT	18. NUMBER OF PAGES
a. REPORT	b. ABSTRACT	c. THIS PAGE		
U	U	U	UU	150

19a. NAME OF RESPONSIBLE PERSON
STI Help Desk at email: help@sti.nasa.gov

19b. TELEPHONE NUMBER ***(Include area code)***
STI Help Desk at: 757–864–9658

Standard Form 298 (Rev. 8-98)
Prescribed by ANSI Std. Z39-18

National Aeronautics and
Space Administration
IS02
George C. Marshall Space Flight Center
Huntsville, Alabama 35812